Title

A STUDY OF THE REACTION n+ d->(p) p n+ n- n| AT INCIDENT PION MOMENTA BETWEEN 1.1 AND 2.4 BeV/c.

Author

Danburg, Jerome Samuel.

Publication Date

1969-07-01

UCRL-19275
c.2

DISCLAIMER

A STUDY OF THE REACTION $\pi^+ d \rightarrow (p) p \pi^+ \pi^- \pi^0$ AT INCIDENT PION MOMENTA BETWEEN 1.1 AND 2.4 BeV/c

Jerome Samuel Danburg
(Ph.D. Thesis)

July 1969

AEC Contract No. W-7405-eng-48

Dedicated to the memory of my father,

August Danburg

A STUDY OF THE REACTION $\pi^+ d \rightarrow (p)\, p\, \pi^+ \pi^- \pi^o$

AT INCIDENT PION MOMENTA BETWEEN 1.1 AND 2.4 BEV/C

Contents

A STUDY OF THE REACTION π^+ d ---> (p) p π^+ π^- π^o AT INCIDENT PION MOMENTA BETWEEN 1.1 AND 2.4 BEV/C

JEROME SAMUEL DANBURG

Lawrence Radiation Laboratory

University of California

Berkeley, California

ABSTRACT

The reaction π^+ d ---> (p) p π^+ π^- π^o has been studied in a 264 000-picture bubble chamber experiment with pion beam momentum between 1.1 and 2.4 BeV/c.

The most significant features of the final state are production of η and ω mesons in the reactions

$$\pi^+ n \longrightarrow \eta p,$$

$$\pi^+ n \longrightarrow \omega p.$$

The η production characteristics are well described by a Reggeized A_2-exchange model using Veneziano-type residue functions. The ω production and decay characteristics are presented, and it is found that a ρ-exchange model with absorptive corrections is inadequate to describe the data.

I. INTRODUCTION

The experiment analyzed in this report was performed using a beam of π^+ mesons from the Bevatron incident on the deuterium-filled 72-inch Alvarez bubble chamber of the University of California Lawrence Radiation Laboratory. This exposure was made between August 23, 1966 and September 26, 1966. The incident pion momentum covered the range from 1.1 to 2.4 BeV/c in eight settings. The beam used for this experiment has been described elsewhere.[1] The range-momentum scale factor for charged tracks in the deuterium-filled chamber and the liquid deuterium index of refraction were determined by measuring the range of μ^+'s coming from the decay of stopping π^+ tracks.[2] A total of 264 000 pictures were taken; the incident momentum settings and the exposure size at each setting are given in Table 1. The method for obtaining the path lengths is set forth in Appendix A.

In addition to the film just mentioned, another exposure of π^+ incident on deuterium at incident momenta around 3 BeV/c and 4 BeV/c was made in the spring and summer of 1966 in conjunction with the lower energy exposure which is the subject of this report. In what follows we shall refer to the data taken between 1.1 and 2.4 BeV/c as the low-energy data, and that taken at 3 and 4 BeV/c as the high-energy data.

The main purpose of this experiment was to analyze reactions of the type

$$\pi^+ n \rightarrow p M^o,$$

$$M^o \rightarrow \pi^+\pi^-, \text{ neutrals}$$

$$\text{or } M^o \rightarrow \pi^+\pi^+\pi^-\pi^-, \text{ neutrals}.$$

Table 1. Momentum settings and exposure size.

p (BeV/c)	Number of Pictures (approximately)	Exposure Size (events/μb)
1.10	13 000	.44
1.30	13 000	.44
1.53	50 000	2.55
1.58	13 000	.45
1.70	50 000	3.00
1.86	50 000	2.92
2.15	50 000	2.97
2.37	26 000	.84

Here M^o is a neutral meson, and neutrals means any number of π^o's or γ's. The target neutron is one of the constituents of deuterium. Note that charge symmetry requires that processes such as these be identical in their description to

$$\pi^- p \rightarrow n M^o,$$
$$M^o \rightarrow \pi^+\pi^-, \text{ neutrals}$$
$$\text{or } M^o \rightarrow \pi^+\pi^+\pi^-\pi^-, \text{ neutrals.}$$

A π^- beam incident on a hydrogen target is easily obtainable in practice, but in this case the simultaneous presence of a neutron and the other neutrals in the final state does not allow the momentum of the neutron and that of the other neutrals to be determined separately; hence an analysis of the production and decay characteristics of the meson M^o is not possible. For this reason the experiment was done as a $\pi^+ d$ exposure.

This report deals primarily with the reaction

$$\pi^+ d \rightarrow pp\,\pi^+\pi^-\pi^o,$$

and in particular with the production and decay of η and ω mesons via the reactions

$$\pi^+ d \rightarrow pp\eta,$$
$$\eta \rightarrow \pi^+\pi^-\pi^o$$
$$\pi^+ d \rightarrow pp\omega,$$
$$\omega \rightarrow \pi^+\pi^-\pi^o .$$

Other aspects of this experiment which are being investigated are (a) strange particle production in this exposure[3] and in the higher-

energy exposure,[4] (b) the reactions

$$\pi^+ d \rightarrow pp\,\pi^+\pi^-\ ^{5}$$

and $\pi^+ d \rightarrow pp$, neutrals,[6]

and (c) five- and six-pronged events. Some preliminary reports on this experiment have appeared earlier.[7,8,9,10]

In the high-energy exposure we have collaborated with workers at Purdue University, who have reported on the reaction

$$\pi^+ d \rightarrow pp, \text{ neutrals}\ ^{11}$$

and on four-pronged events.[12]

References 13-25 are a list of papers on thirteen other π^+-deuterium experiments done in bubble chambers, encompassing the range of incident pion momentum from .65 BeV/c to 8 BeV/c; this list is hopefully both exhaustive and current.

We note at this point that information on the scanning, measuring, and fitting of the events on the film is contained in Appendix B, and Appendix E contains a list of the notations used in this report to describe the particle interactions.

II. FINAL STATES AND SEPARATION OF HYPOTHESES

A. The Final State Hypotheses

The three- and four-pronged events were fit to the following reaction hypotheses:

$$\pi^+ d \rightarrow pp\,\pi^+\pi^- \qquad \text{(II.1)}$$

$$\rightarrow pp\,\pi^+\pi^-\pi^o \qquad \text{(II.2)}$$

$$\rightarrow pp\,\pi^+\pi^-\,(mm) \qquad \text{(II.3)}$$

$$\rightarrow pp\,\pi^+\pi^-\,\gamma \qquad \text{(II.4)}$$

$$\rightarrow pp\,K^+K^- \qquad \text{(II.5)}$$

$$\rightarrow np\,\pi^+\pi^+\pi^- \qquad \text{(II.6)}$$

$$\rightarrow p\,\pi^+\pi^+\pi^-\,(mm) \qquad \text{(II.7)}$$

$$\rightarrow \pi^+\pi^+\pi^+\pi^-\,(mm) \qquad \text{(II.8)}$$

$$\rightarrow d\,\pi^+\pi^+\pi^- \qquad \text{(II.9)}$$

$$\rightarrow d\,\pi^+\pi^+\pi^-\pi^o \qquad \text{(II.10)}$$

The details of the fitting procedure have been relegated to Appendix B. There were 103 000 four-pronged events with fits out of the 128 000 events found on the film; of the 93 000 three-pronged events found, 54 000 were measured, and fits were obtained for 44 000 of these. Tables 2 and 3 give the number of events assigned to each reaction as a function of momentum setting, for three- and four-pronged events respectively.

At this point we restrict our interest to those examples of reactions (II.2) and (II.4) which appear as four-pronged event topologies, i.e., those for which both of the final state protons had

Table 2. Number of events assigned to final states vs. beam momentum, for 3-pronged event topology.

Final State	Beam Momentum 1.10	1.30	1.53	1.58	1.70	1.86	2.15	2.37
pp $\pi^+\pi^-$	1 481	1 362	6 755	1 287	--	--	7 491	1 917
pp $\pi^+\pi^-\pi^o$	355	671	4 080	816	--	--	6 824	2 095
pp $\pi^+\pi^-$(mm)	17	44	401	89	--	--	1 855	789
pp $\pi^+\pi^-\gamma$	15	10	73	3	--	--	95	28
ppK^+K^-	0	0	5	4	--	--	182	62
np $\pi^+\pi^+\pi^-$	84	107	822	146	--	--	2 246	802
p $\pi^+\pi^+\pi^-$(mm)	5	8	123	22	--	--	976	443
$\pi^+\pi^+\pi^+\pi^-$(mm)	*	*	*	*	--	--	*	*
d $\pi^+\pi^+\pi^-$	*	*	*	*	--	--	*	*
d $\pi^+\pi^+\pi^-\pi^o$	*	*	*	*	--	--	*	*

* These final states normally do not appear as a 3-pronged topology.

Table 3. Number of events assigned to final states vs. beam momentum, for four-pronged event topology.

Final State	Beam Momentum							
	1.10	1.30	1.53	1.58	1.70	1.86	2.15	2.37
$pp\ \pi^+\pi^-$	1 059	1 041	4 596	720	5 229	4 965	4 517	1 140
$pp\ \pi^+\pi^-\pi^o$	279	535	3 211	559	4 322	4 865	5 553	1 600
$pp\ \pi^+\pi^-$(mm)	21	40	468	99	939	1 311	2 273	858
$pp\ \pi^+\pi^-\gamma$	57	71	319	56	376	336	405	90
ppK^+K^-	0	0	12	4	41	64	106	34
$pn\ \pi^+\pi^+\pi^-$	299	598	5 023	895	6 606	7 544	8 921	2 806
$p\ \pi^+\pi^+\pi^-$(mm)	13	60	819	211	2 286	3 719	6 065	2 172
$\pi^+\pi^+\pi^+\pi^-$(mm)	0	2	62	19	154	236	444	182
$d\ \pi^+\pi^+\pi^-$	11	11	152	13	115	129	187	71
$d\ \pi^+\pi^+\pi^-\pi^o$	3	0	273	61	178	74	71	24

sufficient laboratory momentum to be visible in the bubble chamber. (The lower cutoff on proton laboratory momentum was found to be approximately 85 MeV/c; this momentum yields a track .15 cm long, which is the practical limit of visibility on the film.)

In the missing mass plots in this section, and in the physics data that follow in this report, the events shown have fulfilled the following criteria:

(a) The kinematic confidence level for the fit is greater than 1 per cent,

(b) The confidence level for the ionization fit is greater than 1 per cent,

(c) All track measurements were available for the kinematic fit (i.e., constraint-reduced events were not used).

(d) The event occurred within a preselected fiducial volume of the bubble chamber, and the dip and azimuth of the beam track for the event lay within preselected limits for each momentum setting.

Events fulfilling these criteria will be referred to as "good" events.

B. Separation of the Final States $pp\,\pi^+\pi^-\pi^o$, $pp\,\pi^+\pi^-\gamma$, and $pp\,\pi^+\pi^-$ (mm)

Because it is difficult for a final state like $pp\,\pi^+\pi^-\pi^o$ or $pp\,\pi^+\pi^-$ (mm) to fake a four-constraint fit like $pp\,\pi^+\pi^-$, and because our selection procedure favors four-constraint fits over lower constraint class fits (see Appendix B), the final state $pp\,\pi^+\pi^-$ is likely to be free of other final states, and complete. This was corroborated by generating Monte Carlo events (see Appendix B) for reactions (II.1)

through (II.7) which were fitted and separated like the real events.

The final state pp $\pi^+\pi^-\gamma$ arises only via the reactions

$$\pi^+ d \rightarrow pp\eta \text{ (or } \eta'),$$
$$\eta \text{ (or } \eta') \rightarrow \pi^+\pi^-\gamma .$$

From the known branching ratio

$$(\eta \rightarrow \pi^+\pi^-\gamma)/(\eta \rightarrow \pi^+\pi^-\pi^o) = .23$$ [26]

and from the $\lesssim 400$ η events in the final state pp $\pi^+\pi^-\pi^o$, at most 150 events should be found in the channel pp $\pi^+\pi^-\gamma$ (the η' production cross section is much smaller than the η production cross section). Although the separation procedure of Appendix B favors assigning pp $\pi^+\pi^-\gamma$ events to the pp $\pi^+\pi^-\pi^o$ final state, there are still about 800 "good" pp $\pi^+\pi^-\gamma$ events, most of which seem to belong to the final state pp $\pi^+\pi^-$, as evidenced by an apparent ρ^o peak in the $\pi^+\pi^-\gamma$ mass spectrum for these events; they also seem to contain about 30 η events. Compensation for the estimated number of pp $\pi^+\pi^-\gamma$ events in the p p $\pi^+\pi^-\pi^o$ sample has been made in calculating the cross section for $\pi^+ d \rightarrow pp\eta$.

The separation of pp $\pi^+\pi^-\pi^o$ from pp $\pi^+\pi^-$ (mm) can be estimated from Figure 1, which shows the mm^2 distribution for all "good" events called pp $\pi^+\pi^-\pi^o$, pp $\pi^+\pi^-\gamma$, or pp $\pi^+\pi^-$ (mm). The pp $\pi^+\pi^-\gamma$ and pp $\pi^+\pi^-$ (mm) events are also shown separately on the lower histogram. The sharp cutoff in the missing mass spectrum for pp $\pi^+\pi^-$ (mm) events at $mm^2 = (2m_{\pi^o})^2 = .072$ BeV^2 indicates that some of the missing-mass events are being called pp $\pi^+\pi^-\pi^o$ events; from the figure, an estimate of 4 per cent contamination in the pp $\pi^+\pi^-\pi^o$ sample from

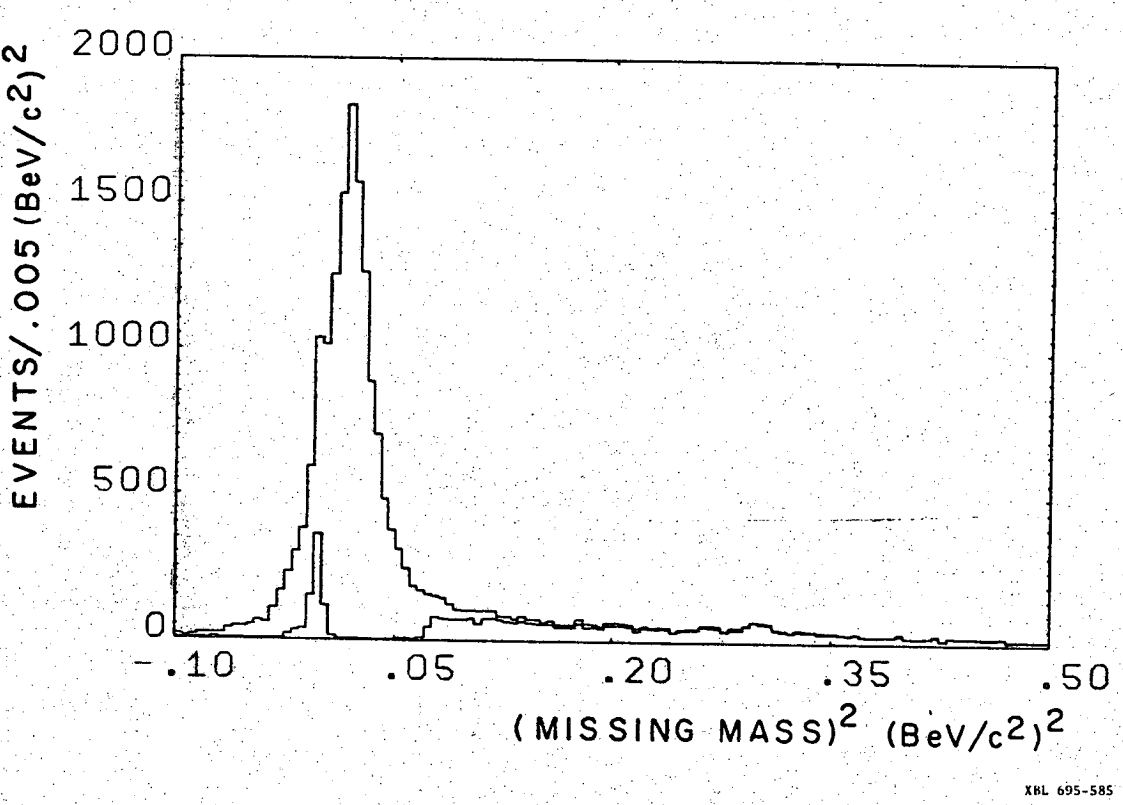

Figure 1. Missing-mass-squared distribution for 19 553 "good" events from the final states p p $\pi^+ \pi^- \pi^o$, p p $\pi^+ \pi^- \gamma$, and p p $\pi^+ \pi^-$ (mm). The lower histogram is the distribution for the latter two reactions only.

missing-mass events can be made by drawing a smoother falloff of the mm^2 histogram for the missing-mass events. However, an admixture of missing-mass events in the pp $\pi^+\pi^-\pi^o$ sample will not affect the η and ω cross section determination, as long as the admixture is distributed more or less uniformly over the $\pi^+\pi^-\pi^o$ mass spectrum (see Section IV).

C. Separation of the Final States pp $\pi^+\pi^-\pi^o$ and np $\pi^+\pi^+\pi^-$

These two final states are often ambiguous with each other because they are both one-constraint fits. The problem is to identify one charged track and the missing neutral particle as a $p\pi^o$ combination or $n\pi^+$, all other tracks in the two fits being the same. The identification of a track as a proton vs. a π^+ in this experiment is greatly aided by the use of pulse height information from the Spiral Reader to make a fit to the expected bubble density for each track-mass interpretation (see Appendix B). This is particularly helpful for the four-pronged events at our beam momentum, where a typical outgoing track has a laboratory momentum of 500 MeV/c, at which momentum a π^+ is easily distinguished from a proton by bubble density.

However, for high-momentum tracks ($p_{lab} > 1200$ MeV/c) a proton and a π^+ are hard to distinguish by ionization. If, in addition, the momenta of the neutral and the charged track have about the same value, p, then the only constraint in the fit, that of energy conservation, determines the value of

$$\sqrt{p^2 + m_+^2} + \sqrt{p^2 + m_o^2} ,$$

where m_+ is the hypothesized mass of the charged track, and m_o is

that of the neutral track. This expression has the same value for $m_+ = m_\pi$, $m_o = m_n$ as for $m_+ = m_p$, $m_o = m_\pi$. In this case, there is no distinction in the kinematical fit between np $\pi^+\pi^+\pi^-$ and pp $\pi^+\pi^-\pi^o$.

A sensitive test of the separation of these two final states is made possible by the presence of strong η and ω signals in the $\pi^+\pi^-\pi^o$ spectrum from the reaction pp $\pi^+\pi^-\pi^o$. There are 15 403 "good" pp $\pi^+\pi^-\pi^o$ four-pronged events, of which 3 079 also fit the hypothesis np $\pi^+\pi^+\pi^-$. Figure 2a shows the $\pi^+\pi^-\pi^o$ mass spectrum for "good" pp $\pi^+\pi^-\pi^o$ events with no fit to the np $\pi^+\pi^+\pi^-$ hypothesis; Figure 2b shows the 3-pion mass spectrum for the pp $\pi^+\pi^-\pi^o$ events which also fit np $\pi^+\pi^+\pi^-$. From the reduced signal-to-background ratio in Figure 2b with respect to 2a, it is estimated that 20 per cent of the events in Figure 2b are actually np $\pi^+\pi^+\pi^-$ events, so that about .20 · 3000 = 600 events of the ~ 15 000 pp $\pi^+\pi^-\pi^o$ events, or approximately 4 per cent are actually np $\pi^+\pi^+\pi^-$ events. This estimate will be used in the η and ω cross section determinations.

An estimate can also be made of the loss of pp $\pi^+\pi^-\pi^o$ events that are called np $\pi^+\pi^+\pi^-$ events. Of the 22 686 "good" np $\pi^+\pi^+\pi^-$ events, 2 602 have a second-best fit to pp $\pi^+\pi^-\pi^o$; Figure 3 shows the $\pi^+\pi^-\pi^o$ mass spectrum for these events when interpreted as the pp $\pi^+\pi^-\pi^o$ final state. The total absence of an η or ω signal in these events allows the conclusion that there is effectively no contamination of the np $\pi^+\pi^+\pi^-$ final state by pp $\pi^+\pi^-\pi^o$ events, that is, no loss of pp $\pi^+\pi^-\pi^o$ events into the np $\pi^+\pi^+\pi^-$ channel.

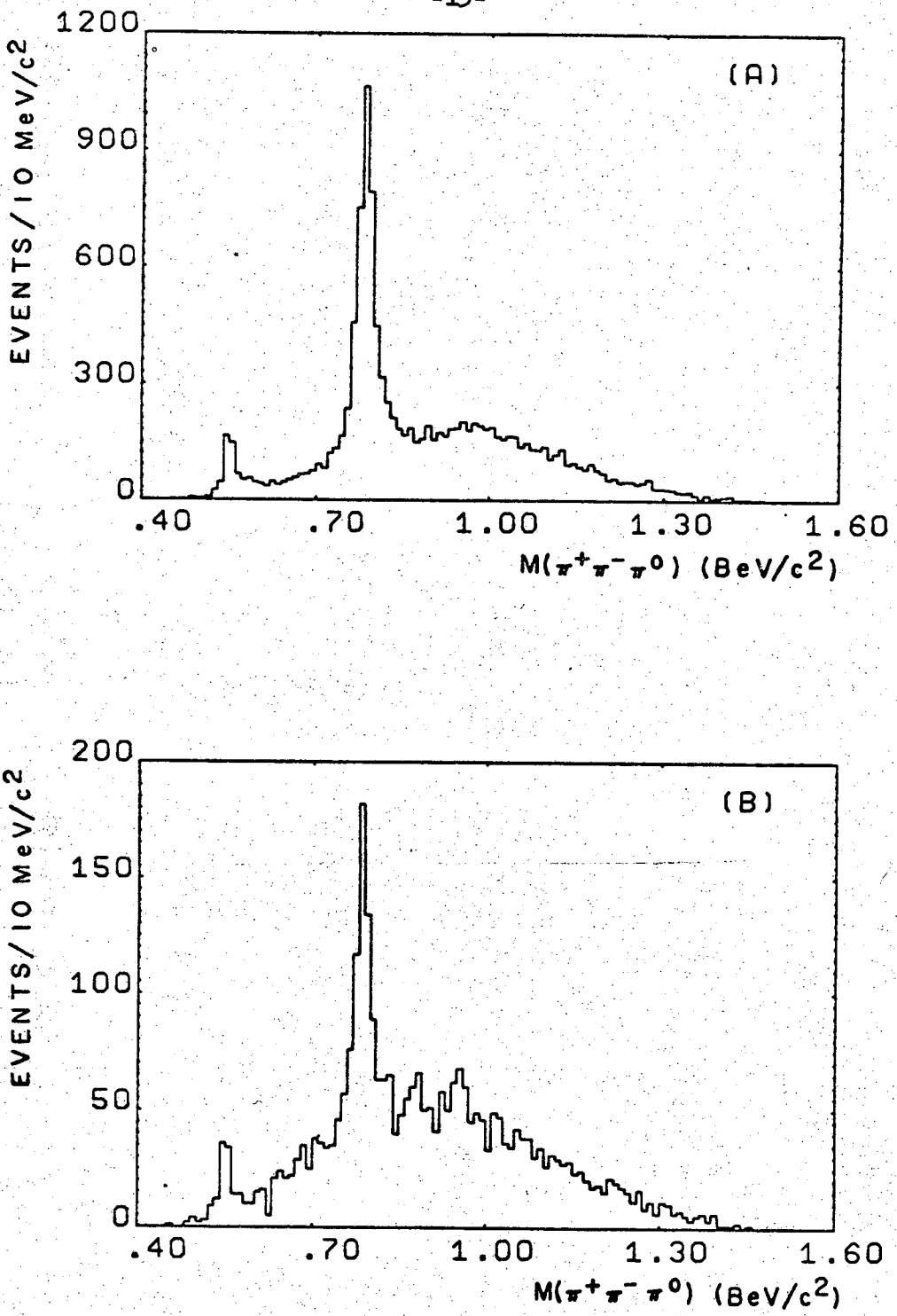

XBL 695-588

Figure 2. $\pi^+\pi^-\pi^0$ mass, a) for 12 324 "good" p p π^+ π^- π^0 events with no fit to the n p π^+ π^+ π^- final state, and b) for 3 079 "good" p p π^+ π^- π^0 events also fitting n p π^+ π^+ π^-.

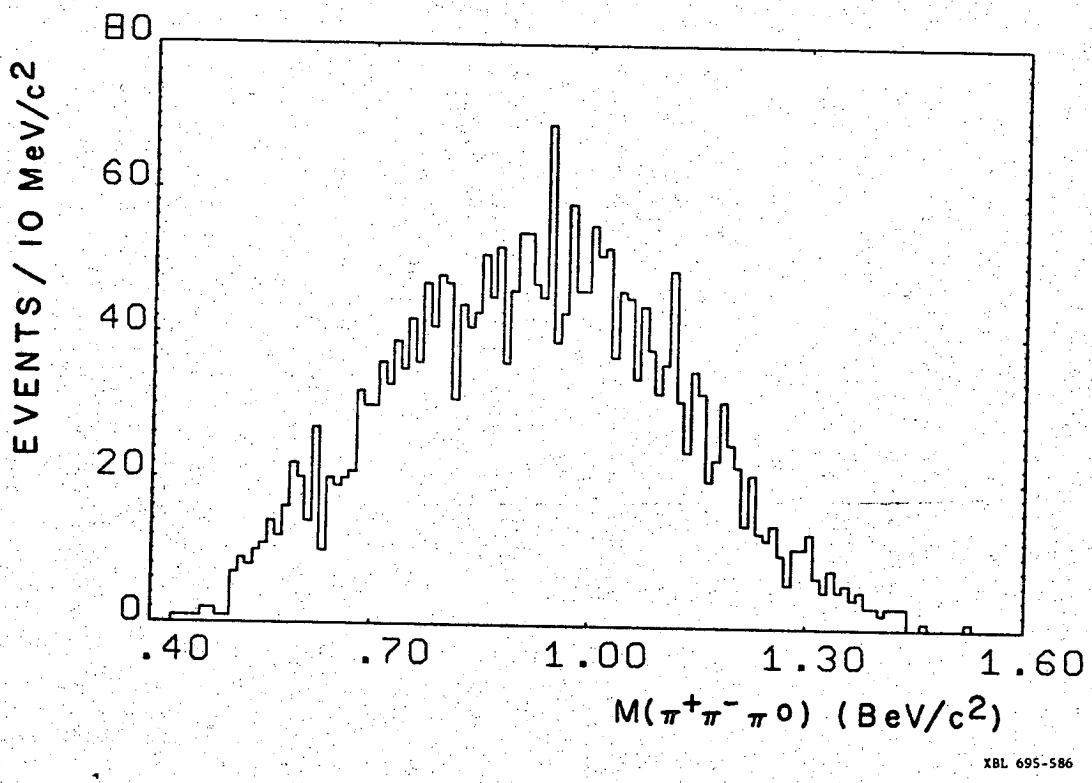

Figure 3. $\pi^+\pi^-\pi^0$ mass spectrum for 2 602 events fitting best to the final state n p π^+ π^+ π^- and second best to p p π^+ π^- π^0. The mass spectrum is obtained when the events are interpreted as the latter channel.

D. Missing-Mass and Confidence Level Distributions for pp $\pi^+\pi^-\pi^o$ Events

Figure 4 shows the mm^2 distribution for "good" pp $\pi^+\pi^-\pi^o$ four-pronged events. In Figure 5 are shown the confidence level distributions for the kinematic and ionization fits separately. At this point we remark again that events for which either the kinematic or ionization confidence level is less than .01 (the leftmost bin of Figure 5a and b) are not included in the sample of "good" events.

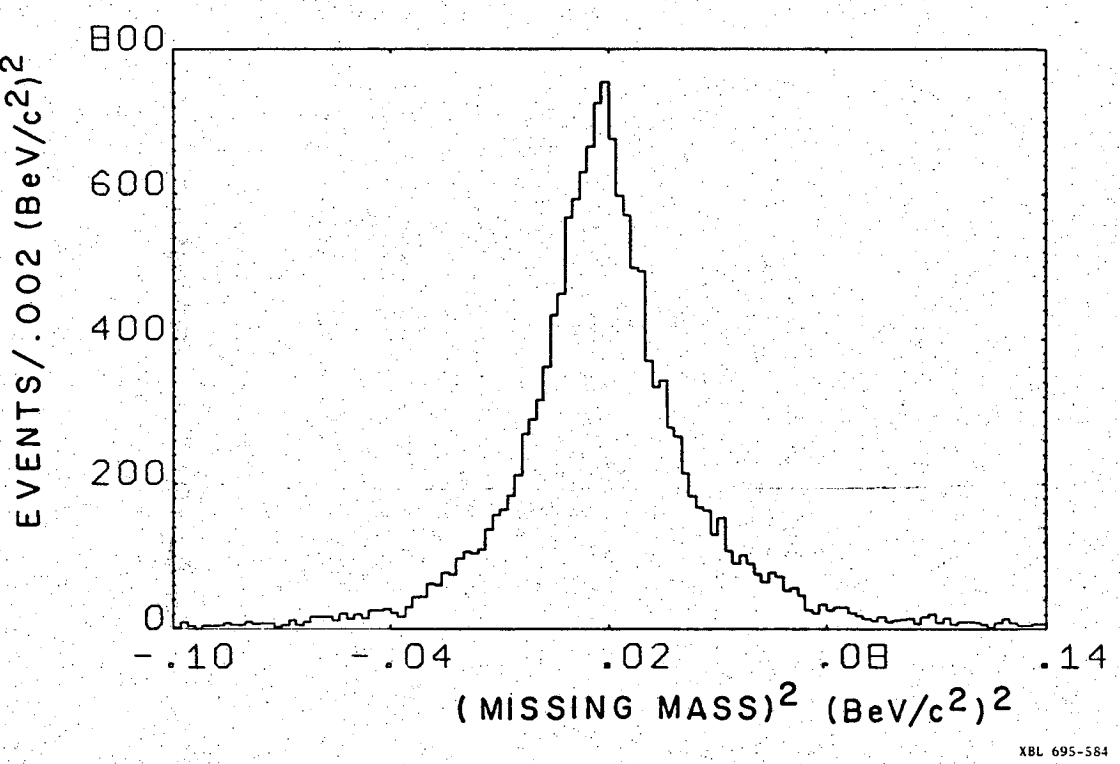

Figure 4. Missing-mass-squared distribution for 14 829 "good" $p\,p\,\pi^+\,\pi^-\,\pi^o$ events.

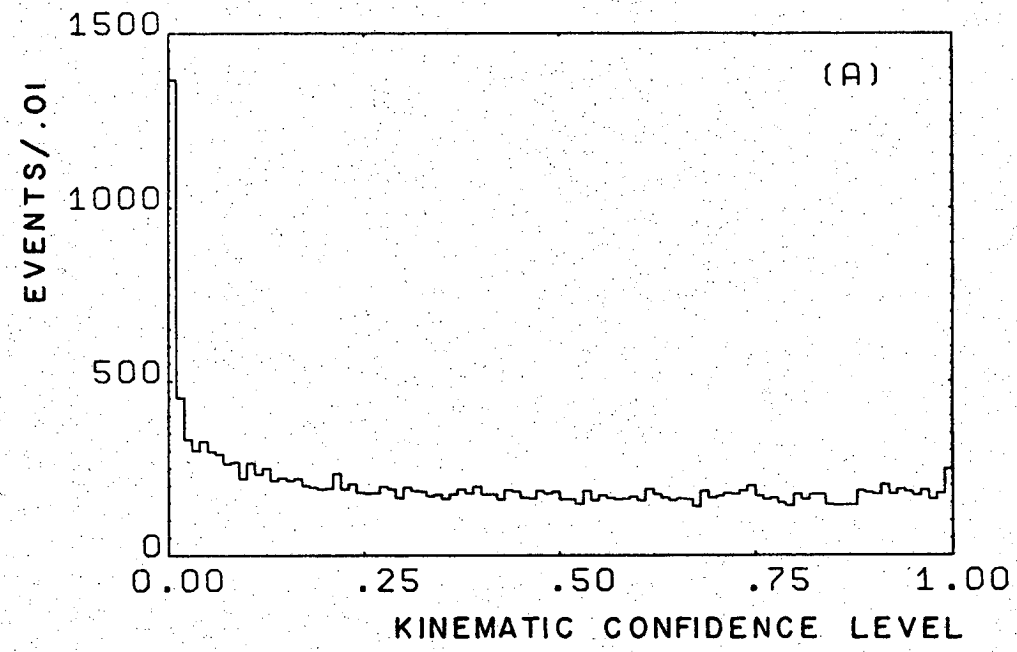

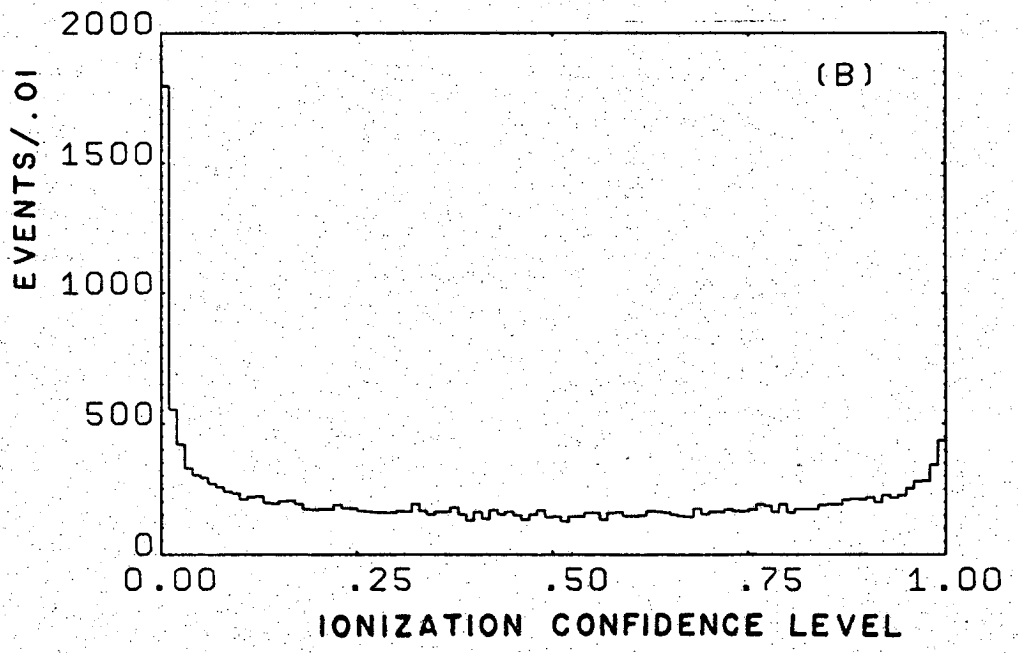

XBL 695-587

Figure 5. a) Kinematic confidence level and b) ionization confidence level for 20 924 events assigned to the final state p p π^+ π^- π^o.

III. THE DEUTERON TARGET

The use of deuterium in the bubble chamber in this experiment is, of course, necessitated by the need for a neutron target. The deuteron is a lightly bound composite of a proton and a neutron, mostly in an S-wave,[27] spin 1 configuration. Although the binding energy of the deuteron is only 2.2 MeV, a number of important effects must be taken into account when using the neutron in the deuteron as the target particle.

A. The Hulthén Wave Function and Spectator Momentum Distributions

A wave function commonly used to describe the separation r of the nucleons in the deuteron is that proposed by Hulthén.[28] It is

$$\psi(r) = C(e^{-\alpha r} - e^{-\beta r})/r \ , \qquad \text{(III.1)}$$

where

$$\int \psi^2(r) r^2 dr = 1 \ . \qquad \text{(III.2)}$$

Here C is the normalization constant fixed to satisfy equation (III.2); it has the value

$$C^2 = 2\alpha\beta(\alpha + \beta)/(\alpha - \beta)^2 \qquad \text{(III.3)}$$

$$\alpha = 45.5 \text{ MeV} = (4.33 \text{ fermi})^{-1} = \sqrt{2\mu B} \ , \qquad \text{(III.4)}$$

with

μ = deuteron reduced mass = $M_{nucleon}/2$

B = deuteron binding energy = 2.2 MeV .

β is often taken to be $\beta = 7\alpha$ [29] or $\beta = 5.18\alpha$.[30] In all applications

of the Hulthén wave function in this report, the average value $\beta = 6.09\,\alpha$ will be used.

The Fourier transform of $\psi(r)$ gives the distribution $\Phi(p)$ of the momentum of the two nucleons in the deuteron; it is

$$p^2\Phi^2(p) = C'p^2\left[\, 1/(p^2+\alpha^2) - 1/(p^2+\beta^2) \,\right]^2, \qquad \text{(III.5)}$$

where

$$\int \Phi^2(p)p^2dp = 1 \ .$$

Figure 6 shows $\psi^2(r)r^2$ and $\Phi^2(p)p^2$; the curves show how much of the wave function is concentrated at each value of nucleon separation r and momentum p.

Experimentally $p^2\Phi^2(p)$ can be measured when the impulse approximation for the π^+d collisions is assumed. This means that the π^+ is assumed to interact with only one of the nucleons in the deuteron, the other nucleon going off after the collision with the same momentum it had before the collision.

For the reaction $\pi^+n(p) \rightarrow (p)p\ \pi^+\pi^-\pi^o$ the notation (p) means that one final-state proton is assumed to be a "spectator" to the collision between the π^+ and the neutron. The final-state proton with the lower laboratory momentum is taken to be the spectator. Figure 7 shows the experimental distribution of spectator momentum; the steep cutoff in the distribution around 85 MeV/c is due to the fact that only events with two visible protons (four-pronged events) are used. The curve is the Hulthén distribution $p^2\Phi^2(p)$ normalized to have the same area as the histogram between p = 110 MeV/c and 160 MeV/c.

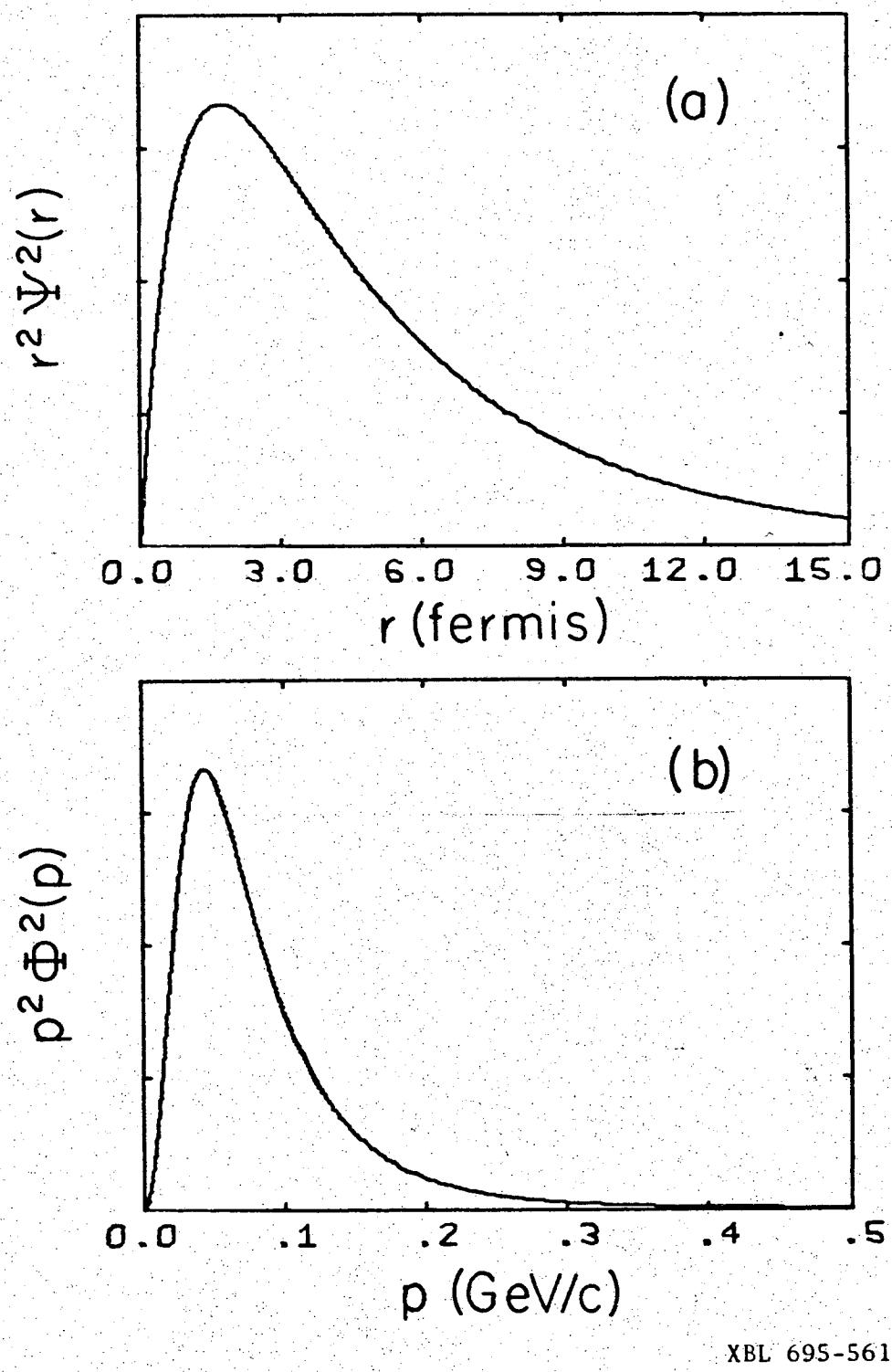

XBL 695-561

Figure 6. Distribution of a) deuteron radial separation and b) nucleon momentum in the deuteron, using the Hulthén wave function with $\beta = 5.09\alpha$.

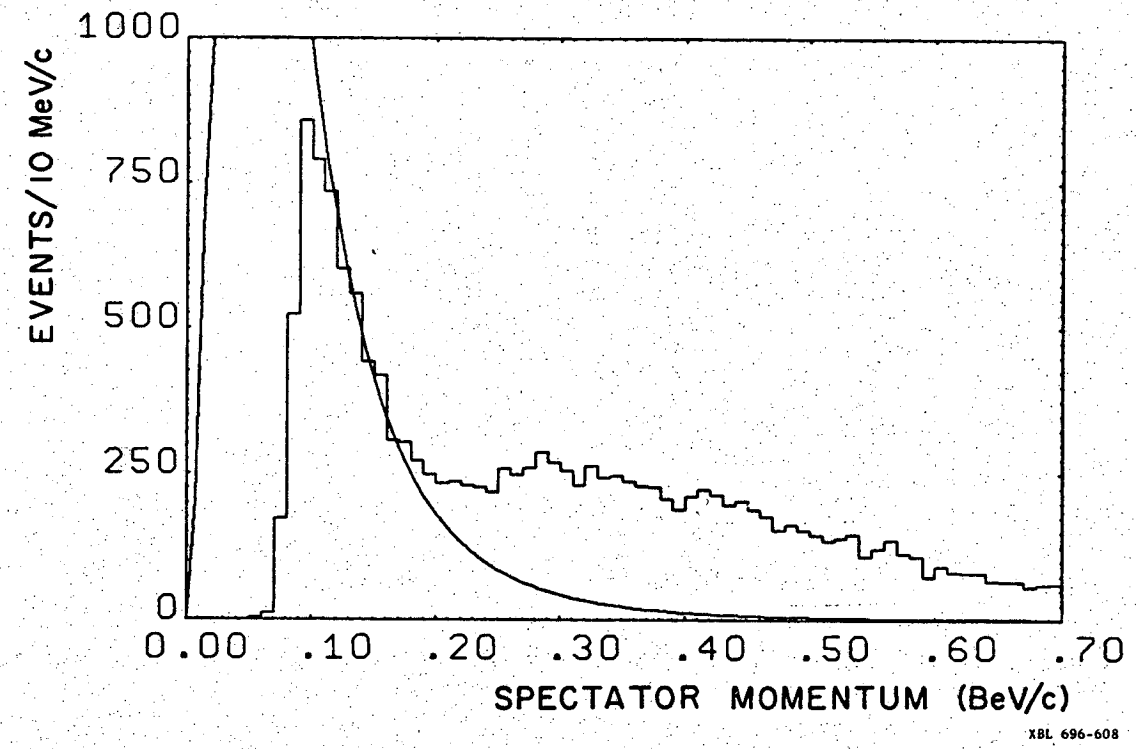

Figure 7. Laboratory momentum of lower-momentum proton in the final state $p\,p\,\pi^+\,\pi^-\,\pi^o$ for 4-pronged events; the curve is the Hulthén distribution normalized to have the same area as the histogram in the interval (110 MeV/c < p < 160 MeV/c).

A deviation from the Hulthén wave function is exhibited as an excess of events with high momentum, that is with momentum greater than 300 MeV/c, which is the practical upper cutoff of the Hulthén distribution. Forty-four per cent of the four-pronged events in Figure 7 have momentum greater than 300 MeV/c.

The excess of high-momentum spectators could be explained by one or more of the following conjectures:

(a) a breakdown of the impulse approximation; that is, high-momentum spectators (p greater than 300 MeV/c) arise from collisions on the entire deuteron,

(b) rescattering of one or more of the final-state particles on the spectator nucleon,

(c) contamination of the (p)p $\pi^+\pi^-\pi^o$ final state by misidentified events belonging to another final state, in which case some of the spectator protons need not even be protons,

(d) inadequacy of the Hulthén wave function.

Points (b) and (c) can be checked by studying the spectator momentum distribution as a function of the $\pi^+\pi^-\pi^o$ mass. If the excess of high-momentum spectators is due to scattering of the final-state pions on the spectator, then conceivably the scattering might be different when the three pions form a resonance (η or ω), assuming that the resonance decays after it has traveled far enough to get outside the deuteron volume, which is a sphere a few fermis in radius (see Figure 6). For an η (or ω) of width 2.6 keV (12.6 MeV) [26] produced with a typical laboratory momentum of 800 MeV/c, the mean decay length is 110 000 fermis (16 fermis), so that these resonances decay

after leaving the deuteron volume. Figure 8a shows the $\pi^+\pi^-\pi^o$ mass vs. spectator momentum. η and ω production is seen to persist even at high spectator momentum; since these resonance signals are unique signatures for the pp $\pi^+\pi^-\pi^o$ final state, it is clear that contamination is not the only source of high-momentum spectators. Figure 8b shows the spectator momentum distribution for events in the ω band ($760 < m(3\pi) < 810$ MeV/c^2). It is seen that this spectator distribution conforms somewhat better to the Hulthén curve than that for all of the pp $\pi^+\pi^-\pi^o$ events; in fact only 34 per cent of the events in the ω band have momentum greater than 300 MeV/c, whereas this fraction is 44 per cent for the entire sample of "good" pp $\pi^+\pi^-\pi^o$ events. This may indicate that a final-state ω is less likely to rescatter on the spectator proton than three unassociated pions, or it may simply indicate that some of the high-momentum spectators are caused by contamination from other final states, since any contamination would form a smaller fraction of the events in the resonance band than of the entire sample of events.

The spectator momentum distributions for other final states can also be examined and compared with the Hulthén distribution; if other final states have different spectator momentum distributions, this might shed some light on the problem of rescattering. Figure 9a shows the spectator momentum for "good" four-pronged events of the final state pp $\pi^+\pi^-$; the curve is the Hulthén distribution normalized to have the same area as the histogram between 110 MeV/c and 160 MeV/c. The fraction of these four-pronged events with spectator momentum greater than 300 MeV/c is 36 per cent, compared to 44 per cent for the

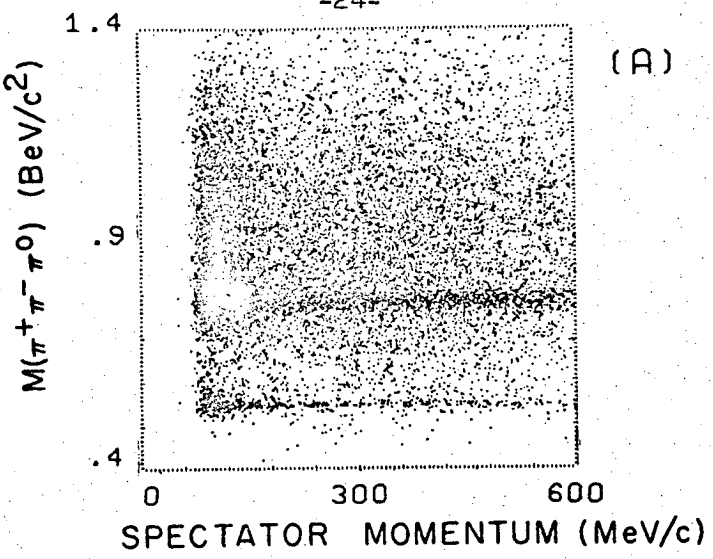

XBL 696-611

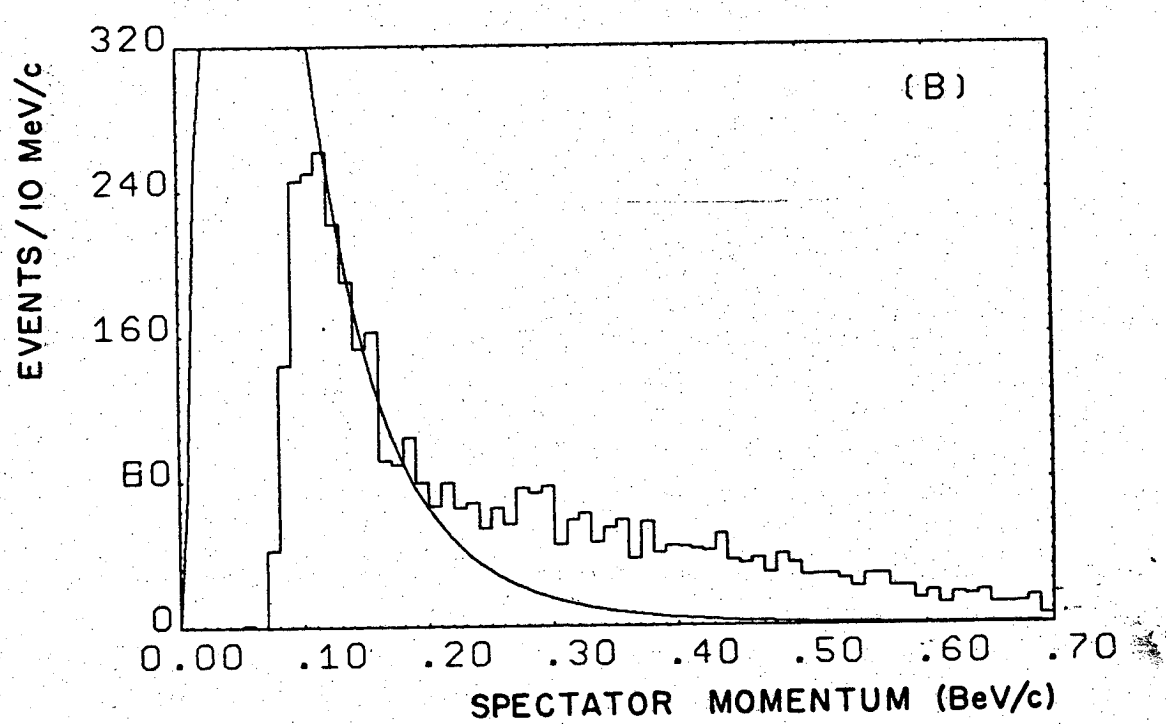

Figure 8. a) Three-pion mass vs. spectator laboratory momentum and b) spectator laboratory momentum distribution for events in the ω band (760 MeV/c^2 < m(3π) < 810 MeV/c^2) for "good" 4-pronged events from the final state p p π^+ π^- π^0. The curve in b) is the Hulthén distribution normalized to have the same area as the histogram in the interval (110 MeV/c < p < 160 MeV/c).

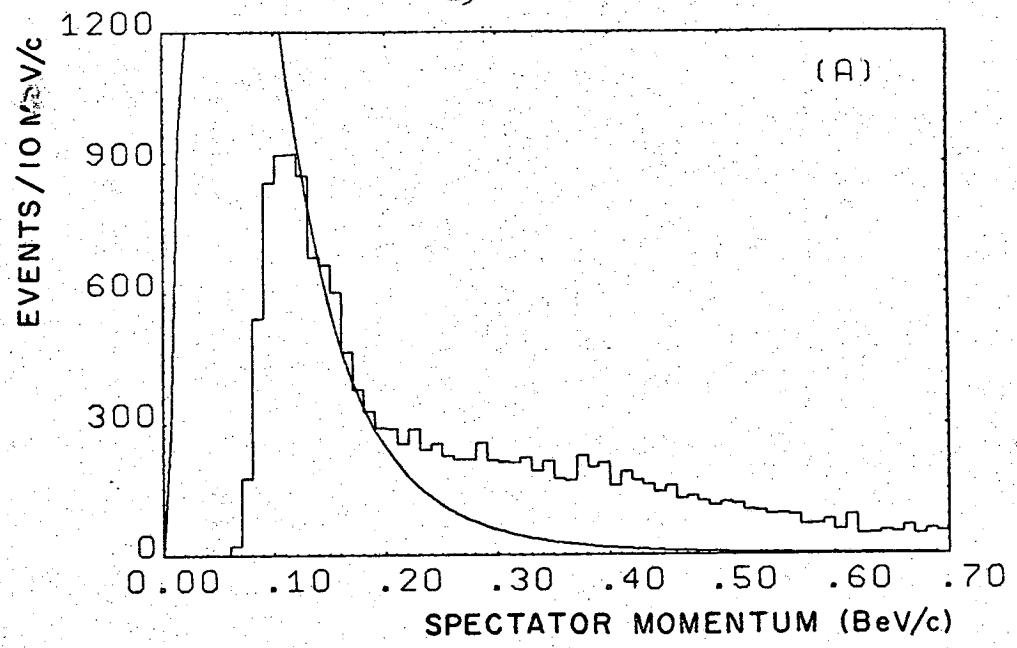

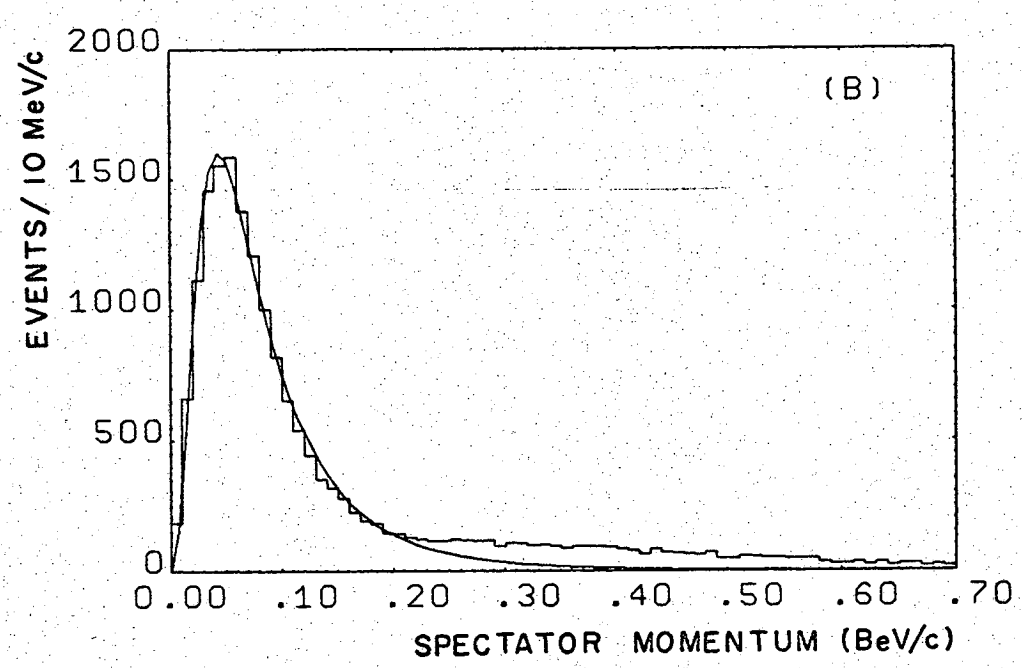

XBL 696-612

Figure 9. Spectator momentum distribution for a) "good" 4-pronged events from the final state p p π^+ π^- and b) "good" events from the final state (n) p π^+ π^+ π^-. The curves are the Hulthén distribution, normalized to have the same area as the histogram in the interval (110 MeV/c < p < 160 MeV/c) for a) and (0 < p < 160 MeV/c) for b).

four-pronged pp $\pi^+\pi^-\pi^o$ events. Figure 9b is the neutron spectator momentum distribution for "good" events in the channel (n)p $\pi^+\pi^+\pi^-$. These events are separated from the (p)n $\pi^+\pi^+\pi^-$ final state by taking the lower-momentum nucleon to be the spectator. The (n)p $\pi^+\pi^+\pi^-$ final state appears almost always as a four-pronged topology, since the charged tracks are almost invariably visible (no examples of this final state were found in the three-pronged events). Since this sample of spectators is complete, the Hulthén curve is normalized to have the area of the histogram between 0 and 160 MeV/c. In order to compare the fraction of events with fast spectators to the fractions obtained for the above-mentioned four-pronged events with visible proton spectators, we take the ratio of the events with spectator momentum greater than 300 MeV/c to the number of events with spectators of momentum greater than 85 MeV/c. The fraction of "fast" spectators is here only 31 per cent. The fact that final states with neutron spectators have fewer high-momentum spectators has also been noted in strange-particle production in this experiment.[3] Benson[21d] has conjectured on the possible reasons for different final states having different spectator momentum distributions.

B. The Flux Factor, Spectator-Beam Angle, and c.m. Energy Smearing

The internal motion of the two nucleons bound in the deuteron gives rise to two interesting effects. We first discuss the effect of this motion on the experimentally measured angle between the spectator nucleon and the incoming pion beam.

The proton and neutron bound in the deuteron move at random in opposite directions with momentum given by a function like the Hulthén distribution. Because of the random nature of the motion, some authors[12, 21d] have stated incorrectly that the experimentally measured angle between the beam and the spectator nucleon should have an isotropic distribution. This statement, however, fails to take into account the fact that when the target particle is moving toward the beam, there is a greater particle flux and hence a higher reaction rate than when the target particle is receding from the beam. Let θ be the angle between the spectator and the beam. Since the target nucleon and the spectator nucleon in the deuteron move in opposite directions in order to conserve momentum, this means that there will be more events for which $\cos\theta$ is greater than 0 than for $\cos\theta$ less than 0.

The experimental distribution can be predicted using the invariant flux factor of Møller[31] to account for the variation of particle flux with the relative motion of the beam and the target particle; it is

$$f = \sqrt{(p_b \cdot p_t)^2 - m_b^2 m_t^2}\,/(m_b m_t) \qquad \text{(III.6)}$$

Here the momenta p_b and p_t are 4-vectors, and the subscripts b and t refer to the beam and the target particle, respectively. The 4-vector of the target particle is taken to be that of the deuteron minus that of the spectator nucleon.

In order to see what sort of distribution is predicted for the cosine of the angle between the spectator and the beam, Monte Carlo calculations were performed and $\cos\theta$ histogrammed for incoming pion momentum of 1.0, 1.5, and 2.0 BeV/c separately, assuming the nucleons

in the deuteron are moving in a random direction with equal and opposite momenta described by the Hulthén distribution. Figure 10 shows the results of the Monte Carlo experiment performed for a beam momentum of 2.0 BeV/c. Figure 10a is the histogram of cos θ for all events, and Figure 10b is that for proton spectator laboratory momentum greater than 85 MeV/c, corresponding to the four-pronged events of this report. The nonisotropy of the distributions is evident. In fact, very similar histograms are obtained for all three Monte Carlo experiments (p_{beam} = 1.0, 1.5, and 2.0 BeV/c). The histograms for incident momentum between 1.0 and 2.0 BeV/c are well approximated by a linear dependence on cos θ; it is

$$f(\cos\theta) = 1 + .10 \cos\theta \qquad \text{(III.7)}$$

for all events, and

$$f(\cos\theta) = 1 + .16 \cos\theta \qquad \text{(III.8)}$$

for events with spectator momentum greater than 85 MeV/c.

Figure 11 displays the comparison between the experimental distribution in cos θ (the angle between the spectator and the beam) and the distribution given by the flux factor. Figure 11a shows the distribution in cos θ for all "good" events of the final state $pp\pi^+\pi^-\pi^o$; the straight line is equation (III.8) normalized to have the same area as the histogram. In Figure 11b only the events with spectator momentum less than 300 MeV/c are included, and here it is seen that the agreement between the data and the flux factor prediction is good. The spectator distribution of Figure 7 and the cos θ

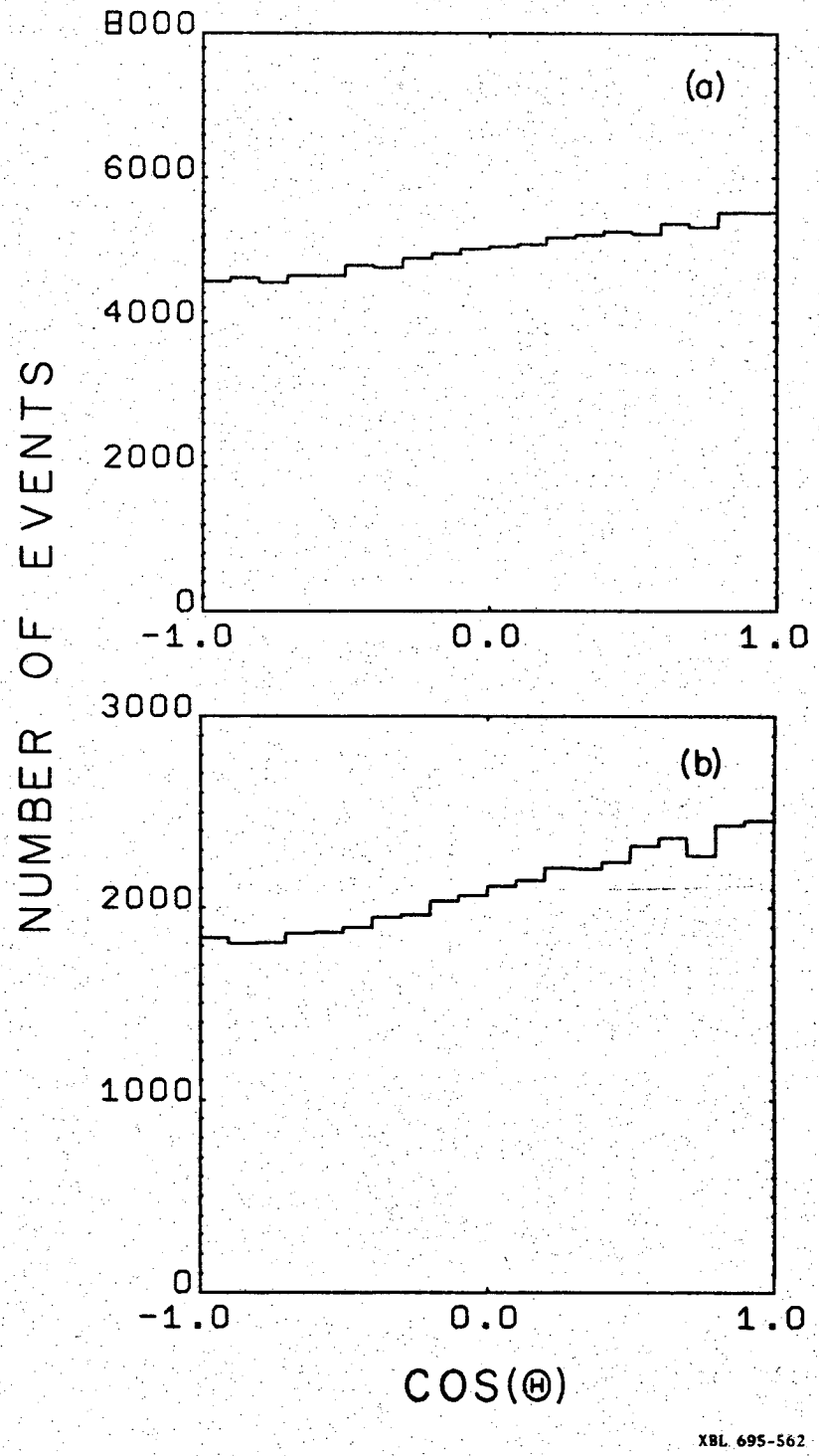

Figure 10. Distribution of cosine between beam and spectator nucleon for a $\pi^+ d$ Monte Carlo experiment of 100 000 events with beam momentum of 2.0 BeV/c, taking the Møller flux factor into account. a) All events, and b) events with spectator momentum greater than 85 MeV/c.

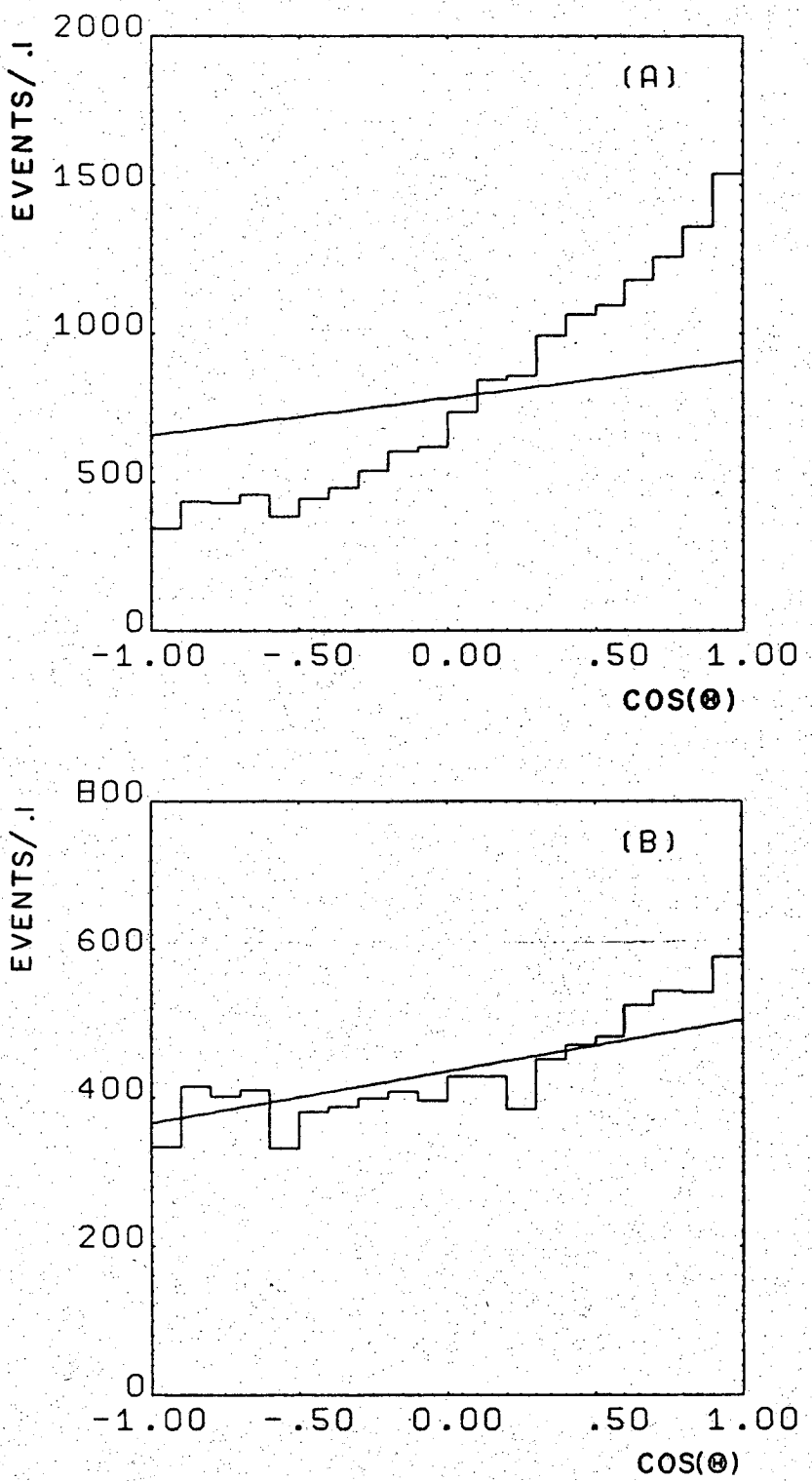

Figure 11. Distribution of cosine between beam and spectator proton for "good" 4-pronged events from the final state p p π^+ π^- π^o. a) All events, and b) events with spectator momentum less than 300 MeV/c. The curves are equation (III.8) normalized to have the same area as the histograms in a) and b).

distribution of Figure 11b indicate that events with spectator momentum less than 300 MeV/c conform well to the expectations of the impulse model.

It should be emphasized that the above prediction for the distribution of $\cos\theta$ holds only if the cross section is assumed to be constant over the range of c.m. energies produced in the collisions. This is because the number of events is proportional to the particle flux times the cross section. However, the assumption of roughly constant cross section is valid for the pp $\pi^+\pi^-\pi^o$ channel, as can be inferred from Table 3 and the fact that the sum of the cross sections for the channels pp $\pi^+\pi^-$, pp $\pi^+\pi^-\pi^o$, pp $\pi^+\pi^-\gamma$, and pp $\pi^+\pi^-$ (mm) is roughly constant over the energy range of this experiment (see Section IV).

Another important effect arising from the motion of the nucleons in the deuteron is the smearing of the center-of-mass energy distribution. In a collision of a beam with a stationary target nucleon, there is of course a unique c.m. energy corresponding to the beam momentum. When one of the nucleons in the deuteron is the target, however, there results a broad spectrum of c.m. energies due to the fact that the target nucleon has a range of momentum and is moving in a random direction with respect to the beam.

Figure 12 shows the distribution of c.m. energies obtained in the Monte Carlo experiment above for a beam of 2.0 BeV/c pions incident on one of the nucleons in the deuteron; the Hulthén distribution is used for the momentum distribution of the nucleons, and the Møller flux factor is included. The c.m. energy for the collision is

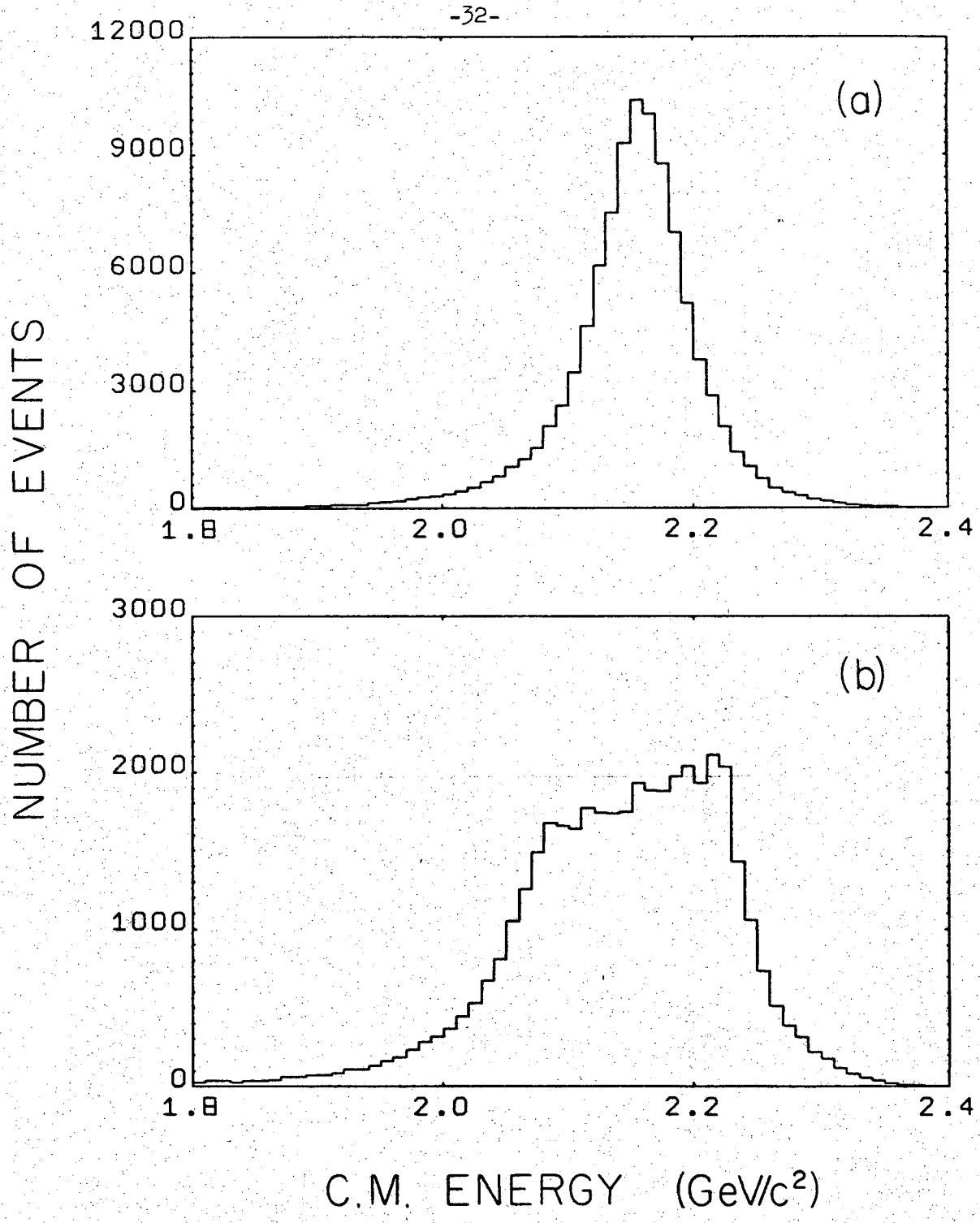

XBL 695-564

Figure 12. Distribution of c.m. energy for a $\pi^+ d$ Monte Carlo experiment of 100,000 events with beam momentum of 2.0 BeV/c, obtained using the Butler distribution and the flux factor. a) All events, and b) events with spectator momentum greater than 85 MeV/c.

$$E_{c.m.} = \sqrt{(p_b + p_d - p_s)^2} \qquad \text{(III.9)}$$

The momenta here are 4-vectors, and the subscripts b, d, and s refer to the beam, deuteron, and spectator, respectively. Figure 12a is the c.m. energy distribution for all events, and Figure 12b is that for the events with spectator momentum greater than 85 MeV/c (corresponding to the four-pronged events of the reaction $\pi^+ d \rightarrow pp\ \pi^+\pi^-\pi^o$). The histograms are made assuming a constant cross section over the energy range shown. The motion of the target nucleon results in a c.m. energy spectrum about 300 MeV wide from a single incident beam momentum.

Figure 13 shows the c.m. energy spectrum for all "good" four-pronged events in the final state $pp\ \pi^+\pi^-\pi^o$ with spectator momentum less than 300 MeV/c; the distribution is the product of the cross section with a sum of distributions like that of Figure 12b. It is seen that the eight incident momenta between 1.1 and 2.4 BeV/c yield a fairly uniform coverage of the c.m. energy range from 1.7 to 2.3 BeV.

C. Glauber Screening

In a very intuitive sense one can understand that the cross section for a beam colliding with a deuteron is less than the sum of the cross sections for a collision with each of the two nucleons in the deuteron separately. If the target deuteron is imagined to be two billiard balls close together, then part of the time one of the billiard balls will occlude the other, reducing the effective cross section. Glauber[32] has derived the expression

$$\sigma(\pi d) = \sigma(\pi n) + \sigma(\pi p) - \sigma(\pi n)\sigma(\pi p)/(4\pi < r^2 >), \qquad \text{(III.10)}$$

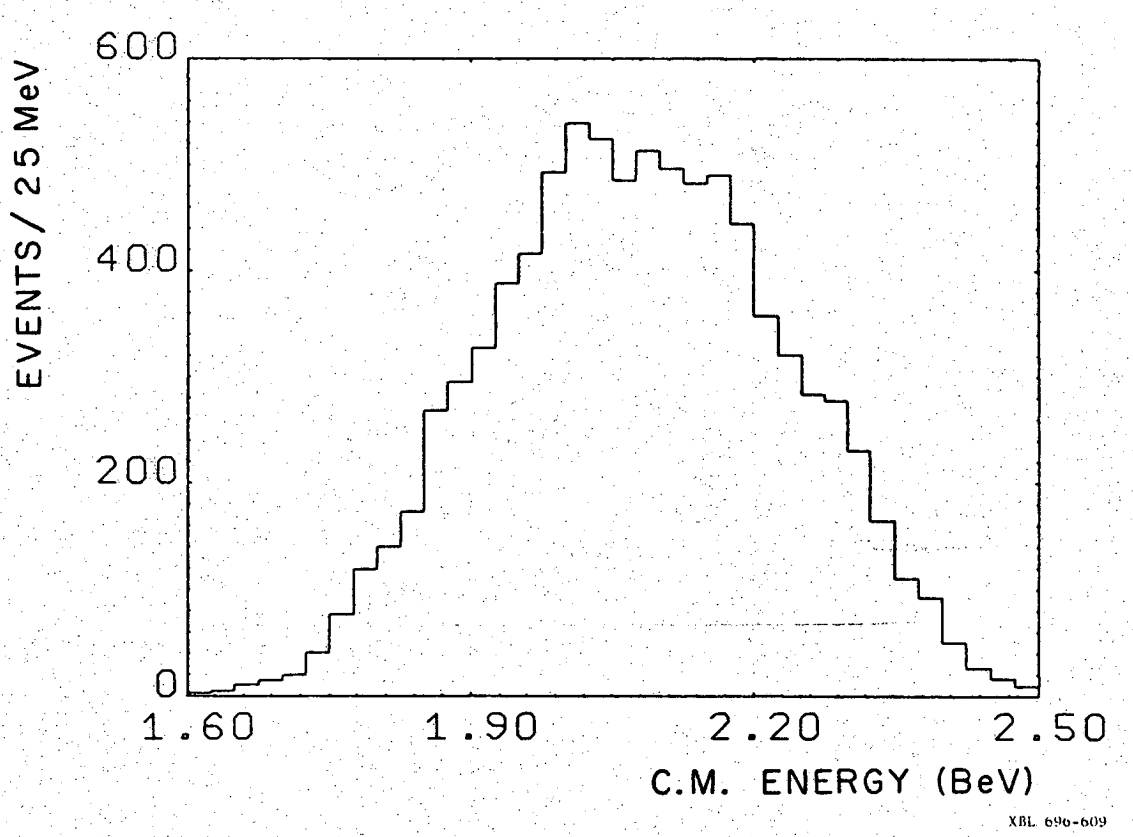

Figure 13. Distribution of c.m. energy for "good" 4-pronged events from the final state (p) p π^+ π^- π^o with spectator momentum less than 300 MeV/c.

where $< r^2 >$ is the average separation between the two nucleons. More recently Wilkin[33] has derived a modified formula which exhibits charge independence; he shows that the correction term should be

$$\left[\sigma(\pi m)\, \sigma(\pi p) - \frac{1}{4}(\sigma(\pi p) - \sigma(\pi m))^2 \right] \Big/ (4\pi < r^2 >) \qquad \text{(III.11)}$$

for a charged-pion beam.

Recently accurate cross sections have been published[34] for π^+ and π^- incident on protons and deuterium over a wide range of energies. From reference 34 it is seen that over the range of incident momenta of this report, we have the total cross sections

$$\sigma(\pi^+ p) \cong 30 \text{ mb}$$

$$\sigma(\pi^- p) \cong 35 \text{ mb} = \sigma(\pi^+ n), \text{ by charge symmetry}$$

Since $\left[\sigma(\pi^+ p) - \sigma(\pi^+ n) \right]^2 \cong (5 \text{ mb})^2$ is small compared to $\sigma(\pi^+ p)\, \sigma(\pi^+ n)$, the correction factor of Wilkin (equation (III.11)) is almost the same as the non-charge-independent correction factor of equation (III.10). From reference 34 it is also seen that over our range of incident momentum,

$$< r^{-2} > \cong .02 \text{ mb}^{-1} .$$

The typical value of the cross section defect in this experiment due to Glauber screening is, from equation (III.10), approximately 1.7 mb; that is, the sum of the $\pi^+ n$ and $\pi^+ p$ cross sections is more than the $\pi^+ d$ cross section by about 1.7 mb, or 2.4 per cent of the total $\pi^+ d$ cross section.

How this cross section defect is to be applied to the various final state channels is unknown. The method of Section IV for obtaining cross sections for η and ω production in the final state $pp\pi^+\pi^-\pi^o$ is valid if the final states (II.1) through (II.4) are each depleted by the same fraction; the similarity of these final states may justify this assumption. At any rate, even if these channels are not all depleted in the same proportion due to Glauber screening, the difference in fractional depletion should not be more than the total depletion itself. Since a difference in depletion among channels (II.1) through (II.4) of ~ 2.4 per cent is much smaller than the statistical cross section errors obtained, the Glauber screening correction will have no effect on the η and ω cross section determination.

D. The Pauli Exclusion Principle and Final States with Two Protons

One can easily see that the Pauli exclusion principle will have an effect on final states containing two protons. In particular, imagine a very glacing ($t \cong 0$) charge-exchange collision of the π^+ beam with the neutron in the deuteron in which the neutron spin is not flipped. After this hypothetical charge-exchange collision there are two protons close together in an S-wave (ignoring the small D-wave component of the deuteron) spin-1 configuration. Since this configuration of two identical fermions is symmetric, however, it is forbidden by the Pauli exclusion principle. Thus it is seen that in the limit of no momentum transfer, such a charge-exchange collision cannot occur in the absence of nucleon spin flip.

The effect of the Pauli exclusion principle on charge-exchange

scattering on the neutron in the deuteron has been calculated for K^+d scattering.[35,36] The expression for the measured cross section when there are two final-state protons is[36]

$$d\sigma/d\Omega = (1 - H(q))(d\sigma/d\Omega)_{nf} + (1 - H(q)/3)(d\sigma/d\Omega)_{sf} \qquad \text{(III.12)}$$

Here the subscripts nf and sf denote the spin-non-flip and spin-flip cross sections respectively. $q = \sqrt{-t}$ is the momentum transfer in the collision, and $H(q)$ is the deuteron form factor, defined as

$$H(q) = \int |\psi(r)|^2 e^{-i\vec{q}\cdot\vec{r}}\, d\vec{r} \qquad \text{(III.13)}$$

Clearly, $H(q) = 1$ for $q = 0$, which is the limiting case considered above. From the first term of equation (III.12) it is clear that there is no non-spin-flip contribution if $q = 0$, as was concluded above.

Equation (III.12) applies to the final state $pp\,\pi^+\pi^-\pi^o$ discussed here; it tells us how to correct the production angular distribution of the three pions for the suppression due to the Pauli principle. Let us restrict our attention to the specific reactions

$$\pi^+ d \rightarrow pp\eta \text{ (or } \omega),$$
$$\eta \text{ (or } \omega) \rightarrow \pi^+\pi^-\pi^o,$$

since it is only the production angular distributions for the resonance events whose exact form we are interested in.

Figure 14 shows the deuteron form factor $H(q)$, calculated using the Hulthén wave function; it has the functional form[35]

$$H(q) = 2\alpha\beta(\alpha + \beta)/(\beta - \alpha)^2 q \cdot \left[\tan^{-1} q/2\alpha + \tan^{-1} q/2\beta - 2\tan^{-1} q/(\alpha + \beta) \right] \qquad \text{(III.14)}$$

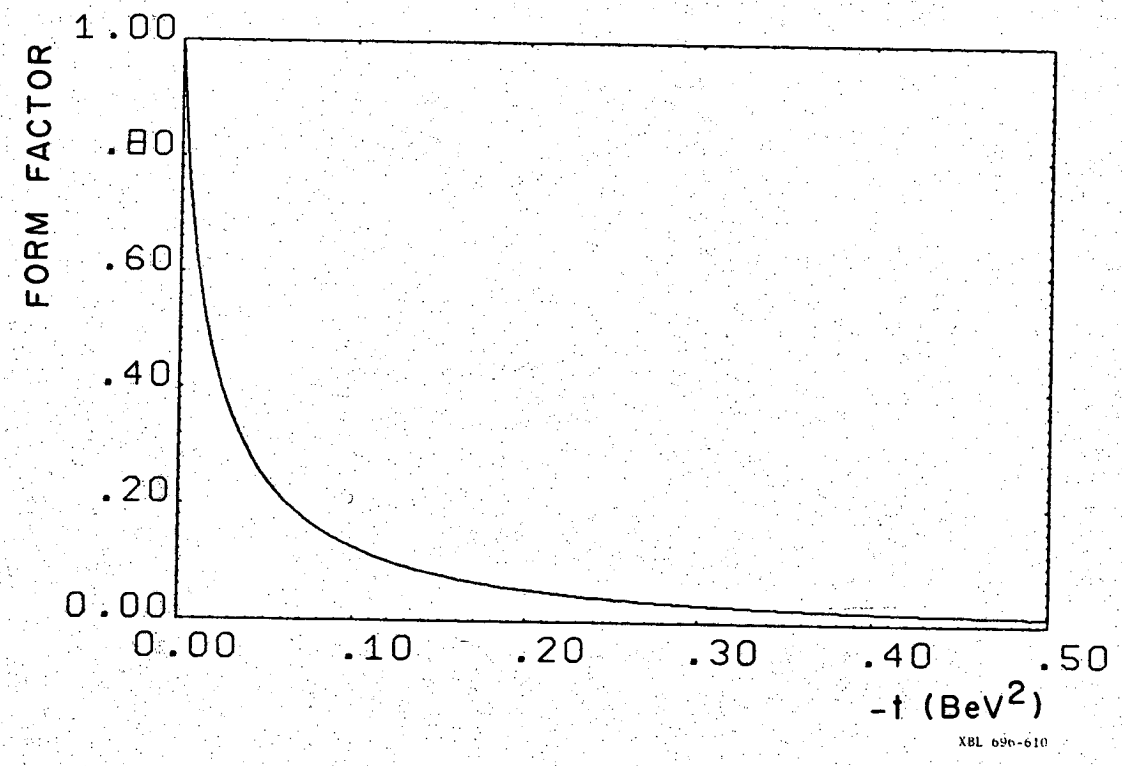

Figure 14. Deuteron form factor vs. momentum-transfer-squared, calculated using the Hulthén wave function.

From the figure it is seen that H(q) is appreciably different from zero only for $-t < .1$ BeV^2, and it is only for this range of momentum-transfer-squared that the effects of the Pauli exclusion principle are important. In Sections V and VI of this report, where η and ω production are discussed, the production angular distributions are presented as distributions of 20 bins in production cosine; in all of the production angular distribution histograms, the two forwardmost of the 20 bins, $(0.8 < \cos\theta < 0.9)$ and $(0.9 < \cos\theta < 1.0)$, cover the momentum-transfer-squared range out to at least .1 BeV^2. Thus it is only the forwardmost two bins that are affected noticeably by the Pauli principle, and the calculation of the effect will, for simplicity, be restricted to this angular region. We define the suppression factors

$$f_{nf} = 1 - H(q), \qquad f_{sf} = 1 - H(q)/3 \qquad \text{(III.15)}$$

taken from equation (III.12). Table 4 gives the value of these factors averaged over the production cosines of the forwardmost two bins (each bin is .1 wide in production cosine) separately for the reactions $\pi^+ d \rightarrow pp\eta$ and $\pi^+ d \rightarrow pp\omega$. It is seen that f_{nf} is significantly less than unity in the production cosine interval (0.9, 1.0) for the energies encountered in this experiment, and thus implies a large correction. The suppression factors are to be treated as detection efficiencies in the production cosine interval indicated, the events in that interval being divided by the appropriate factor (or combination of factors) to get the number of events that would be found if the beam had collided with a free neutron. To make the correction, however, one must know the relative sizes of the spin-flip

Table 4a. Spin-flip and spin-non-flip suppression factors due to the Pauli principle for the two forwardmost production cosine bins for $\pi^+ d \rightarrow pp\omega$.

$E_{c.m.}$ (BeV)	$(0.8 < \cos\theta < 0.9)$		$(0.9 < \cos\theta < 1.0)$	
	f_{nf}	f_{sf}	f_{nf}	f_{sf}
1.8	0.93	0.98	0.91	0.97
1.9	0.93	0.98	0.87	0.96
2.0	0.93	0.98	0.85	0.95
2.1	0.94	0.98	0.83	0.95
2.2	0.95	0.98	0.83	0.94
2.3	0.96	0.99	0.83	0.94
2.4	0.96	0.99	0.84	0.95

Table 4b. Spin-flip and spin-non-flip suppression factors due to the Pauli principle for the two forwardmost production cosine bins for $\pi^+ d \rightarrow pp\eta$.

$E_{c.m.}$	$(0.8 < \cos\theta < 0.9)$		$(0.9 < \cos\theta < 1.0)$	
	f_{nf}	f_{sf}	f_{nf}	f_{sf}
1.7	0.87	0.96	0.74	0.91
1.8	0.89	0.96	0.73	0.91
1.9	0.91	0.97	0.73	0.91
2.0	0.93	0.98	0.74	0.91
2.1	0.94	0.98	0.76	0.92
2.2	0.95	0.98	0.78	0.93
2.3	0.96	0.99	0.79	0.93
2.4	0.97	0.99	0.81	0.94

and spin-non-flip cross sections. For this reason the application of Table 4 in correcting the η and ω production angular distributions will be deferred until Sections V and VI, where the shapes of the production angular distributions indicate the relative importance of the spin-flip and spin-non-flip contributions.

The upward corrections obtained above are not expected to increase the η and ω cross sections obtained in Section IV, however. This is because in Section IV these resonance cross sections are obtained by normalizing to the sum of the known cross sections for the charge-symmetric counterparts to reactions (II.1) through (II.4). All of these reactions have two protons in the final state, however, and depending upon the particular form of the production angular distribution in each final state, all should be corrected upward to account for the Pauli principle. The forwardmost two production bins, which contain not more than 20 per cent of the events for any of reactions (II.1) through (II.4), will be corrected upward typically by about 15 per cent, so that there will be in general less than about a 3 per cent correction to the total number of events in any channel. This percentage probably does not vary much for the four final states used for normalization, so the cross section obtained for the resonant part of reaction (II.2) will not be significantly affected by the Pauli principle.

IV. THE FINAL STATE (p) p π^+ π^- π^o: GENERAL CHARACTERISTICS

In this section attention will be focused on resonance production in the final state (p) p π^+ π^- π^o, in which it is explicitly assumed that one of the final-state protons, designated as (p), is a spectator to the reaction

$$\pi^+ n \rightarrow p \pi^+ \pi^- \pi^o \qquad \text{(IV.1)}$$

In order to help assure that this is the case, only those "good" examples of final state (II.2) which have at least one proton with laboratory momentum less than 300 MeV/c will be used in the discussion of this section and the two following sections on η and ω production. Spectator protons with momentum less than 300 MeV/c do indeed conform well to the predictions of the impulse model, as was seen in the previous section, particularly from Figures 7 and 11b. There are 8710 events satisfying the above criteria.

A. Mass Spectra

Figure 15 shows the most important features of reaction (IV.1). Figure 15a is a scatter plot of c.m. energy vs. the 3-pion mass; a prominent η band at mass 549 MeV/c^2 and a very strong ω band at about 785 MeV/c^2 characterize the data. The resonant signals show up as large peaks in the 3-pion mass spectrum of Figure 15b, the lower histogram of which shows the spectrum for events in which -t (from the beam to the 3 pions) is less than 0.6 BeV^2.

Figures 16-24 display other mass spectra in the same way as the 3-pion mass spectrum is presented. The a-part of each figure is a

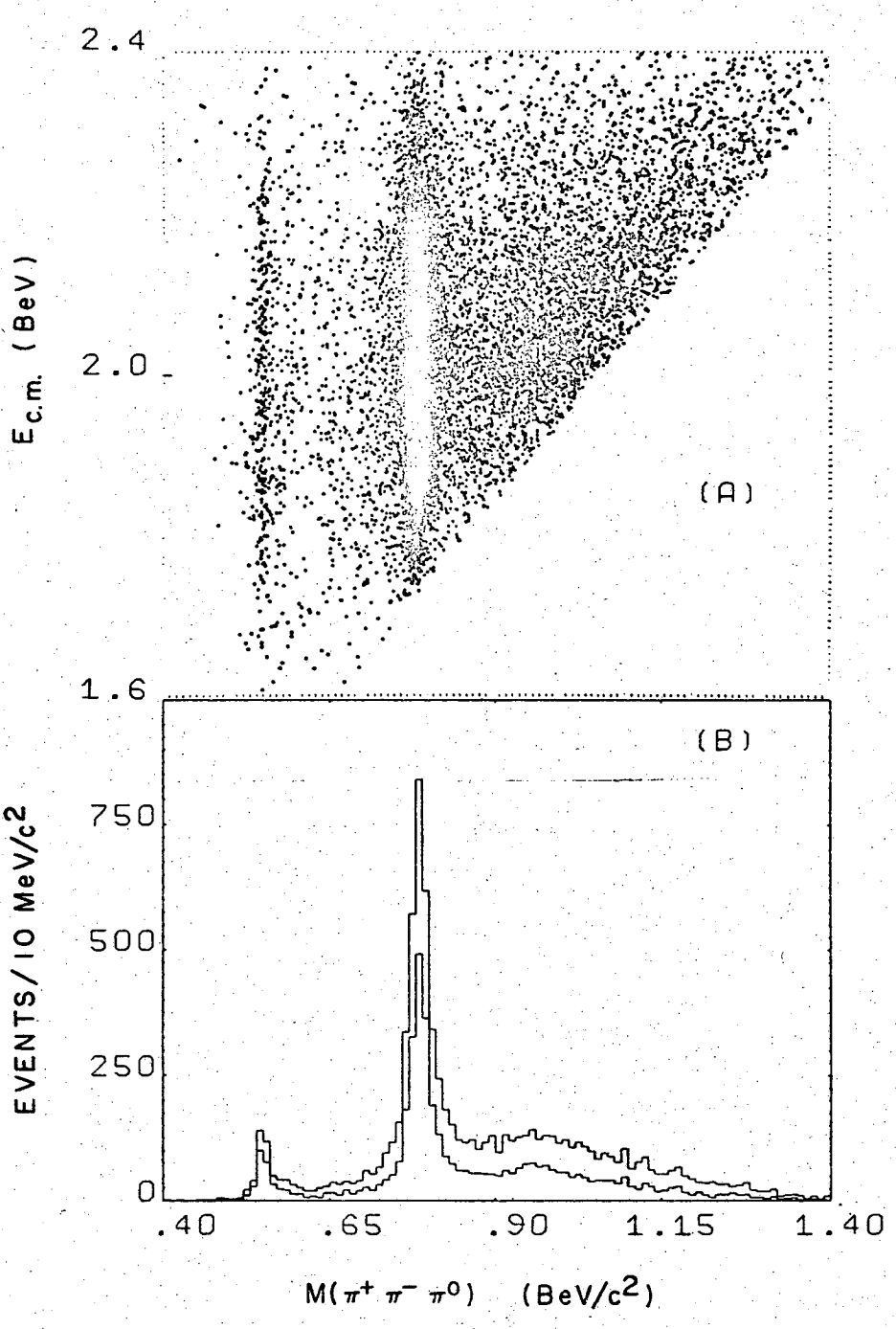

XBL 696-740

Figure 15. a) $m(\pi^+\pi^-\pi^0)$ vs. c.m. energy; b) $m(\pi^+\pi^-\pi^0)$, the lower histogram has events with $-t(\text{beam to } \pi^+\pi^-\pi^0) < 0.6$ BeV^2.

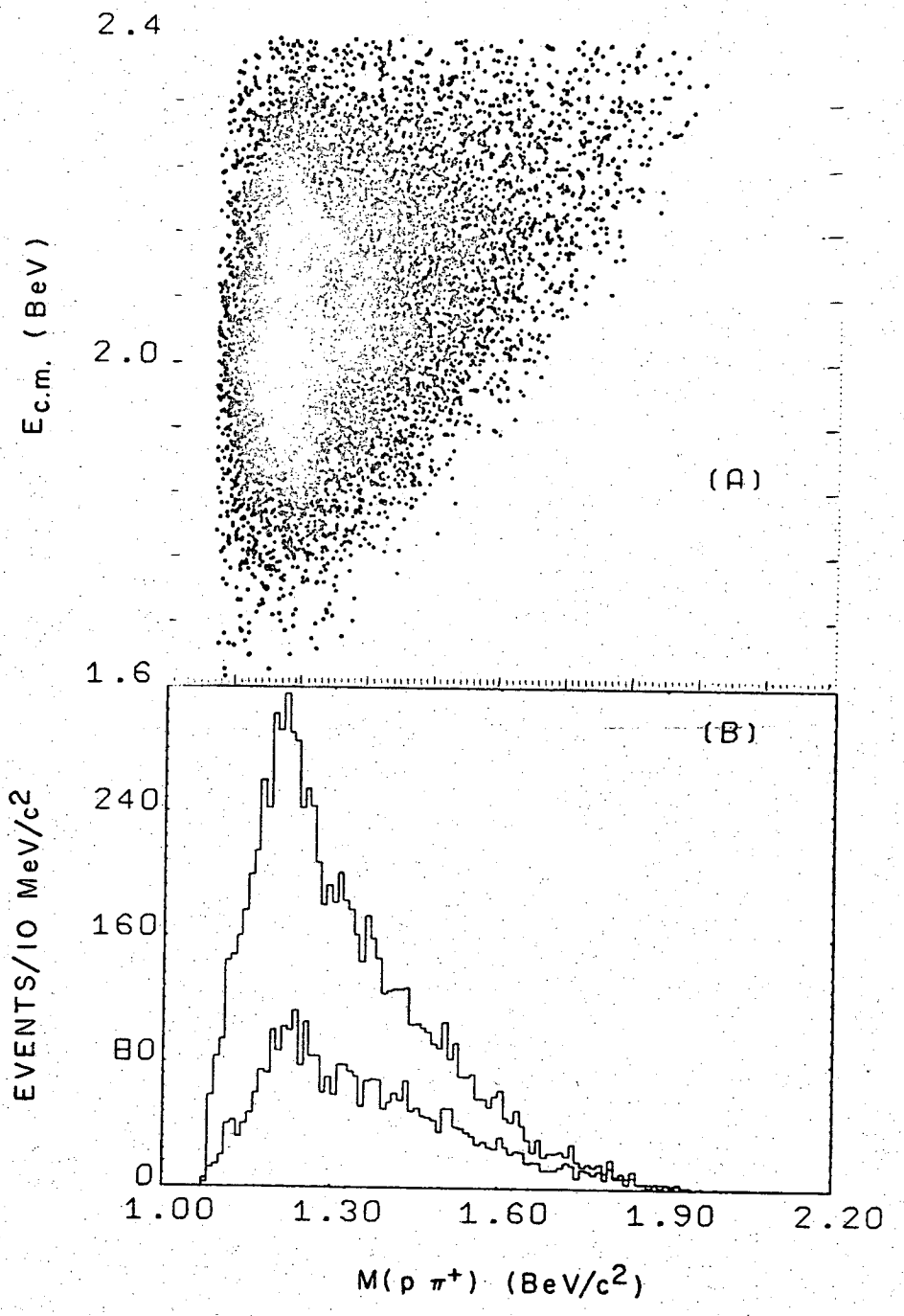

XBL 696-745

Figure 16. a) m($p\pi^+$) vs. c.m. energy; b) m($p\pi^+$), the lower histogram has events with u(beam to $p\pi^+$) < 0.4 Bev^2.

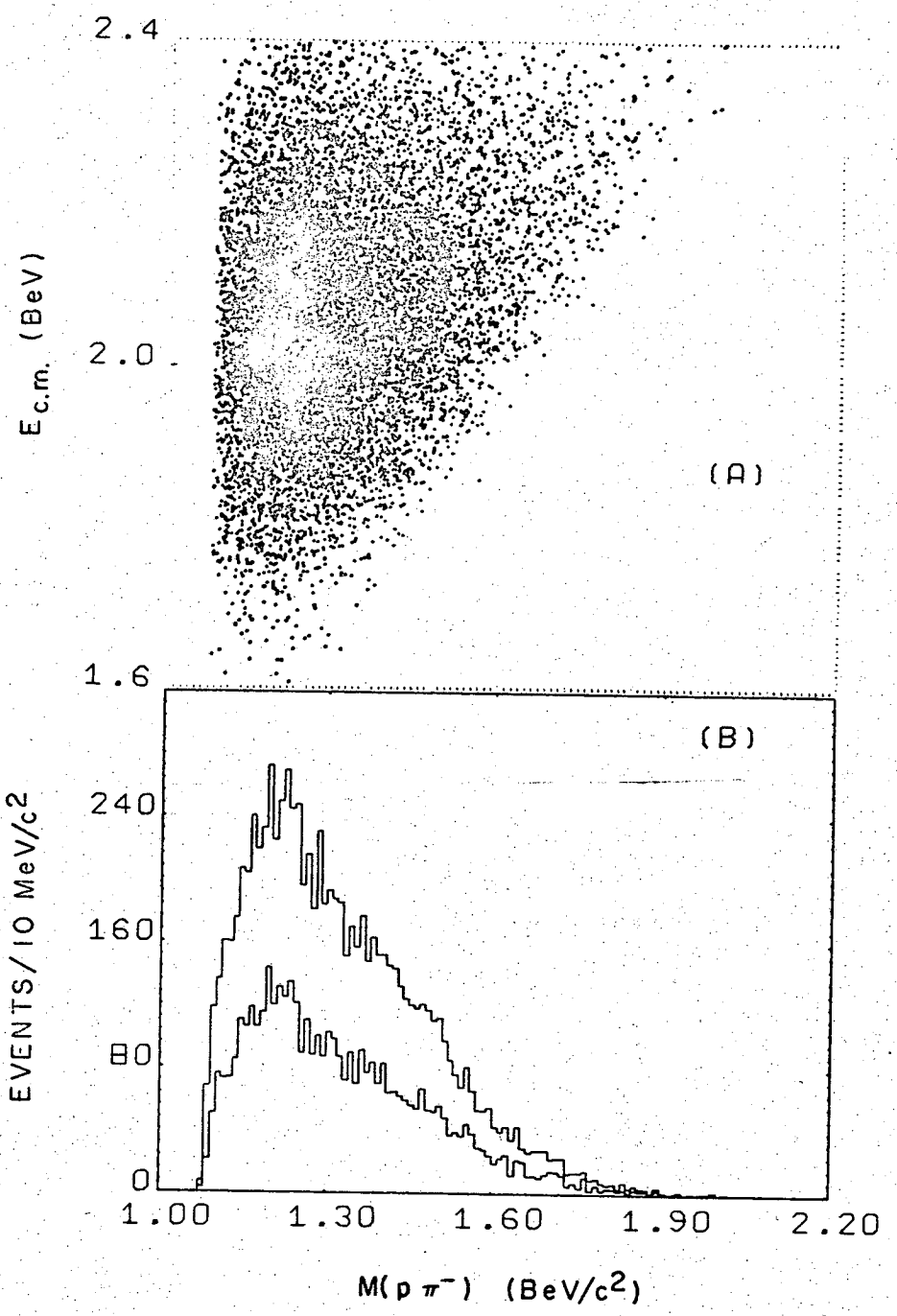

XBL 696-742

Figure 17. a) m(pπ^-) vs. c.m. energy; b) m(pπ^-), the lower histogram has events with -t(target to pπ^-) < 0.6 BeV^2.

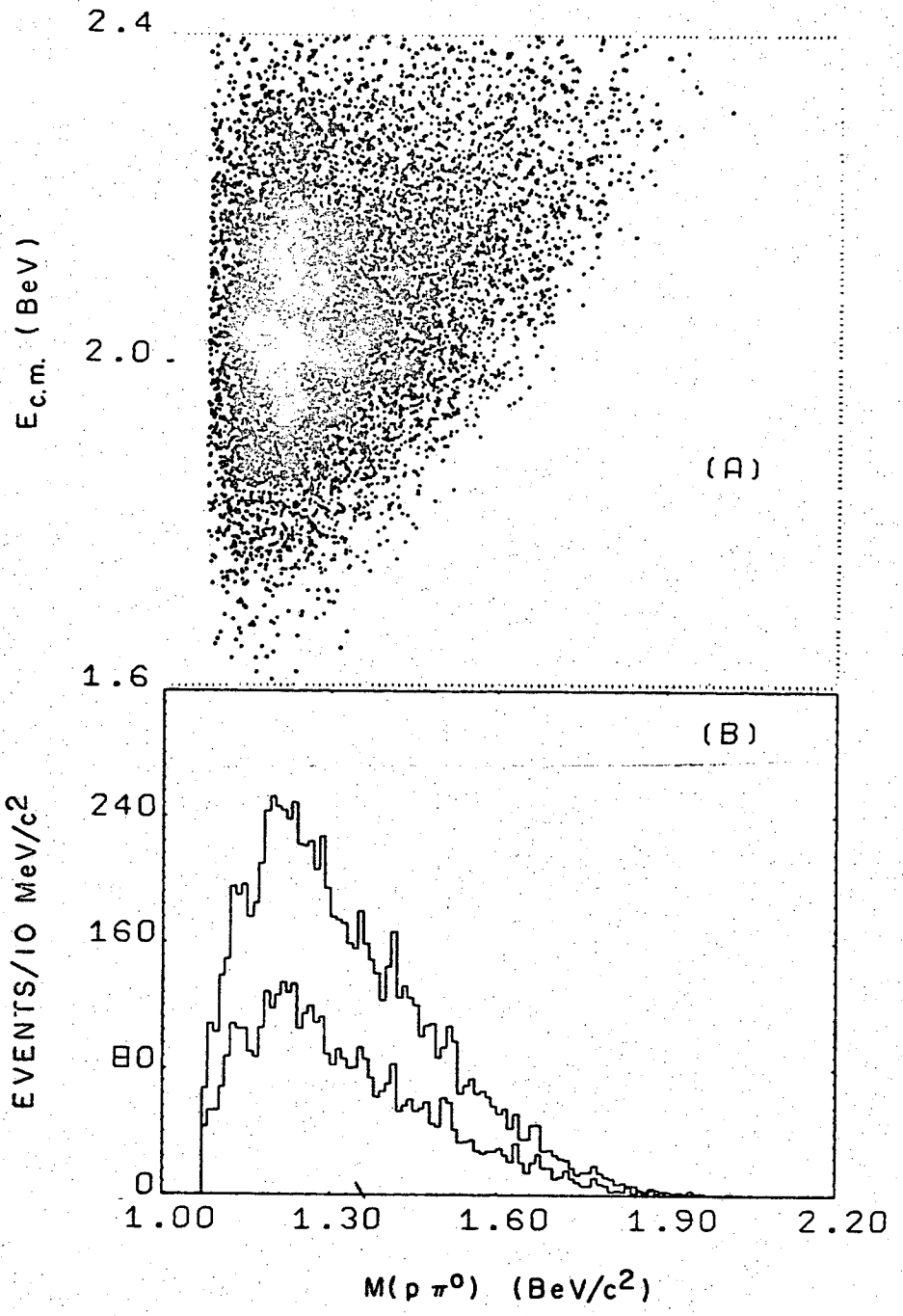

Figure 18. a) $m(p\pi^o)$ vs. c.m. energy; b) $m(p\pi^o)$, the lower histogram has events with $-t$(target to $p\pi^o$) < 0.6 BeV^2.

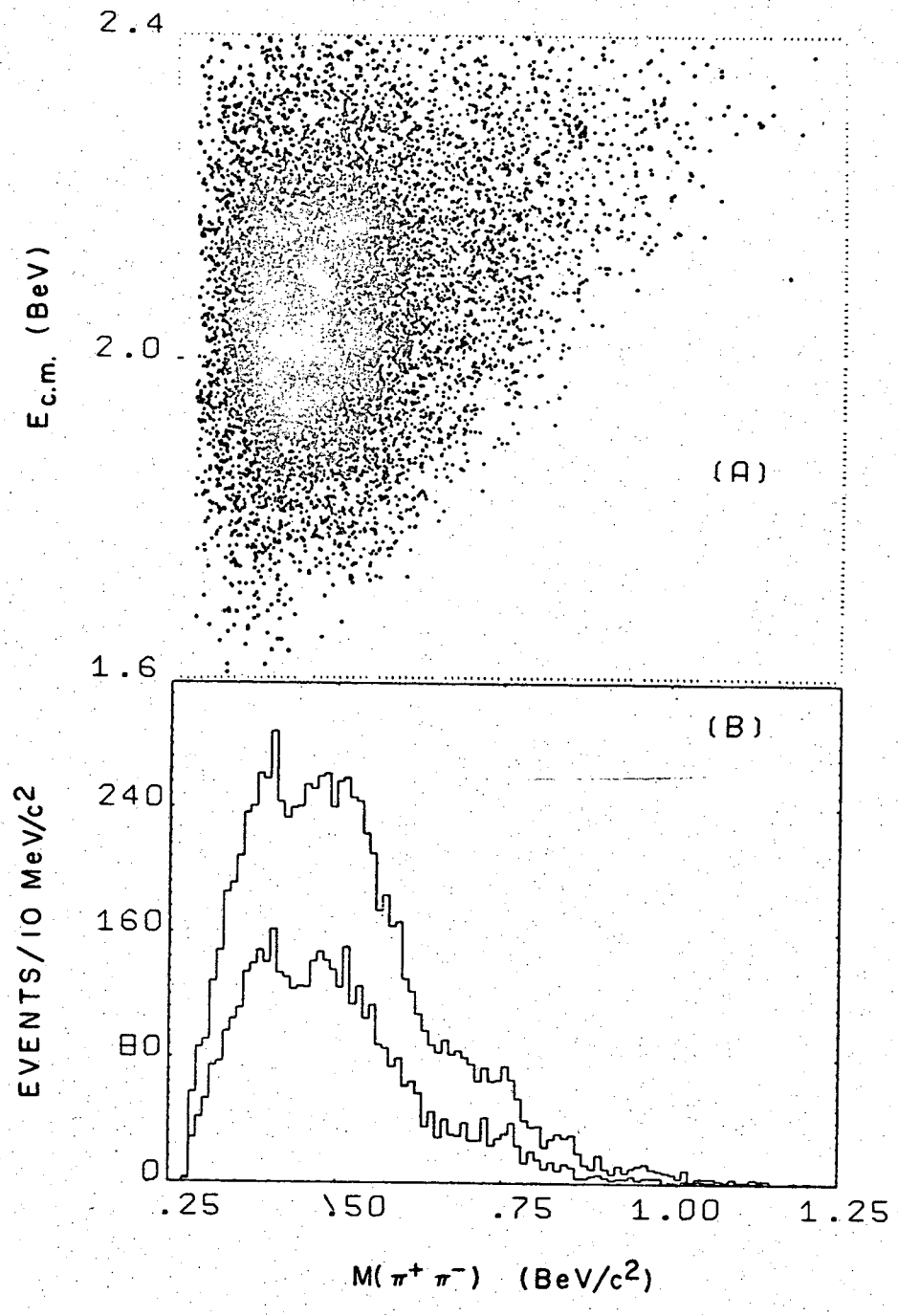

XBL 696-753

Figure 19. a) $m(\pi^+\pi^-)$ vs. c.m. energy; b) $m(\pi^+\pi^-)$, the lower histogram has events with $-t(\text{beam to } \pi^+\pi^-) < 0.6$ BeV^2.

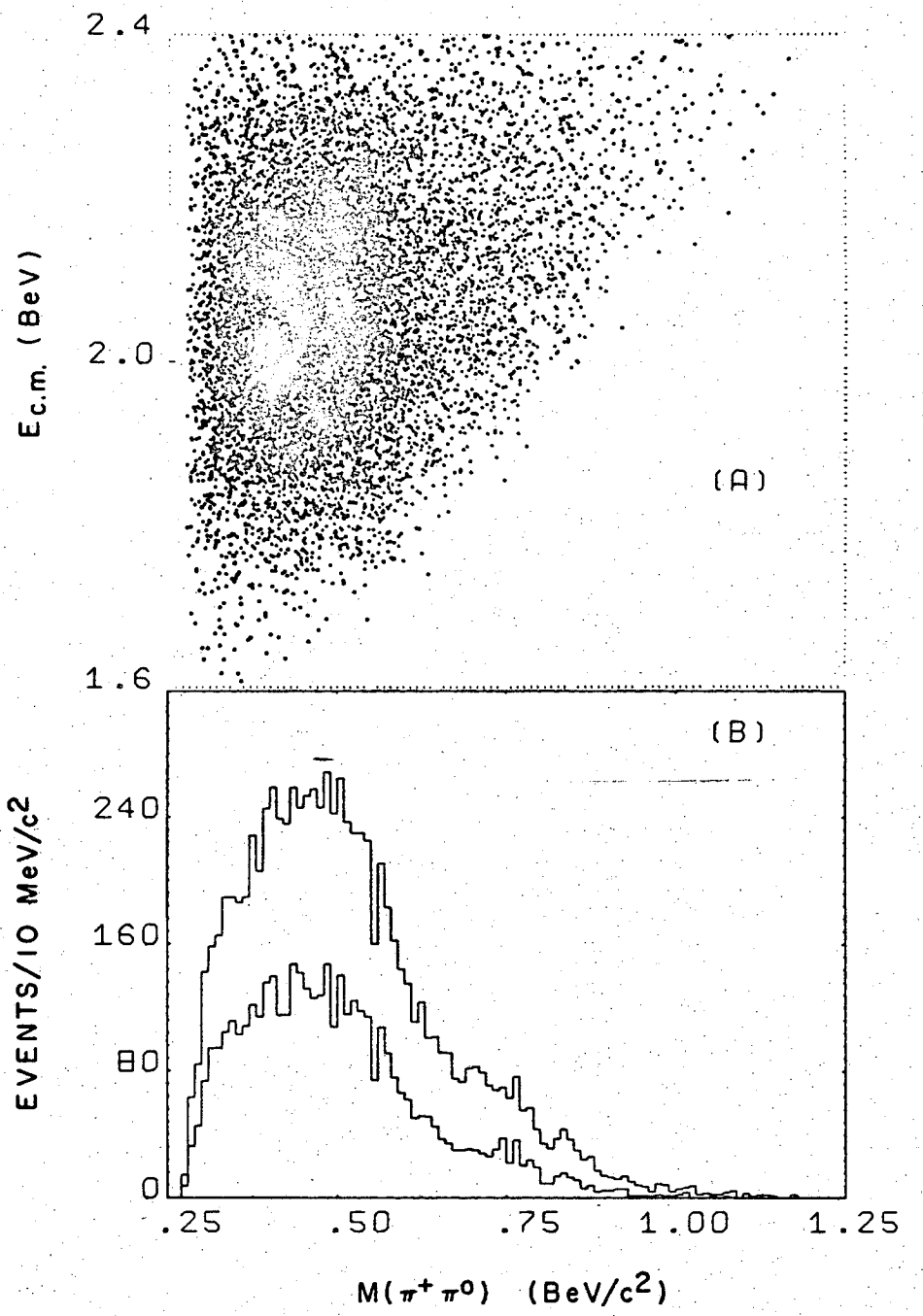

Figure 20. a) $m(\pi^+\pi^0)$ vs. c.m. energy; b) $m(\pi^+\pi^0)$, the lower histogram has events with $-t(\text{beam to } \pi^+\pi^0) < 0.6$ BeV^2.

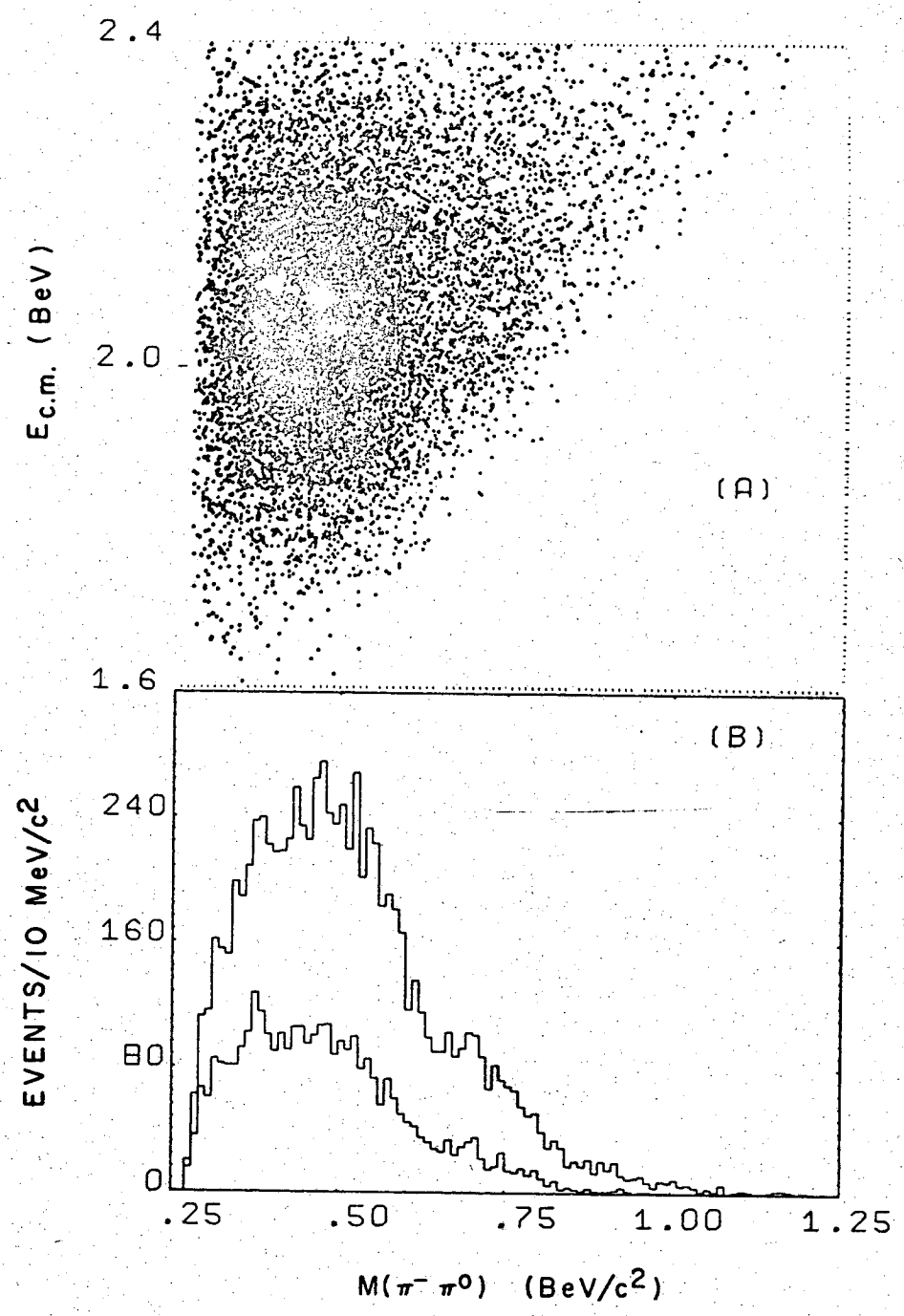

XBL 696-744

Figure 21. a) $m(\pi^- \pi^0)$ vs. c.m. energy; b) $m(\pi^- \pi^0)$, the lower histogram has events with $u(\text{target to } \pi^- \pi^0) < 0.4$ BeV^2.

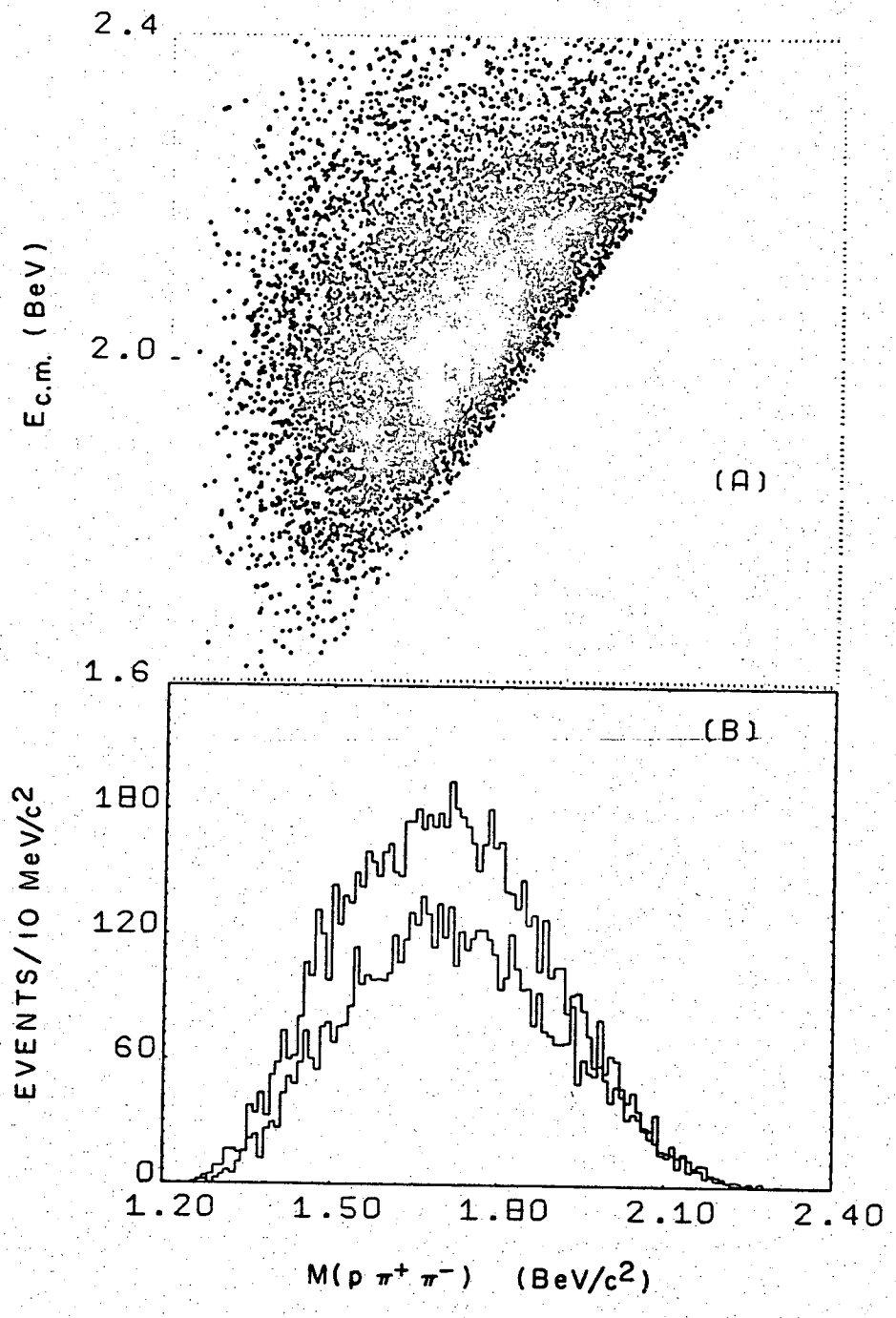

Figure 22. a) $m(p\pi^+\pi^-)$ vs. c.m. energy; b) $m(p\pi^+\pi^-)$, the lower histogram has events with $-t$(target to $p\pi^+\pi^-$) < 0.6 BeV^2.

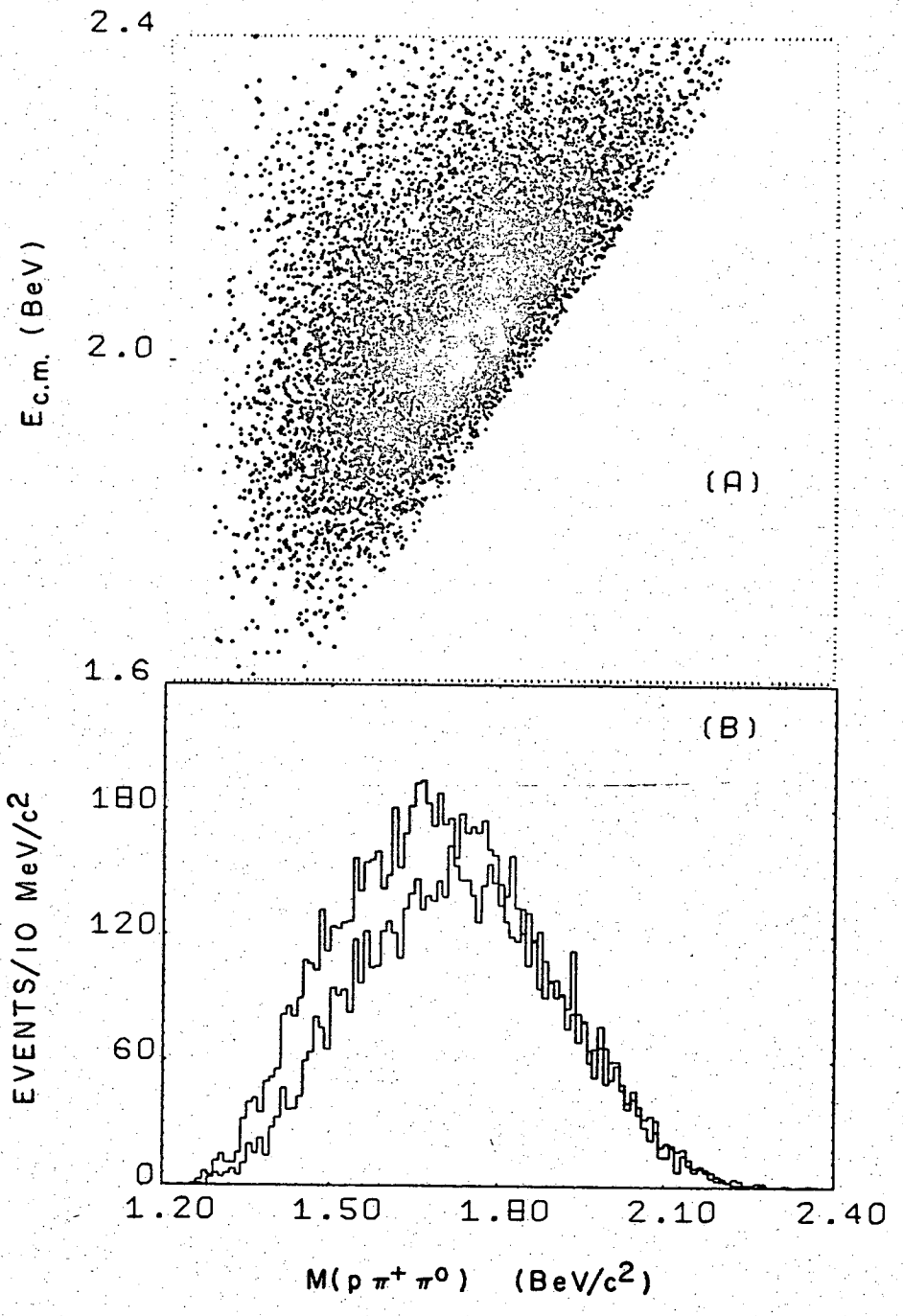

Figure 23. a) $m(p\pi^+\pi^0)$ vs. c.m. energy; b) $m(p\pi^+\pi^0)$, the lower histogram has events with u(beam to $p\pi^+\pi^0$) < 0.4 BeV^2.

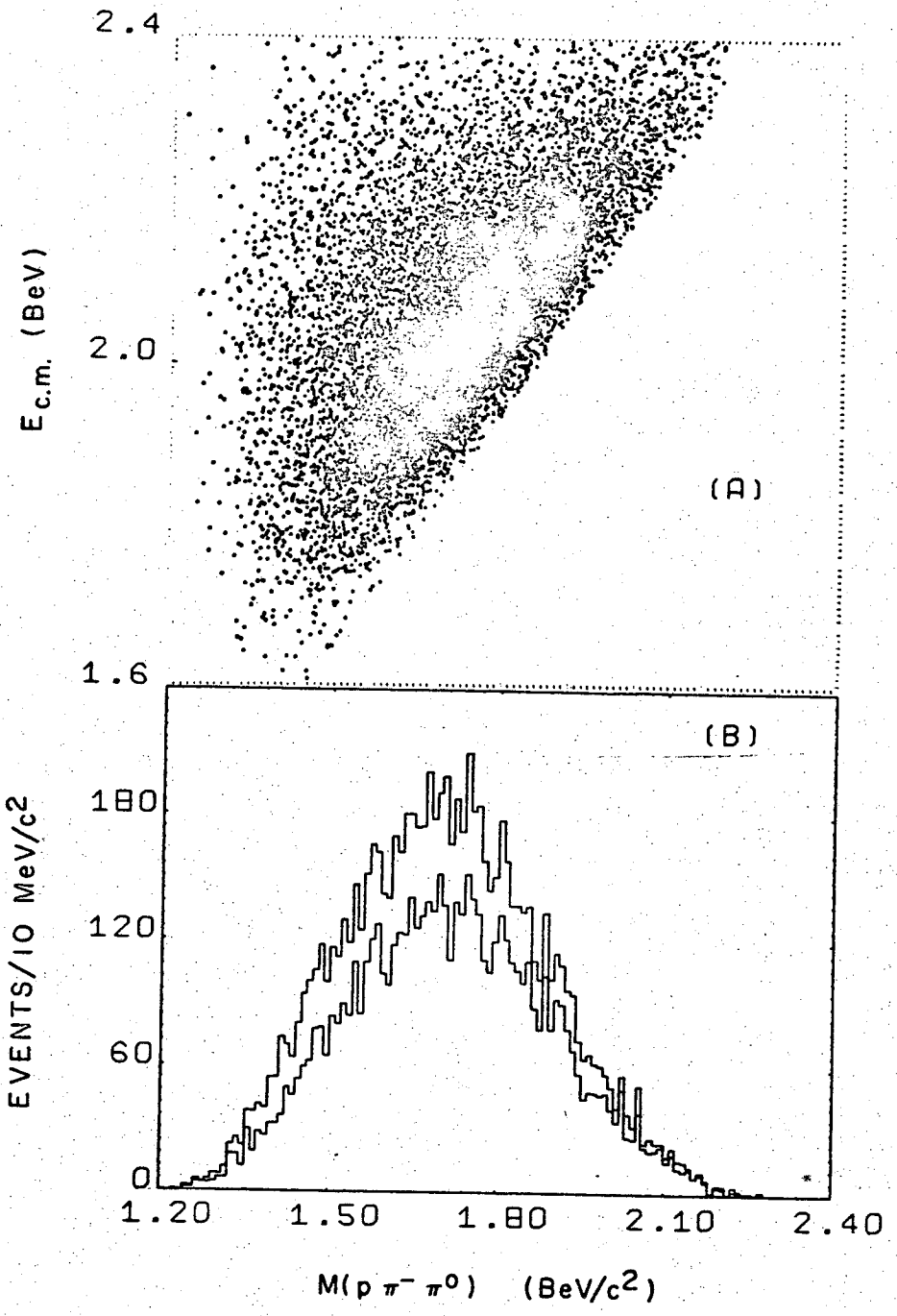

Figure 24. a) $m(p\pi^-\pi^0)$ vs. c.m. energy; b) $m(p\pi^-\pi^0)$, the lower histogram has events with $-t$(target to $p\pi^-\pi^0$) < 0.6 BeV^2.

scatter plot of c.m. energy vs. mass, and the b-part of the figure is the mass distribution for all c.m. energies (the projection onto the x-axis of the scatter plot). The lower histogram in the b-part of each figure is the mass spectrum for events for which the beam-to-pion(s) momentum-transfer-squared (-t) is less than 0.6 BeV^2; exceptions are the lower histograms for the $p\pi^+$, $\pi^-\pi^o$, and $p\pi^+\pi^o$ mass spectra, for which the events are restricted to have the neutron-to-pion(s) momentum-transfer-squared (u) less than 0.4 BeV^2. This is done because a t-cut enhances processes which proceed by exchange of a meson, whereas any resonance in the spectra of the $p\pi^+$, $\pi^-\pi^o$, or $p\pi^+\pi^o$ would have to be mediated by the exchange of a doubly-charged meson, of which there are no known examples. However, baryon exchange via a singly-charged baryon is a possible mechanism for the three mass spectra mentioned, so a u-cut is applied for these spectra. Figures 16-24 show the mass spectra for the mass combinations $p\pi^+$, $p\pi^-$, $p\pi^o$, $\pi^+\pi^-$, $\pi^+\pi^o$, $\pi^-\pi^o$, $p\pi^+\pi^-$, $p\pi^+\pi^o$, and $p\pi^-\pi^o$, respectively. These figures show none of the prominent structure observed in the 3-pion spectrum; in fact the only structure immediately visible in either the uncut or cut histograms is a small amount of $\Delta^{++}(1236)$ in the $p\pi^+$ mass spectrum and a suggestion of a slight amount of ρ production in the 2-pion mass combinations. It will be seen below that all the mass spectra are well described by a fit which includes η and ω production in the 3-pion mass spectrum as the only resonances present.

B. Details of the $\pi^+\pi^-\pi^o$ Mass Spectrum

The 3-pion mass spectrum will now be investigated more closely.

In order to find the amounts of η and ω, as well as to fit their masses and widths as a function of c.m. energy, the data were divided into six c.m. energy intervals, each of which is 100 MeV wide, centered at the values $E_{c.m.}$ = 1.8, 1.9, 2.0, 2.1, 2.2, and 2.3 BeV. For each interval a separate maximum-likelihood fit to the data was performed using the program MURTLEBERT.[37] The amount, mass, and width of the two resonances were determined by the fit; the values obtained are given in Table 5. Because the η and ω widths are larger than the true widths of these resonances,[26] the line shape used in the fits was Gaussian, and the widths in Table 5 are full width at half maximum. Inclusion of $\Delta^{++}(1236)$ in the maximum-likelihood fitting procedure was found to identify only a few per cent of this resonance, with large errors on its amount and width; in addition, the η and ω parameters were the same whether or not $\Delta^{++}(1236)$ was included in the fit, so for simplicity this resonance is ignored in Table 5.

Each of Figures 25-34 shows a mass spectrum from reaction (IV.1) at the six c.m. energy intervals; the curves are the Monte-Carlo predictions of the maximum-likelihood fits summarized in Table 5. With the exception of the $p\pi^+$ spectrum, all the mass distributions are well described by a fit involving only η and ω signals in the 3-pion mass spectrum.

The momentum-transfer-squared between the beam and the 3 pions in reaction (IV.1) is plotted vs. 3-pion mass in Figure 35. This figure differs from a Chew-Low plot in that it is the mass, and not the mass-squared of the 3 pions that is plotted against the momentum-transfer-squared, and, more importantly, in that all c.m. energies

Table 5. Number of events, and amount, mass, and width of η and ω in each of six 100 MeV-wide c.m. energy intervals.

$E_{c.m.}$ (BeV)	number of events	η fraction	m_η (MeV)	Γ_η (MeV)	ω fraction	m_ω (MeV)	Γ_ω (MeV)
1.8	509	.083 ± .023	548 ± 3	24 ±19	.503 ± .058	784 ± 1	31 ±10
1.9	1 278	.059 ± .008	547 ± 3	39 ± 7	.432 ± .019	786 ± 1	38 ± 3
2.0	1 972	.033 ± .004	549 ± 1	19 ± 3	.314 ± .015	784 ± 1	37 ± 3
2.1	1 976	.037 ± .005	549 ± 1	25 ± 3	.287 ± .013	786 ± 1	39 ± 3
2.2	1 611	.024 ± .004	549 ± 1	11 ± 2	.274 ± .014	785 ± 1	47 ± 3
2.3	954	.012 ± .004	550 ± 2	14 ± 3	.202 ± .015	785 ± 2	39 ± 4

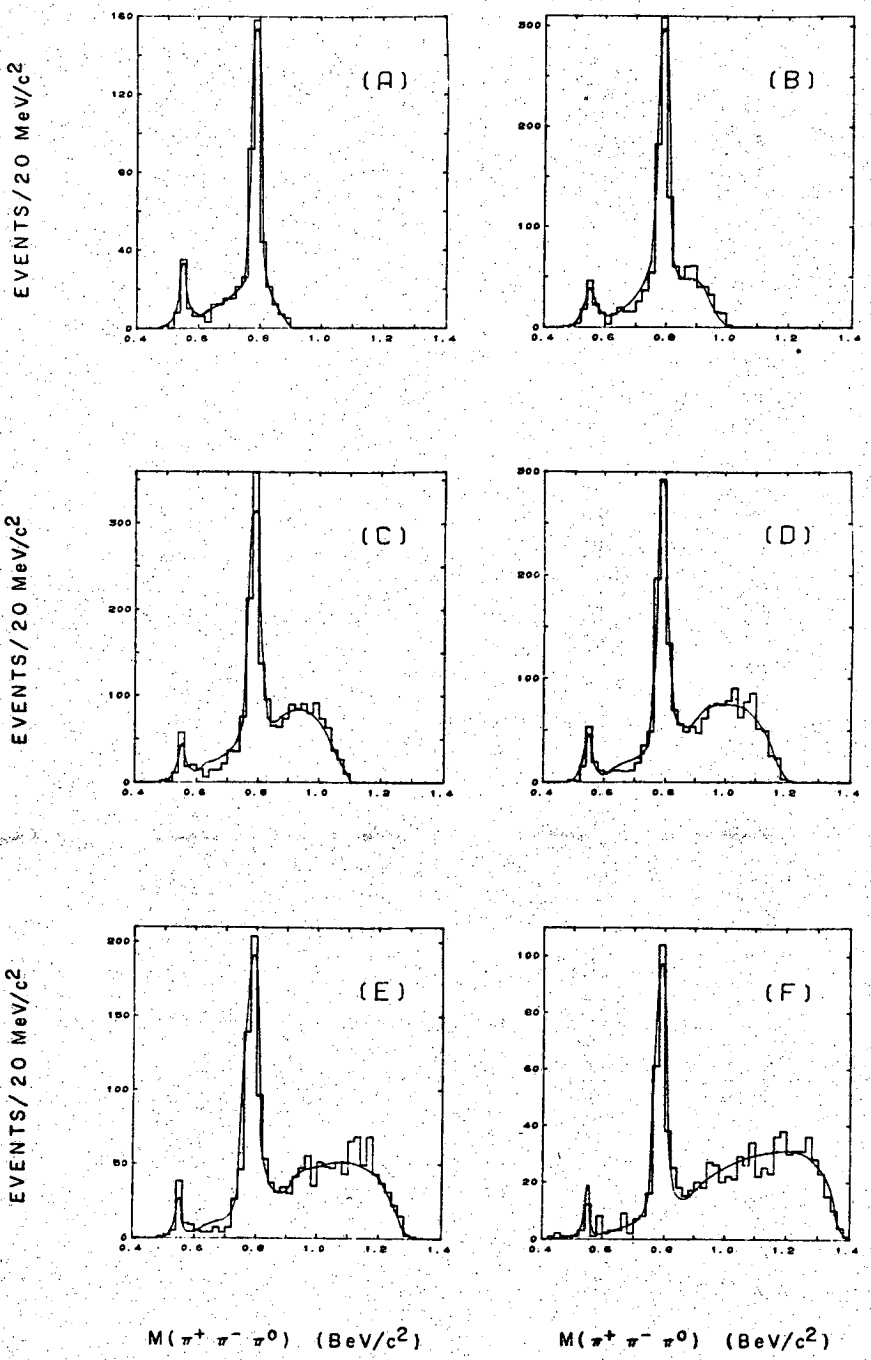

XBL 696-736

Figure 25. $m(\pi^+\pi^-\pi^0)$ in six 100 MeV-wide c.m. energy intervals centered at a) 1.8, b) 1.9, c) 2.0, d) 2.1, e) 2.2, and f) 2.3 BeV; the curves are from maximum-likelihood fits.

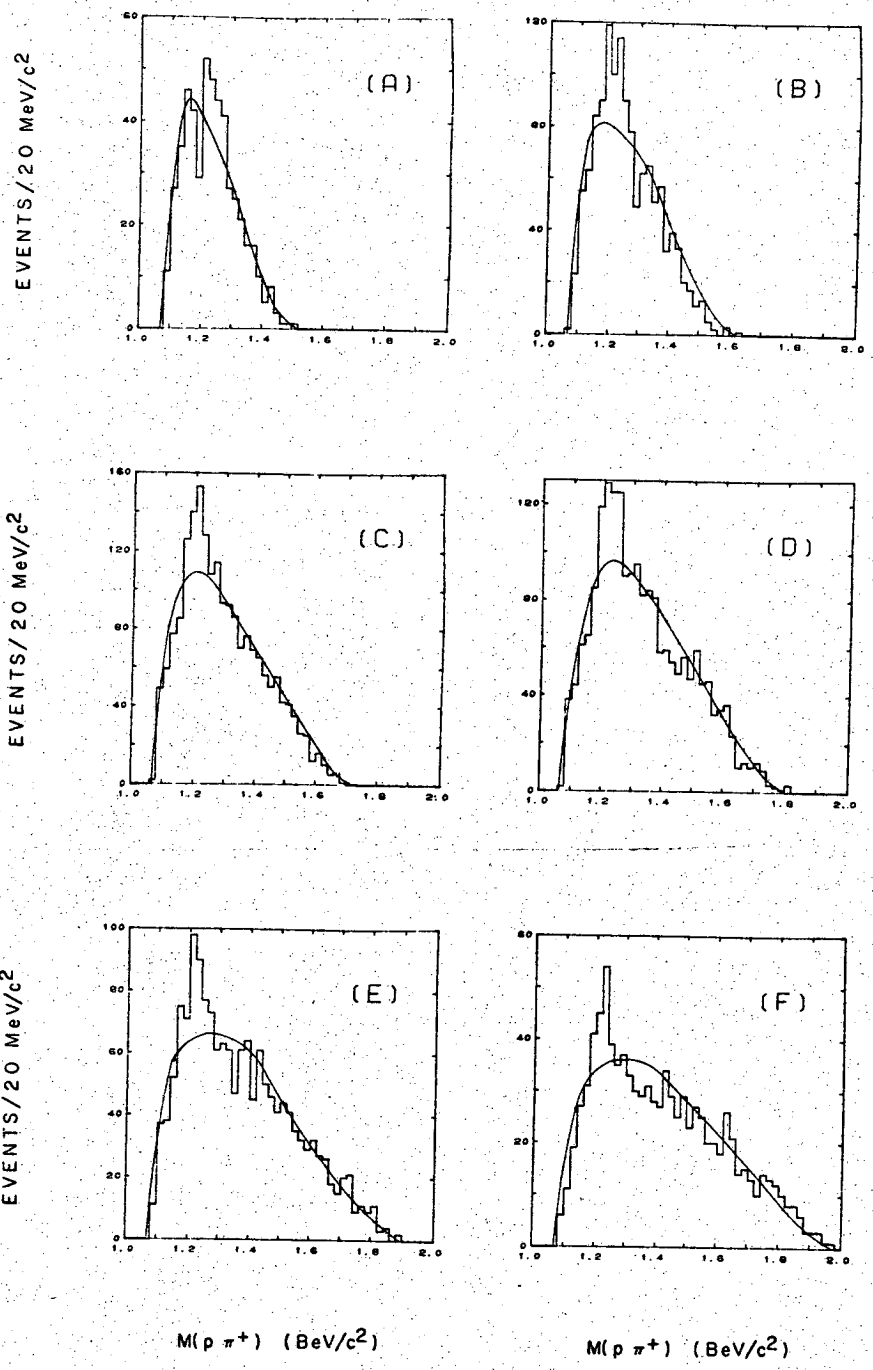

XBL 696-752

Figure 26. $m(p\pi^+)$ in six 100 MeV-wide c.m. energy intervals centered at a) 1.8, b) 1.9, c) 2.0, d) 2.1, e) 2.2, and f) 2.3 BeV; the curves are from maximum-likelihood fits.

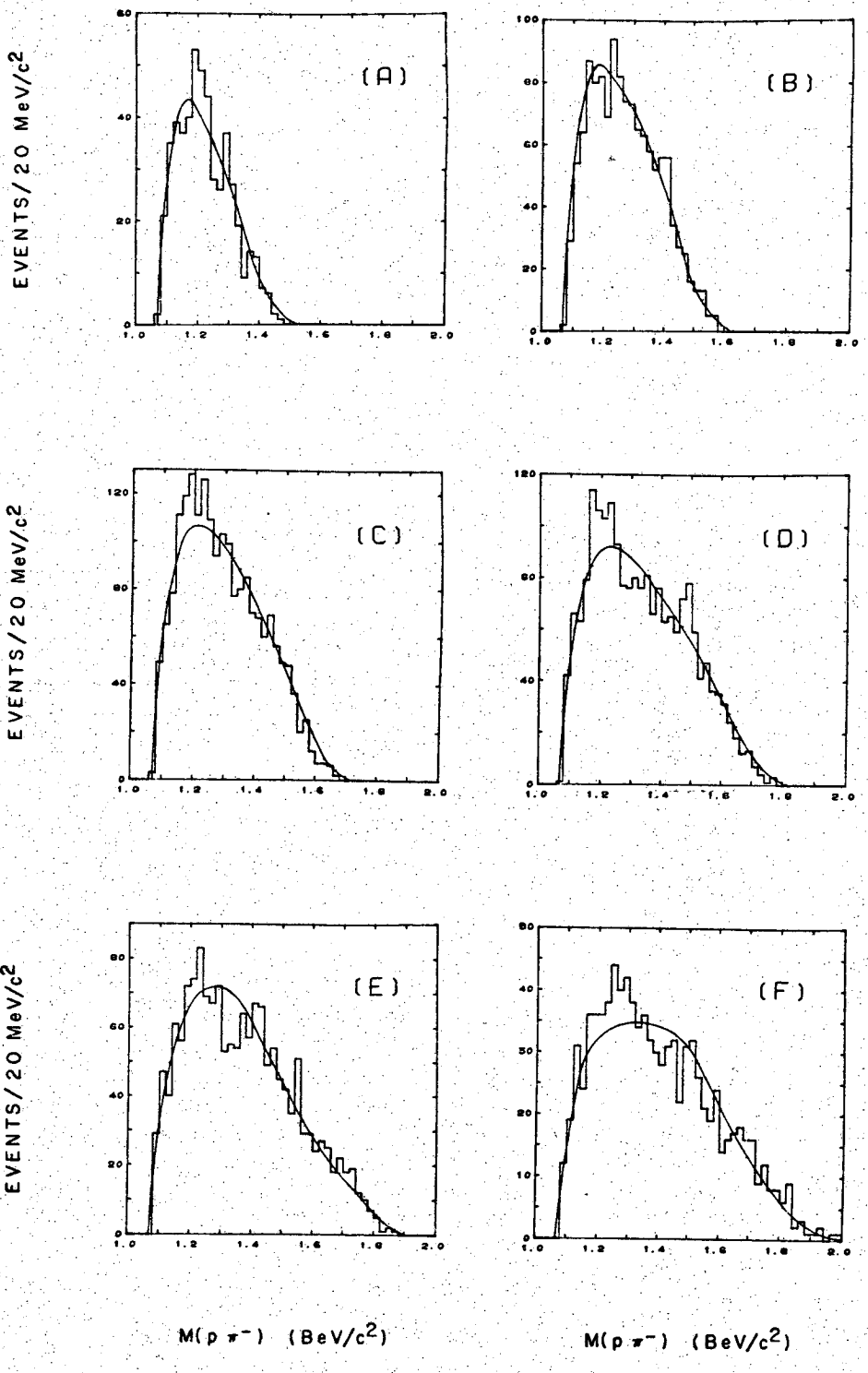

XBL 696-766

Figure 27. $m(p\pi^-)$ in six 100 MeV-wide c.m. energy intervals centered at a) 1.8, b) 1.9, c) 2.0, d) 2.1, e) 2.2, and f) 2.3 BeV; the curves are from maximum-likelihood fits.

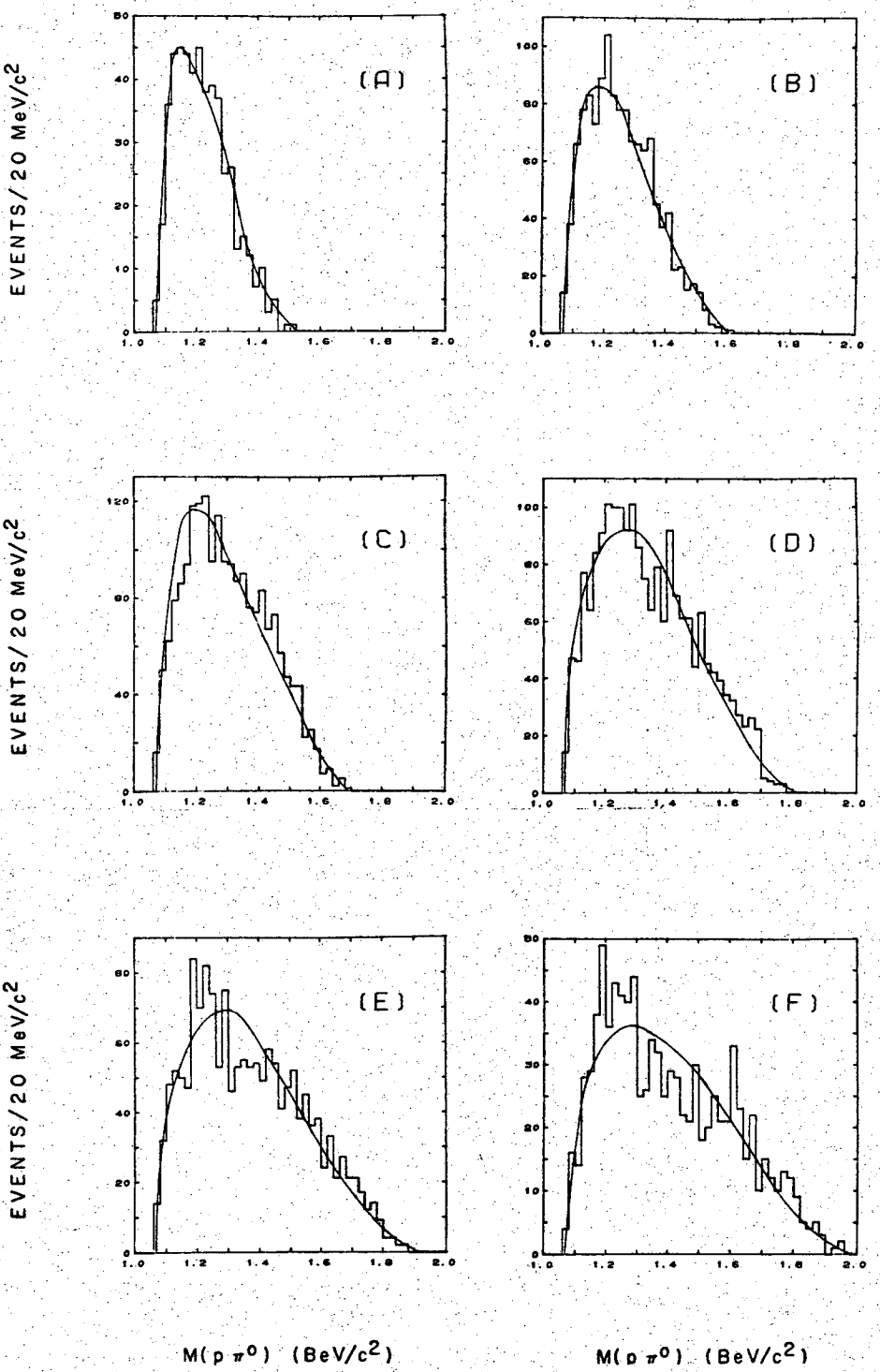

XBL 696-765

Figure 28. $m(p\pi^0)$ in six 100 MeV-wide c.m. energy intervals centered at a) 1.8, b) 1.9, c) 2.0, d) 2.1, e) 2.2, and f) 2.3 BeV; the curves are from maximum-likelihood fits.

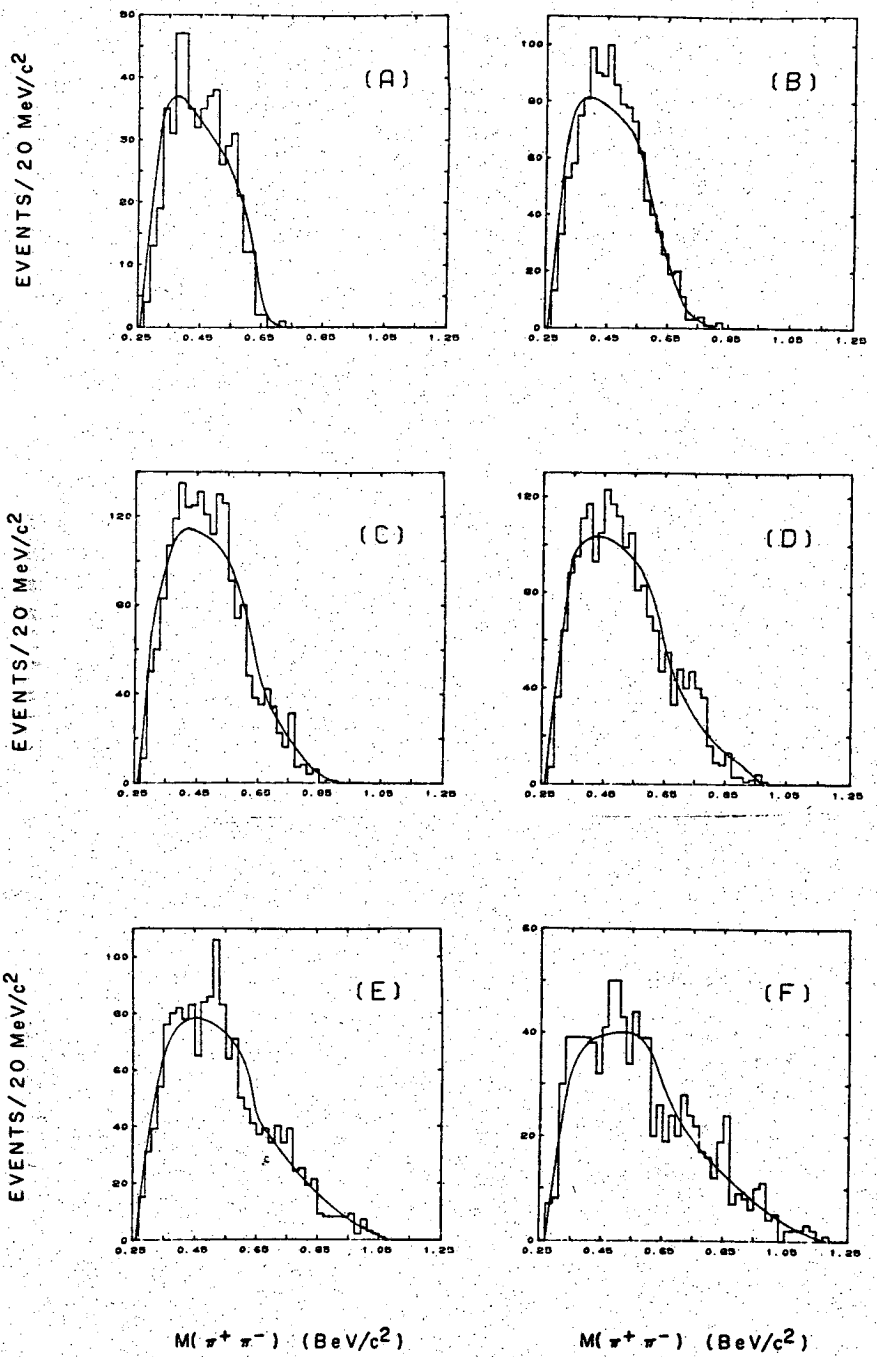

XBL 696-751

Figure 29. $m(\pi^+\pi^-)$ in six 100 MeV-wide c.m. energy intervals centered at a) 1.8, b) 1.9, c) 2.0, d) 2.1, e) 2.2, and f) 2.3 BeV; the curves are from maximum-likelihood fits.

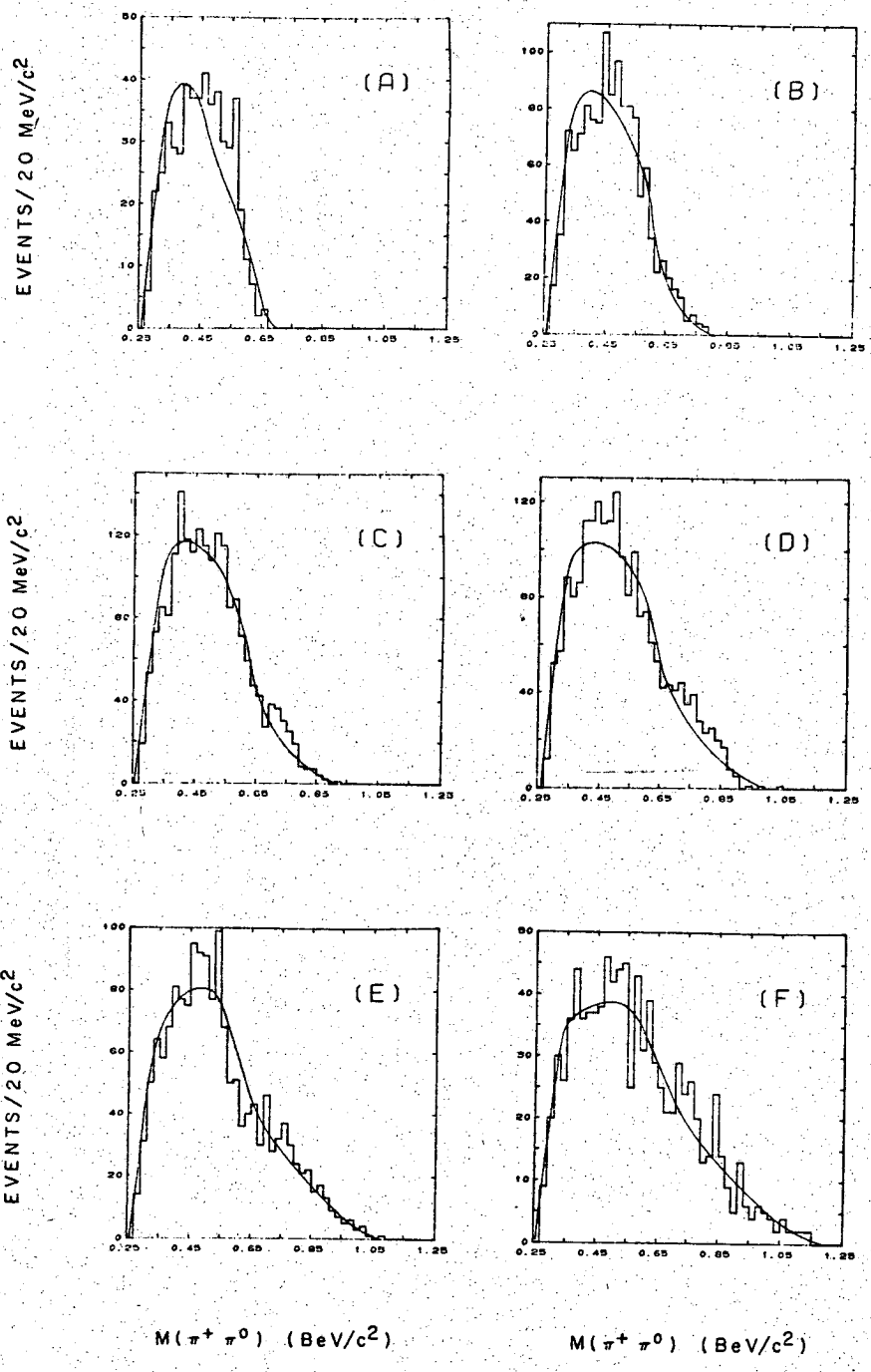

XBL 696-750

Figure 50. $m(\pi^+\pi^0)$ in six 100 MeV-wide c.m. energy intervals centered at a) 1.8, b) 1.9, c) 2.0, d) 2.1, e) 2.2, and f) 2.3 BeV; the curves are from maximum-likelihood fits.

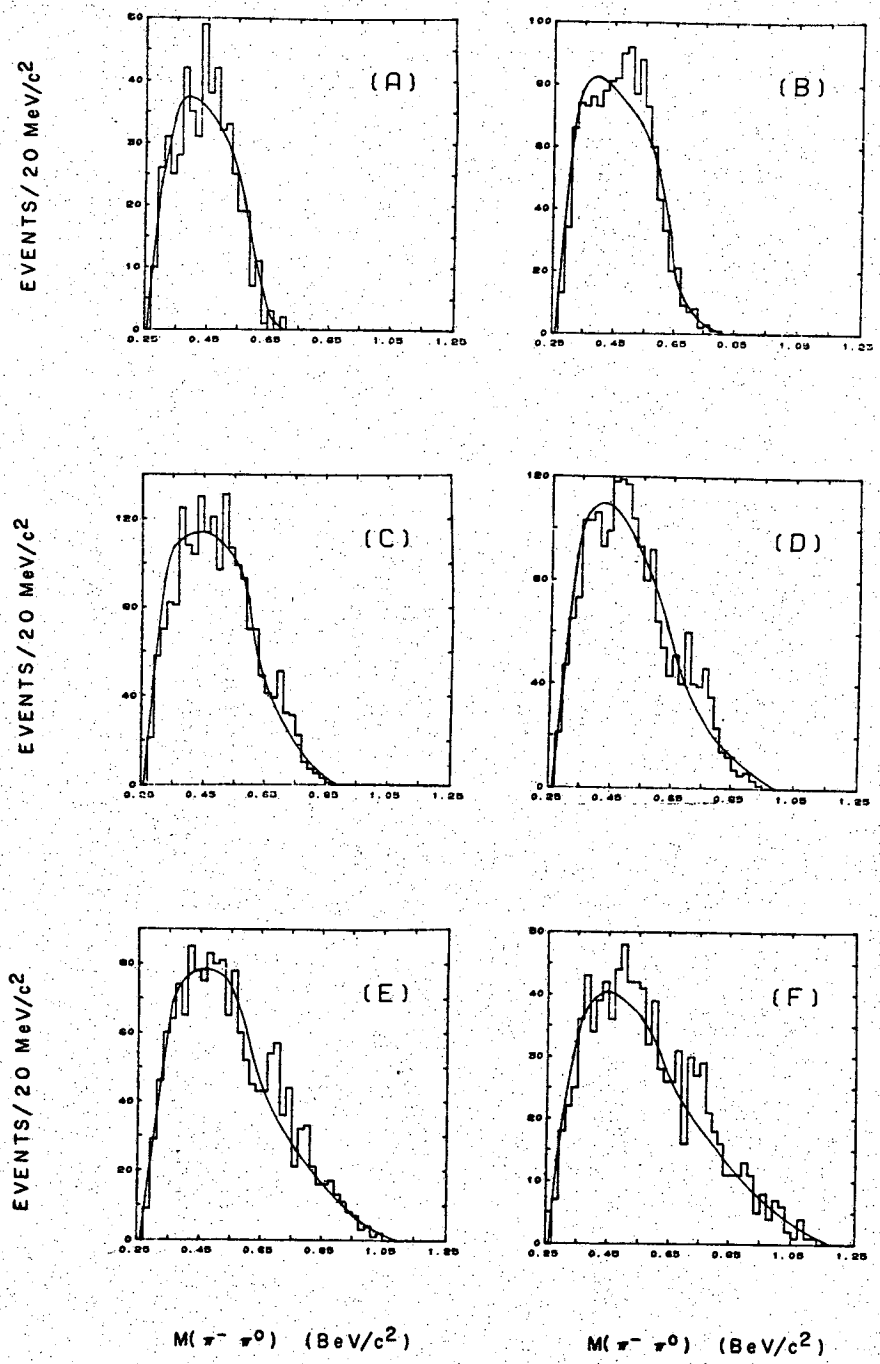

XBL 696-749

Figure 31. $m(\pi^-\pi^0)$ in six 100 MeV-wide c.m. energy intervals centered at a) 1.8, b) 1.9, c) 2.0, d) 2.1, e) 2.2, and f) 2.3 BeV; the curves are from maximum-likelihood fits.

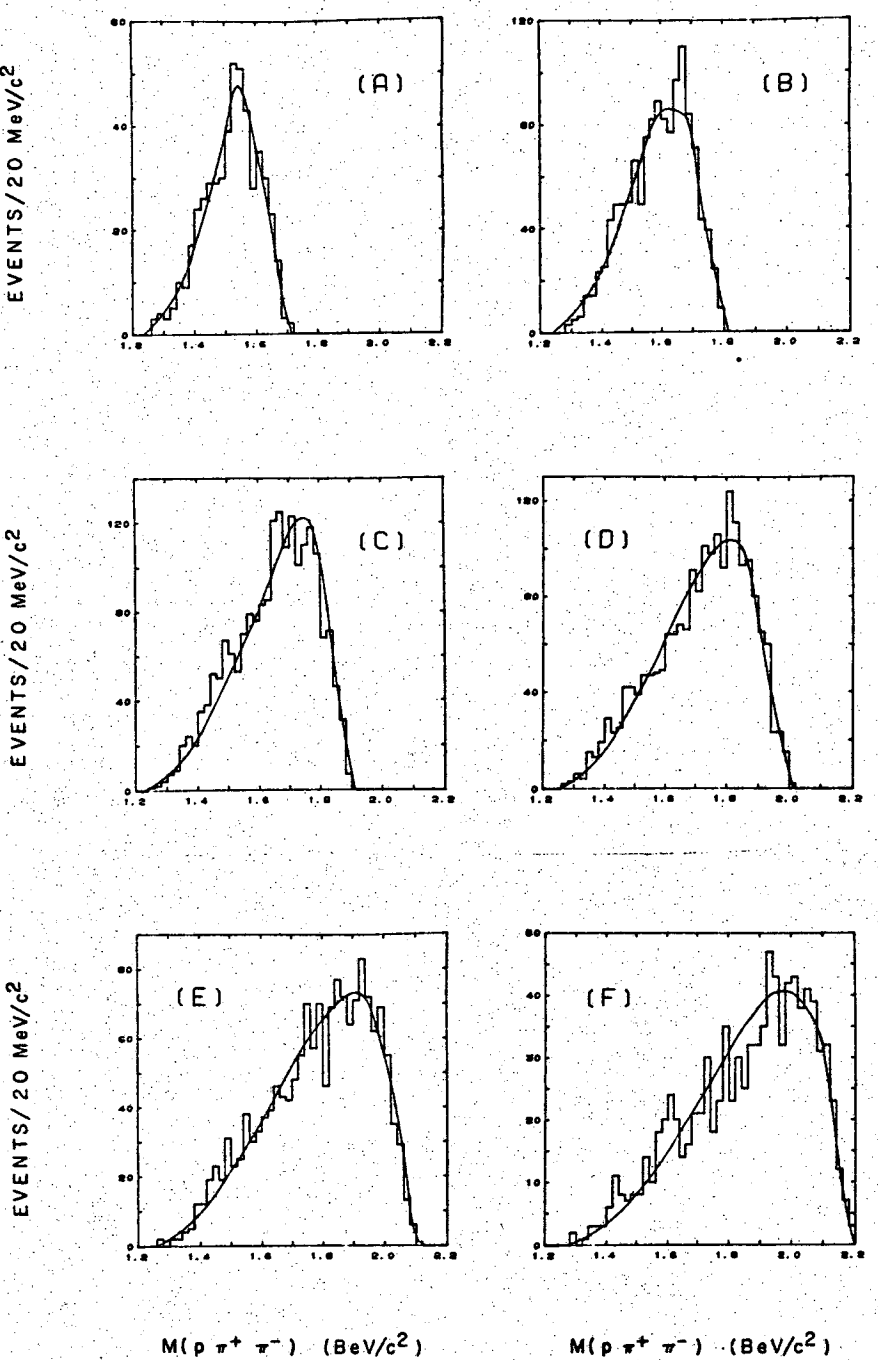

XBL 696-747

Figure 32. $m(p\pi^+\pi^-)$ in six 100 MeV-wide c.m. energy intervals centered at a) 1.8, b) 1.9, c) 2.0, d) 2.1, e) 2.2, and f) 2.3 BeV; the curves are from maximum-likelihood fits.

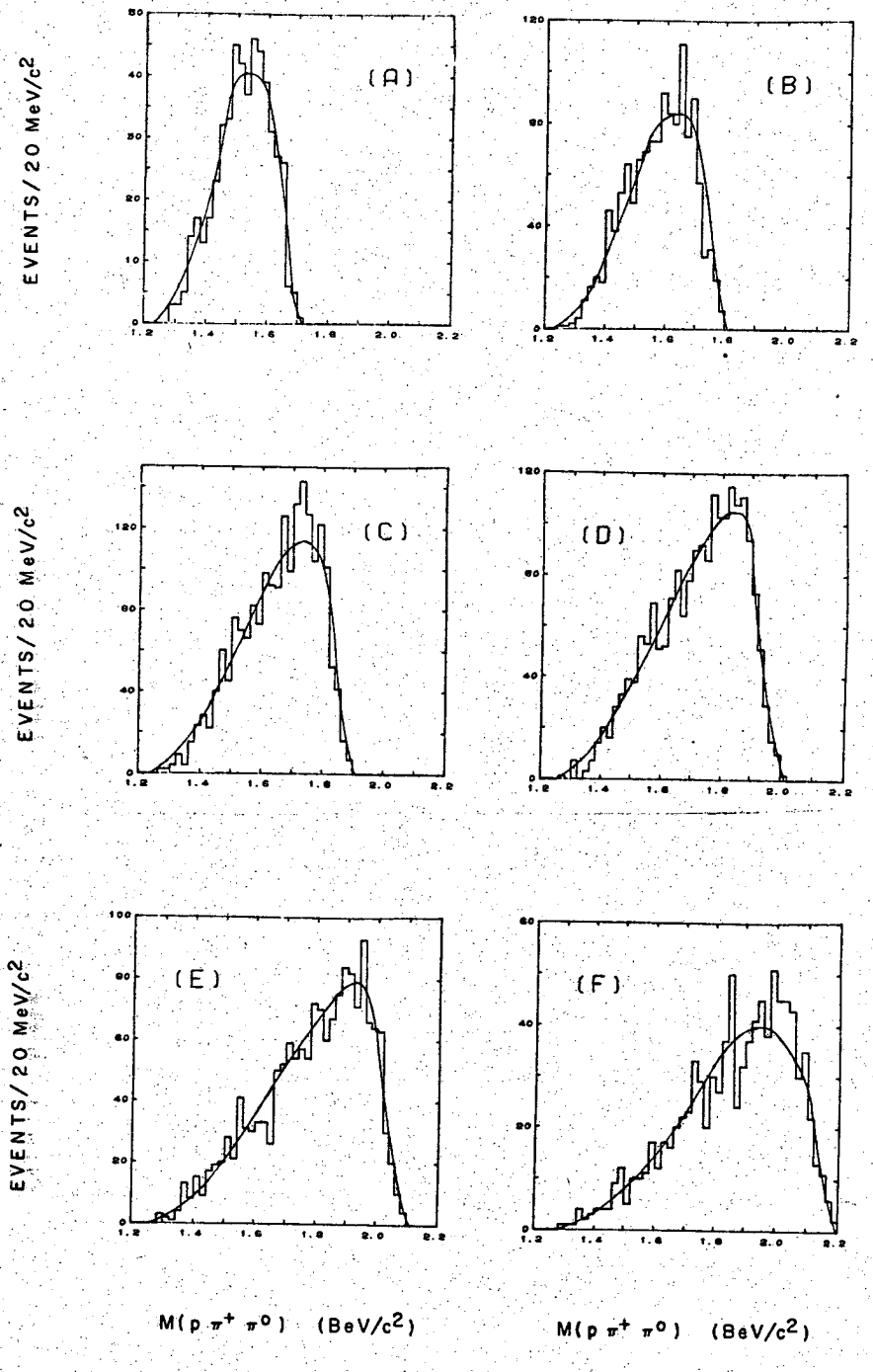

XBL 696-748

Figure 33. $m(p\pi^+\pi^0)$ in six 100 MeV-wide c.m. energy intervals centered at a) 1.8, b) 1.9, c) 2.0, d) 2.1, e) 2.2, and f) 2.3 BeV; the curves are from maximum-likelihood fits.

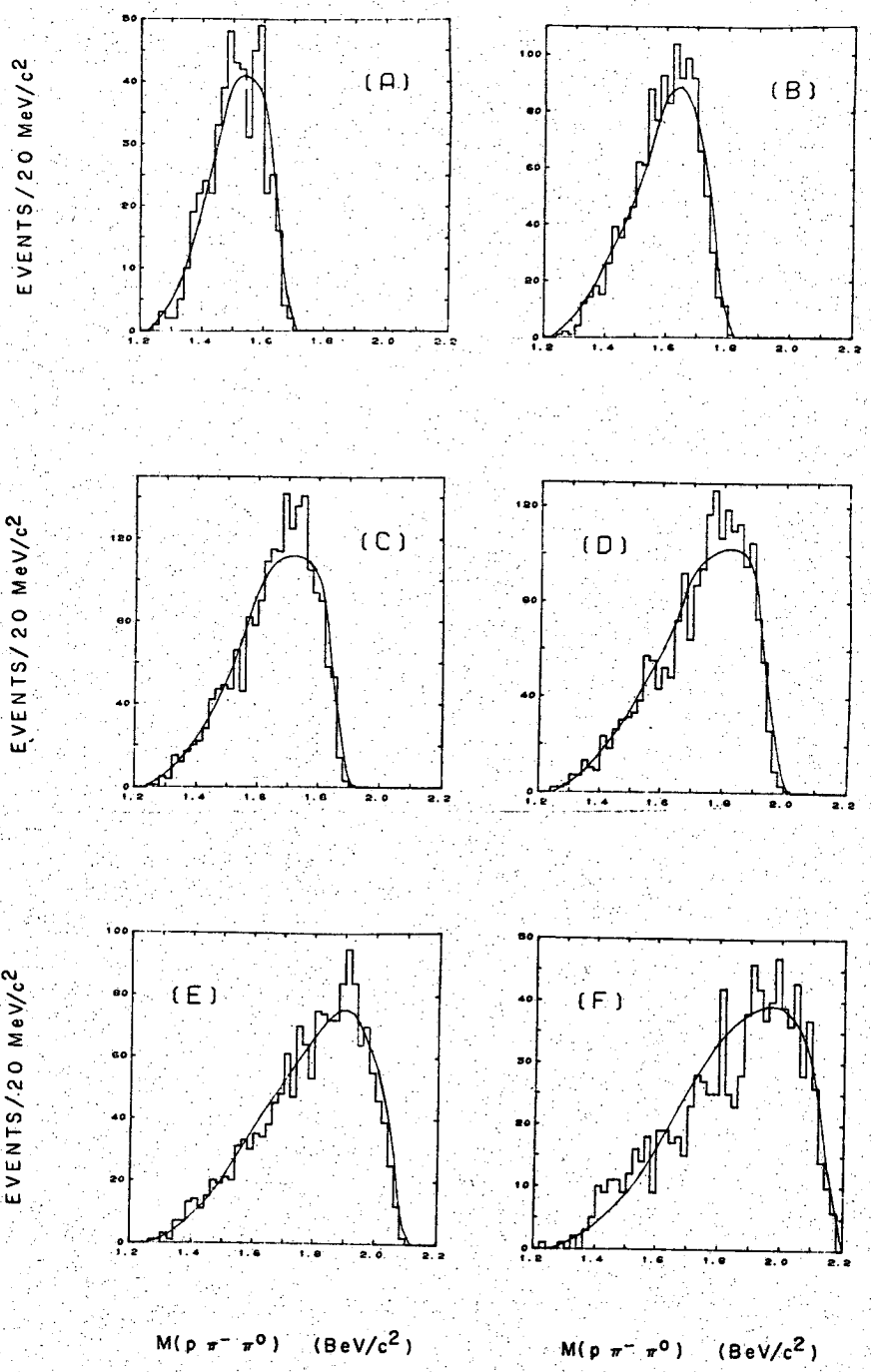

XBL 696-746

Figure 34. $m(p\pi^-\pi^0)$ in six 100 MeV-wide c.m. energy intervals centered at a) 1.8, b) 1.9, c) 2.0, d) 2.1, e) 2.2, and f) 2.3 BeV; the curves are from maximum-likelihood fits.

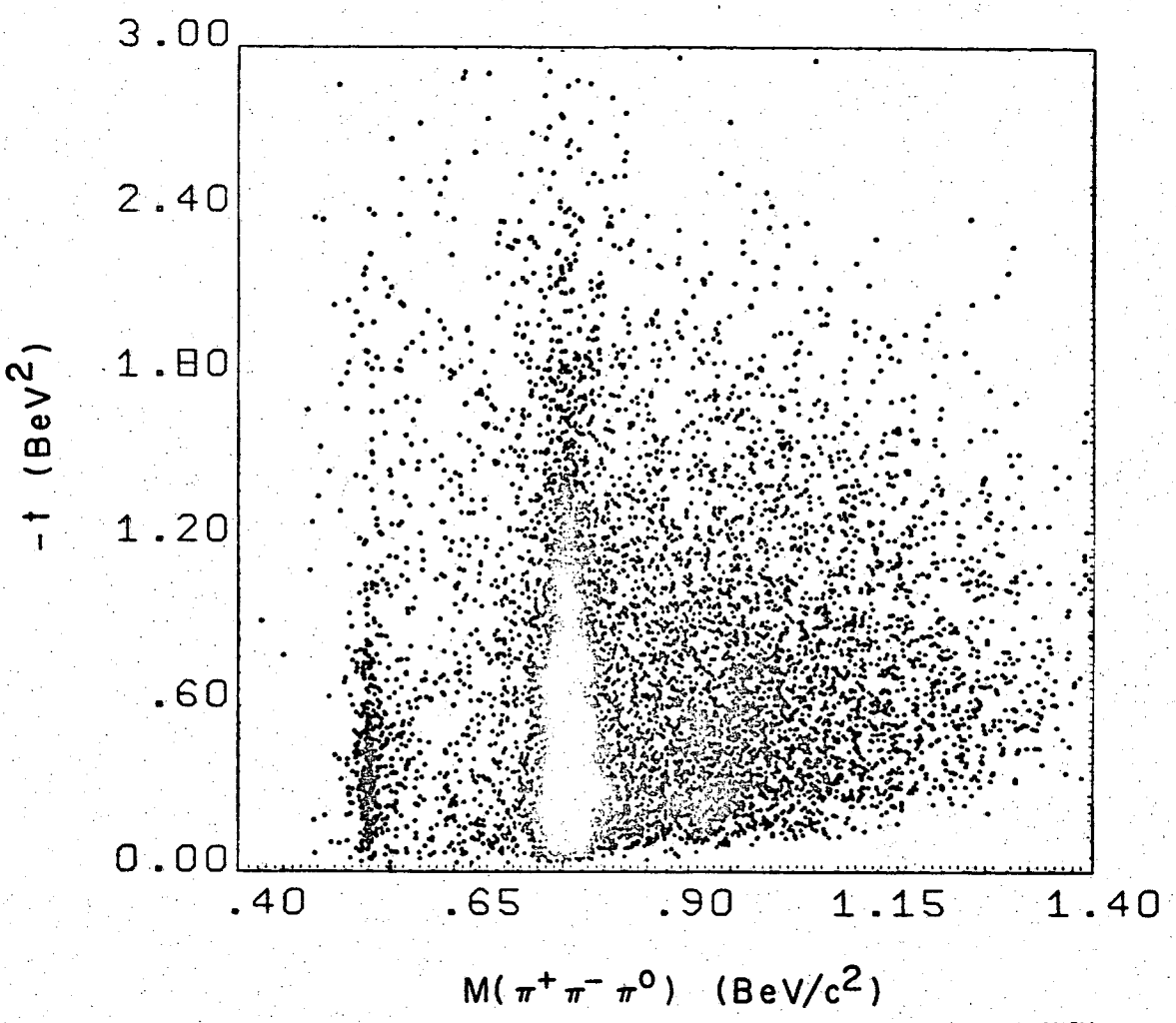

Figure 3b. $m(\pi^+\pi^-\pi^0)$ vs. -t(beam to $\pi^+\pi^-\pi^0$).

are combined in the plot, so that there is not a well-defined boundary, as there would be if the c.m. energy had a single value. Therefore the distribution of points in the vertical direction is not equivalent to the production angular distribution. However, it is apparent from the figure that ω's are produced out to -t of over 1.5 BeV^2, whereas η production occurs only out to about -t = 1 BeV^2.

Although there is no obvious structure in the 3-pion mass spectra of Figures 15 and 25 above the ω mass, we will examine the possibility of the presence of the H(990), φ(1019), and A-mesons, all of which have $\pi^+\pi^-\pi^o$ decay modes reported.

The H meson, with mass around 990 MeV/c^2 and decaying into $\pi^+\pi^-\pi^o$ via $\rho\pi$, has been reported previously.[21b, 21c, 21d, 20g, 38] More recently Galtieri and Söding,[39] and Fung et al.,[40] have shown that the evidence for the H(990) is not compelling. As noted above in reference to Figures 29, 30, and 31, there is only a very small ρ signal in the $\pi^+\pi^-$, $\pi^+\pi^o$, and $\pi^-\pi^o$ mass combinations. Nevertheless the $\pi^+\pi^-\pi^o$ mass spectrum has been reexamined under the constraint that the $\pi\pi$ mass combinations lie in the ρ mass band (650 MeV/c^2 < m($\pi\pi$) < 850 MeV/c^2). Figures 36, 37, 38, and 39 show the $\rho\pi$ mass vs. c.m. energy and $\rho\pi$ mass distribution for the combinations $\rho^o\pi^o$, $\rho^+\pi^-$, $\rho^-\pi^+$, and all $\rho\pi$, respectively. Only the $\rho^o\pi^o$ mass spectrum with -t(beam to 3 pions) < 0.6 BeV^2 shows an enhancement around the hypothesized H-mass of 990 MeV/c^2; it appears as an excess of 30 to 35 events around a mass of 970 MeV/c^2. However, the total estimated number of decays of the type $\eta' \rightarrow \eta\pi\pi$ for events with "goodness" and spectator momentum cuts equivalent to those in this report is approximately 120.[41] Using the

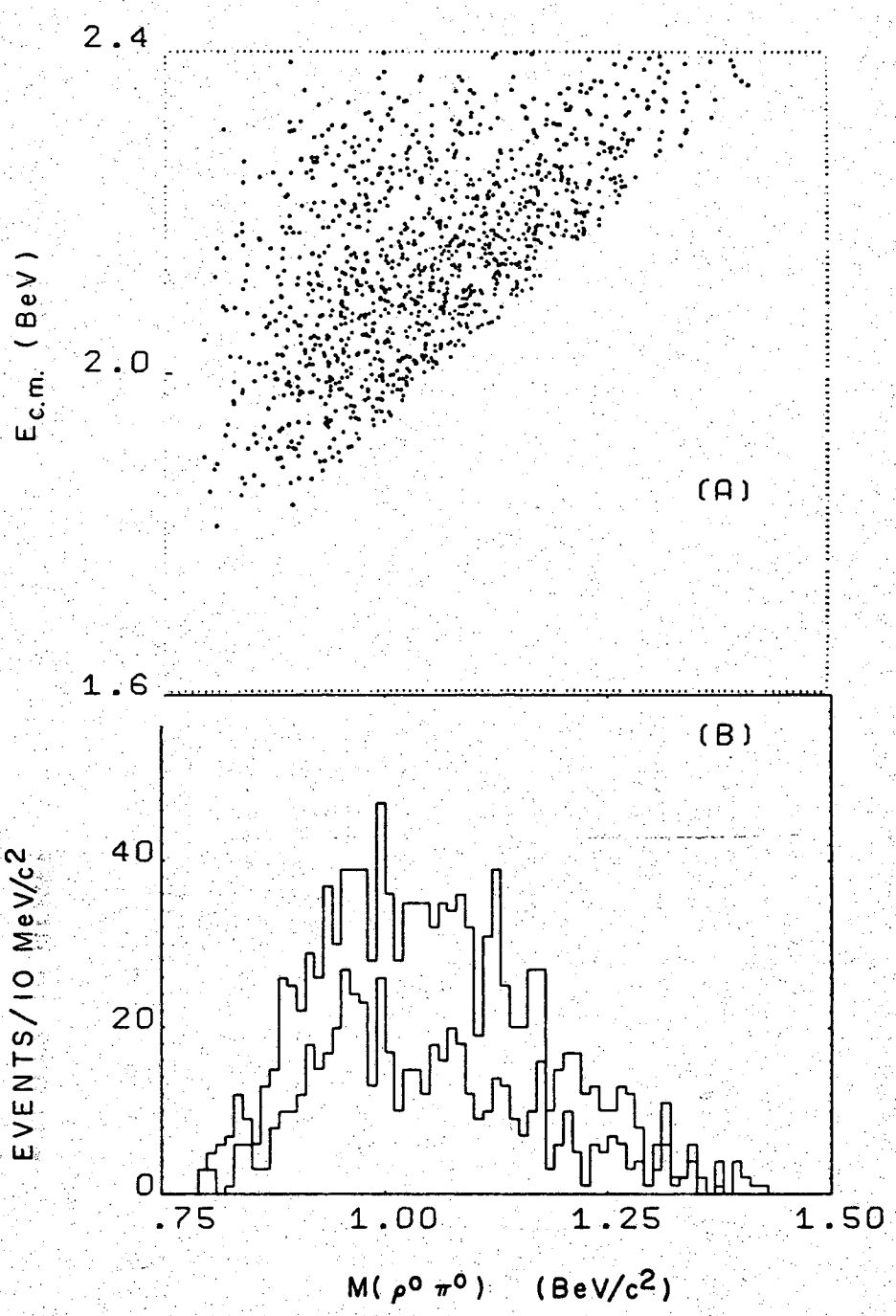

Figure 36. a) $m(\rho^0\pi^0)$ vs. c.m. energy; b) $m(\rho^0\pi^0)$, the lower histogram has events with $-t(\text{beam to } \rho^0\pi^0) < 0.6$ BeV^2.

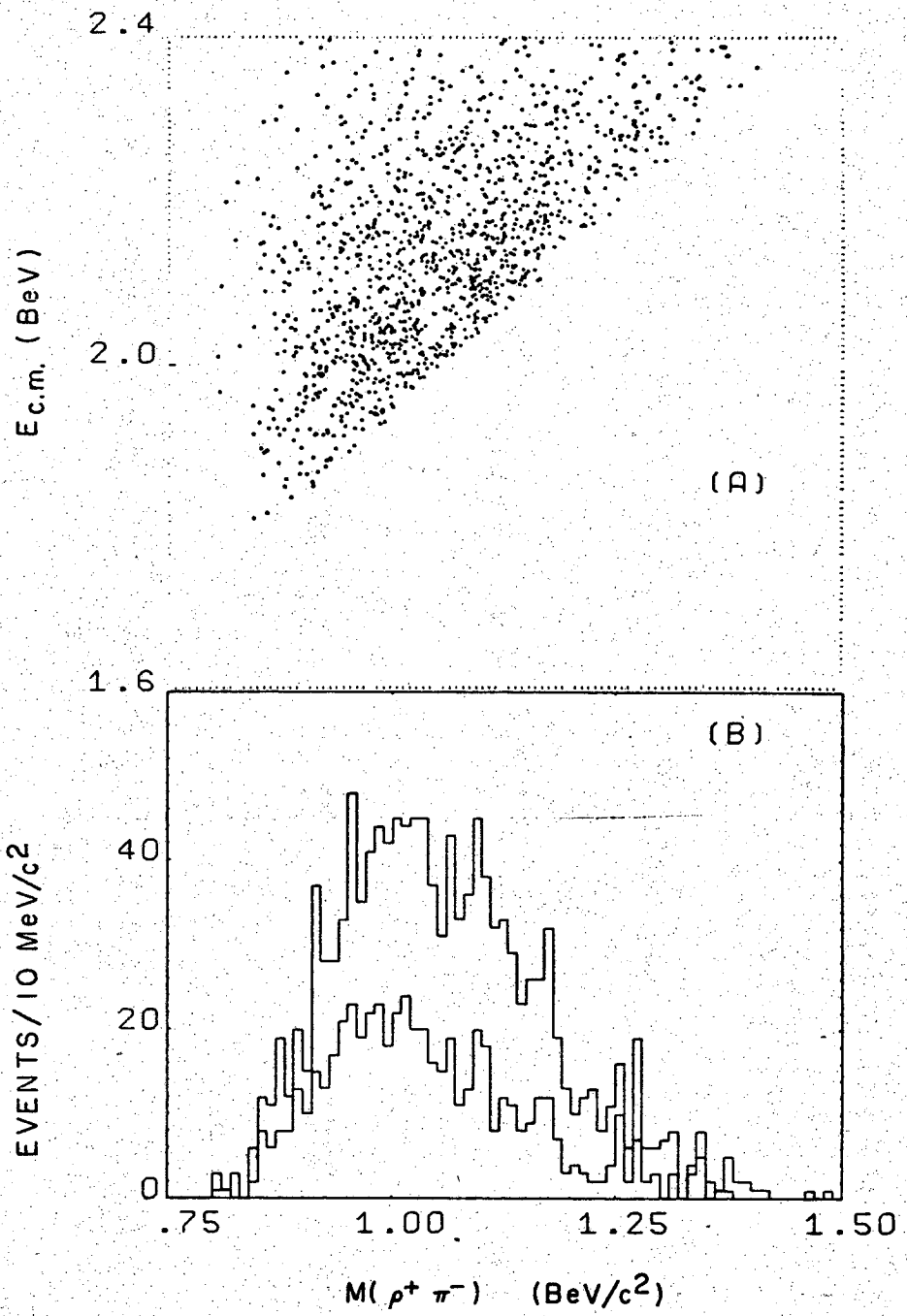

Figure 37. a) $m(\rho^+\pi^-)$ vs. c.m. energy; b) $m(\rho^+\pi^-)$, the lower histogram has events with $-t(\text{beam to } \rho^+\pi^-) < 0.6$ BeV^2.

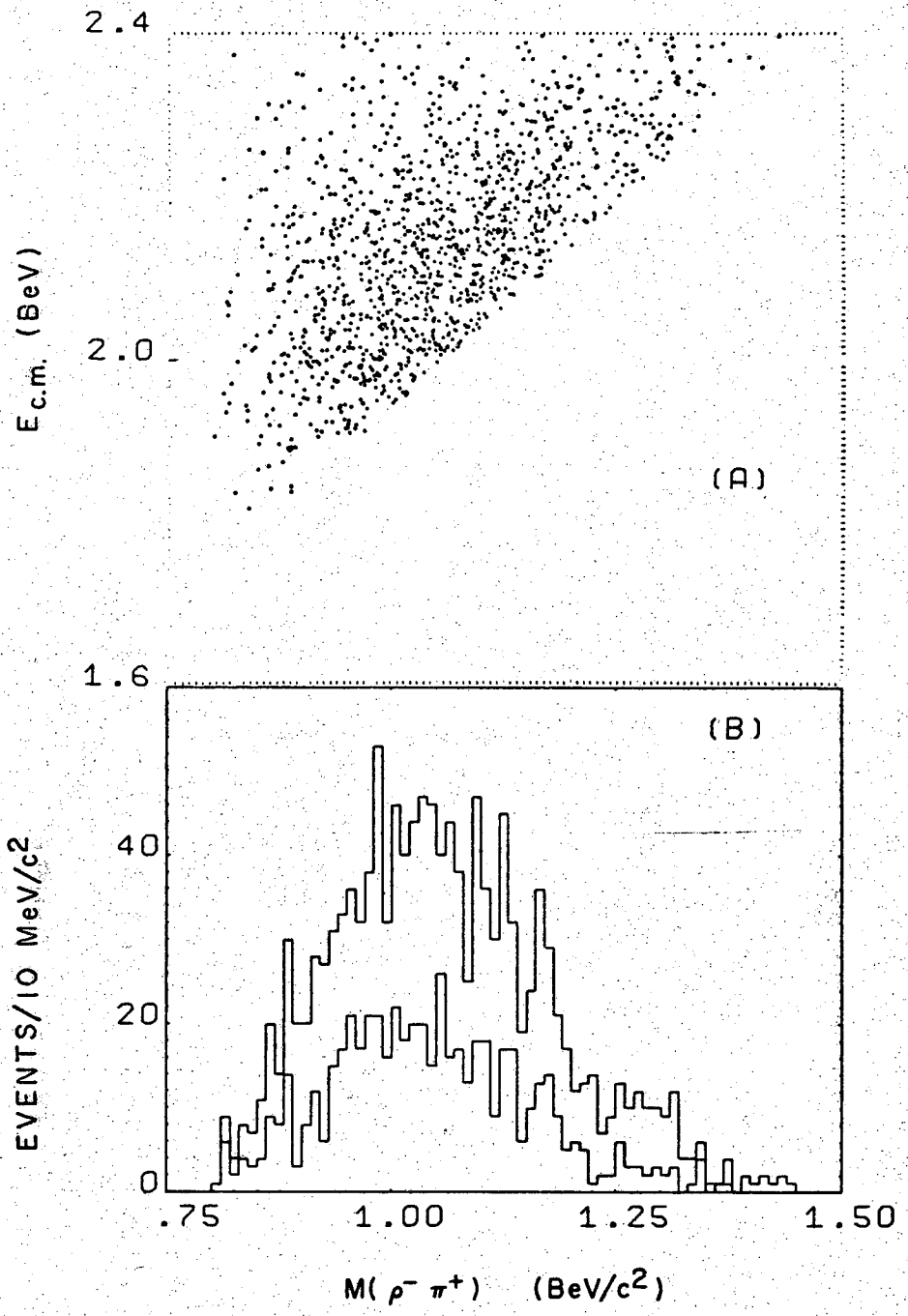

Figure 38. a) $m(\rho^-\pi^+)$ vs. c.m. energy; b) $m(\rho^-\pi^+)$, the lower histogram has events with $-t(\text{beam to } \rho^-\pi^+) < 0.6$ BeV^2.

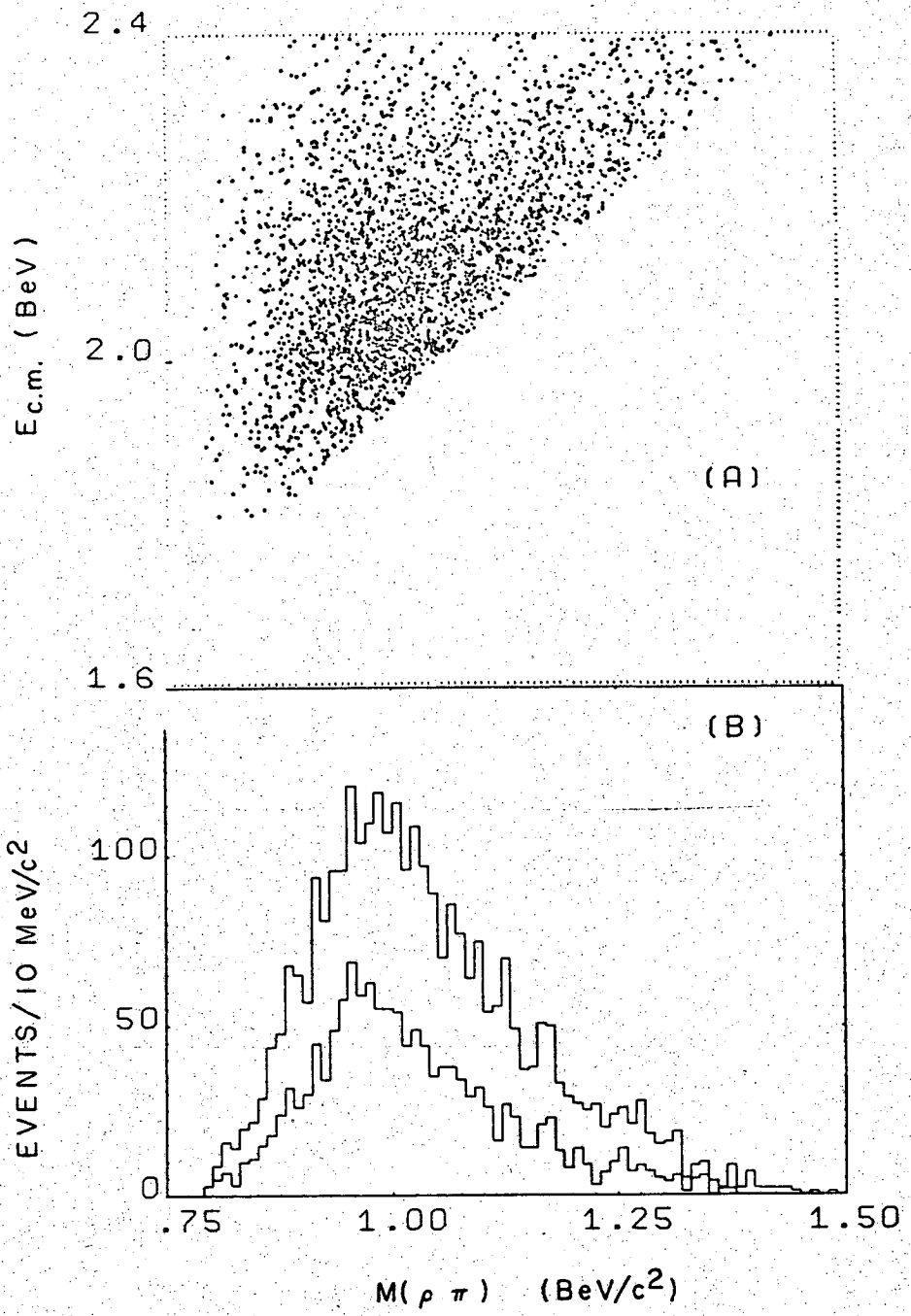

XBL 696-733

Figure 59. a) $m(\rho\pi)$ vs. c.m. energy; b) $m(\rho\pi)$, the lower histogram has events with $-t(\text{beam to } \rho\pi) < 0.6$ BeV^2.

branching ratio

$$(\eta' \to \eta\pi\pi)/(\eta' \to \pi^+\pi^-\gamma(\text{including } \rho^o\gamma)\ ) \cong 3,^{26}$$

an estimated 40 $\pi^+\pi^-\gamma$ events should appear around the η' mass. Figure 40 shows the $\pi^+\pi^-\gamma$ mass spectrum for "good" 4-pronged events from reaction (II.4) with spectator momentum less than 300 MeV/c. There appears to be no excess of events around 960 MeV/c^2, and in fact there are only 15 events in the mass interval between 940 and 970 MeV/c^2. If we conclude that all the events containing the reaction

$$\pi^+ n \to p \eta', \quad \eta' \to \pi^+\pi^-\gamma \qquad \text{(IV.2)}$$

appear in the p p $\pi^+\pi^-\pi^o$ final state, then the 30 to 35 event bump in the $\rho^o\pi^o$ mass spectrum is consistent with the expected 40 events from reaction (IV.2). There remains no evidence for production of the H meson in this experiment.

The φ meson with mass 1019 MeV/c^2 has a reported $\pi^+\pi^-\pi^o$(including $\rho\pi$) decay fraction of 20 per cent.[26] The φ decays into K^+K^- with a listed branching ratio of 48 per cent, so 2.4 times as many K^+K^- decays of the φ are expected as 3-pion decays. However, the total number of events of the reaction

$$\pi^+ n \to p \varphi, \quad \varphi \to K^+K^- \qquad \text{(IV.3)}$$

in the "good" 4-pronged events is only 30 to 40,[3] so that only about 15 events from the reaction

$$\pi^+ n \to p \varphi, \quad \varphi \to \pi^+\pi^-\pi^o \qquad \text{(IV.4)}$$

are expected. It is clear from Figures 15 and 25 that such a small number of events will not be detectable. However, since the $\varphi \to 3\pi$ branching ratio of 20 per cent includes $\rho\pi$ events, we can examine the

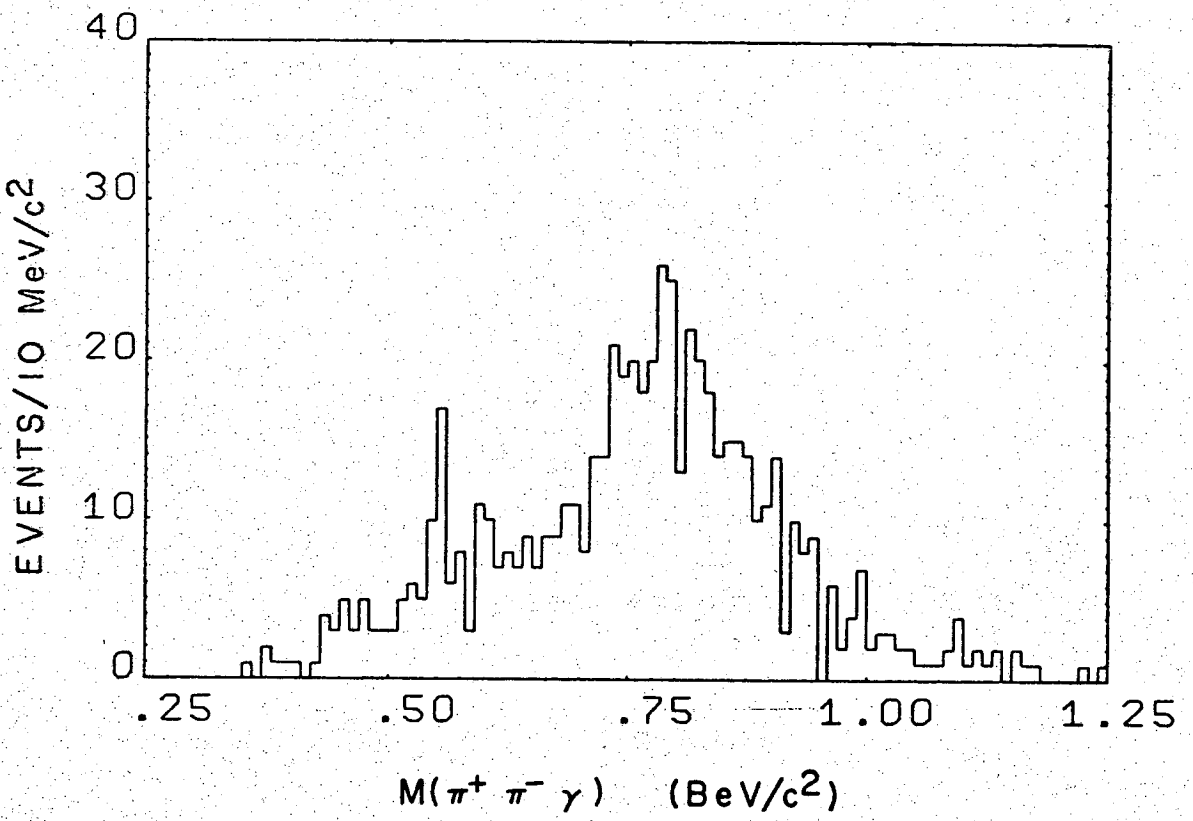

XBL 696-754

Figure 40. $m(\pi^+\pi^-\gamma)$ for "good" 4-pronged events from reaction (II.4) with spectator momentum less than 500 MeV/c.

$\rho\pi$ mass spectra of Figures 36 to 39, which, however, show no φ enhancement around 1019 MeV/c^2. The expected 15 φ events is an upper limit for the $\rho\pi$ decay mode, and since the φ has I = 0, the events should be divided up in the proportions

$$\rho^0\pi^0 : \rho^+\pi^- : \rho^-\pi^+ = 5 : 5 : 5,$$

and these three $\rho\pi$ spectra are of course consistent with having 5 extra events apiece around a mass of 1019 MeV/c^2. Figure 39, which is the sum of all the $\rho\pi$ spectra, also shows no noticeable enhancement around the φ mass, even with $-t < 0.6$ BeV^2, although it is consistent with the presence of up to 15 φ events.

It is noted that there seems to be no A_1 signal near 1080 MeV/c^2 in the 3-pion mass spectrum of Figures 15 and 25 or in any of the $\rho\pi$ spectra of Figures 36-39. At this point it should be stressed again that Figures 29-31 indicate that very little ρ of any charge is produced, so that the $\rho\pi$ spectra which have been examined for resonant signals consist of at least 80 per cent background.

Lastly, we remark trivially that no $A_2(1300)$ signal is detected in the 3-pion mass spectrum, because the highest energy of this experiment just barely reaches the threshold for A_2 production.

C. Cross Sections for the Reactions $\pi^+ n \rightarrow p\eta$, $\pi^+ n \rightarrow p\omega$

The cross sections for η and ω production were obtained by calculating the ratio $R_{res.}$ of the number of resonance (η or ω) events to the number of events fitting reactions (II.1) through (II.4), the sum of whose cross sections is required by charge symmetry to be equal to the sum of the cross sections (call this sum σ_{sum}) for the

processes

$$\pi^- p \rightarrow \pi^+ \pi^- n, \qquad \text{(IV.5a)}$$

$$\rightarrow \pi^+ \pi^- (mm). \qquad \text{(IV.5b)}$$

The resonance cross section is then $R_{res.} \cdot \sigma_{sum}$. The cross sections for reactions (IV.5) have been measured elsewhere[42] over the energy range of this experiment; the values of σ_{sum} used here are given in Table 6. Identical "event goodness" and spectator momentum cuts were made on all of reactions (II.1) through (II.4), and the fraction of η and ω events in reaction (II.2) was determined in 13 different c.m. energy intervals, each 50 MeV wide, centered at the values 1.75, 1.80, 1.85, ..., 2.35 BeV. The maximum-likelihood method was applied to find the fraction of η and ω events; in this series of fits the resonance masses were set at the average values seen from Table 5 (m_η = 549 MeV/c^2, m_ω = 785 MeV/c^2), and the widths as a function of c.m. energy were also obtained from Table 5 (interpolating where necessary). The cross section σ_{sum} was calculated by interpolating from Table 6. Table 7 summarizes the number of events and the fraction of resonant events found in each c.m. energy interval.

Cross sections were calculated for the processes

$$\pi^+ n \rightarrow p \eta, \qquad \text{(IV.6a)}$$

$$\rightarrow p \omega \qquad \text{(IV.6b)}$$

and are thus corrected for the branching ratios[26]

$$(\eta \rightarrow \pi^+\pi^-\pi^0(\text{or } \gamma)\ )/(\eta \rightarrow \text{all}) = .29, \qquad \text{(IV.7a)}$$

$$(\omega \rightarrow \pi^+\pi^-\pi^0)/(\omega \rightarrow \text{all}) = .90 \qquad \text{(IV.7b)}$$

In the calculation account was taken of the fact that not all of the

Table 6. Sum of cross sections for the reactions $\pi^- p \to \pi^+ \pi^- n$ and $\pi^- p \to \pi^+ \pi^-$ (mm) as a function of c.m. energy.

$E_{c.m.}$ (BeV)	σ_{sum} (mb)	source
1.618	11.5 ± 0.6	a)
1.716	11.4 ± 0.6	b)
1.726	10.4 ± 0.8	a)
1.795	10.4 ± 0.8	b)
1.872	11.1 ± 0.3	b)
2.030	12.0 ± 0.7	b)
2.181	11.6 ± 0.6	c)
2.232	11.8 ± 0.6	c)
2.309	10.7 ± 0.6	c)
2.405	10.4 ± 0.5	c)
2.504	9.0 ± 0.4	c)

a) E. Pickup et al., PR 132, 1819 (1963).

b) T. C. Bacon et al., PR 157, 1263 (1967).

c) L. D. Jacobs, UCRL 16877 (1966).

Table 7. Event numbers and resonant fractions as a function of c.m. energy in thirteen 50 MeV-wide c.m. energy intervals.

$E_{c.m.}$ (BeV)	events in reactions (II.1)-(II.4)	events in reaction (II.2)	η fraction in reaction (II.2)	ω fraction in reaction (II.2)
1.75	438	118	.124 ± .033	.480 ± .057
1.80	663	259	.071 ± .017	.539 ± .037
1.85	1 072	441	.099 ± .015	.502 ± .029
1.90	1 506	622	.050 ± .010	.404 ± .025
1.95	1 970	804	.051 ± .008	.377 ± .021
2.00	2 591	1 032	.029 ± .006	.289 ± .017
2.05	2 570	1 009	.034 ± .006	.320 ± .017
2.10	2 432	1 009	.030 ± .006	.289 ± .016
2.15	2 298	972	.033 ± .006	.254 ± .016
2.20	1 851	801	.029 ± .006	.300 ± .018
2.25	1 420	603	.016 ± .005	.217 ± .019
2.30	1 173	507	.017 ± .006	.205 ± .020
2.35	653	274	.010 ± .006	.210 ± .027

events with a $\pi^+\pi^-\gamma$ decay of the η were included in the events assigned to reaction (II.2). In fact, from the $\pi^+\pi^-\gamma$ mass spectrum of Figure 40 an estimated 26 η events remain classified as reaction (II.4), and are not included in the fit. From columns 3 and 4 of Table 7, it is found that there are around 318 η events in reaction (II.2), so the η cross sections were corrected by the factor 344/318 = 1.08, since the branching ratio (IV.7a) is used in the calculation.

As is discussed in Section III, the Glauber screening of the target neutron by the spectator proton and the effect of the Pauli exclusion principle in suppressing low-momentum-transfer processes should affect the cross section determination only insignificantly. The reason for this is basically that all of the reactions (II.1)-(II.4), which serve as the normalization cross section, are affected in similar proportions, so that the ratio of the number of resonant events to the number of normalization events is unaffected to a first approximation; in Section III a more complete discussion is presented.

The main uncertainty in the method arises from the spectator momentum cut ($p_{spec.} < 300$ MeV/c) applied to all the events used in the cross section determination. As was noted in Section III, each of reactions (II.1)-(II.4) has a different fraction of events with spectator momentum above 300 MeV/c, so that a different fraction of events is excluded from each reaction. However, as was stressed at the beginning of this section, events with spectator momentum less than 300 MeV/c conform well to the expectations of the impulse model, so that for each of the normalization reactions only those events are used for which it is likely that the target particle is a neutron,

and not the entire deuteron. Still, if scattering of the final-state pions on the spectator nucleon in reactions (II.1)-(II.4) is the cause of most of the high-momentum spectators, then differences in the amount of this scattering among the normalization reactions will lead to a systematic error caused by excluding different fractions of events for the different reactions (II.1)-(II.4). This systematic error could not be large, however, since the normalization reactions all have similar fractions of high-momentum spectators (see Section III).

It was noted in Section II that about 4 per cent of reaction (II.2) is actually contamination from reaction (II.6). From Table 7 it is seen that reaction (II.2) accounts for only about 40 per cent of the normalization reactions (II.1)-(II.4), so that this contamination is about 1.6 per cent of the normalization events. This implies that the cross sections for η and ω production should be increased by about this percentage, but since 1.6 per cent is so much smaller than the typical error of 15 per cent in the η and ω cross sections, the correction due to this contamination has been ignored.

Table 8 shows the cross sections obtained as described above for reactions (IV.6). The errors take into account the uncertainty in the resonance fractions of Table 7 and the errors in the normalization cross section of Table 6. As stated above, the cross sections are corrected for unseen η and ω decay modes. Figures 41 and 42 show the cross sections vs. c.m. energy for reactions (IV.6a) and (IV.6b), respectively.

The cross section for η production has been measured elsewhere,

Table 8. Cross sections for $\pi^+ n \to \eta p$ and $\pi^+ n \to \omega p$ as a function of c.m. energy.

$E_{c.m.}$ (BeV)	$\sigma(\pi^+ n \to \eta p)$ (mb)	$\sigma(\pi^+ n \to \omega p)$ (mb)
1.75	1.29 ± .44	1.49 ± .29
1.80	1.08 ± .35	2.44 ± .35
1.85	1.65 ± .33	2.50 ± .25
1.90	.86 ± .20	2.09 ± .20
1.95	.89 ± .19	1.97 ± .19
2.00	.50 ± .13	1.51 ± .17
2.05	.59 ± .14	1.67 ± .19
2.10	.55 ± .14	1.57 ± .18
2.15	.60 ± .14	1.39 ± .16
2.20	.55 ± .14	1.69 ± .19
2.25	.29 ± .12	1.18 ± .17
2.30	.30 ± .12	1.07 ± .16
2.35	.16 ± .11	1.03 ± .19

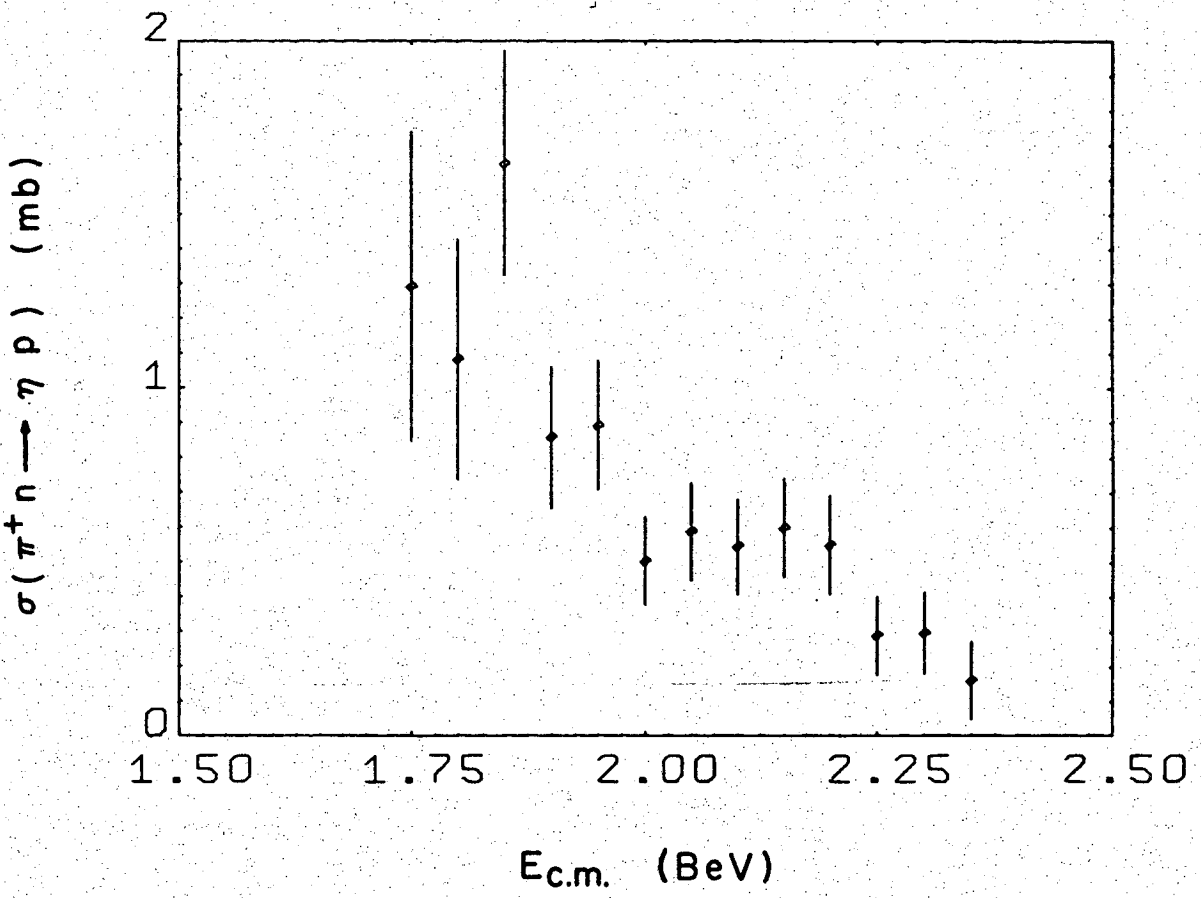

Figure 41. Cross section for $\pi^+ n \rightarrow \eta p$ vs. c.m. energy.

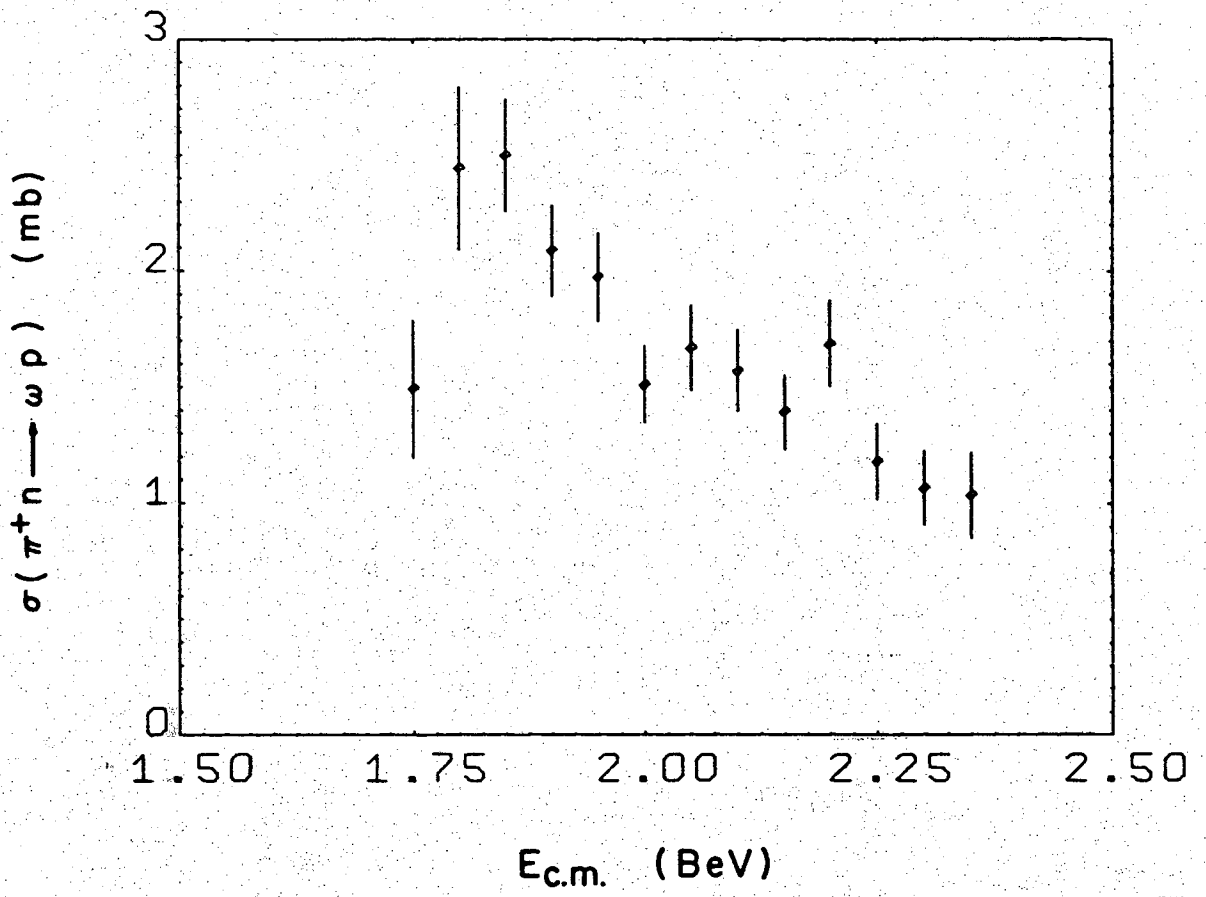

Figure 42. Cross section for $\pi^+ n \rightarrow \omega p$ vs. c.m. energy.

both for reaction (IV.6a) itself (by Bacon et al.[18c]) and for its charge-symmetric counterpart, $\pi^- p \rightarrow \eta n$ (by Bulos et al.,[43] Richards et al.,[44] Crouch et al.,[45] Wahlig and Mannelli,[46] and Guisan et al.[47]), which should have the same cross section. Likewise the cross section for reaction (IV.6b) has been measured at other energies, although much less extensively, both for process (IV.6b) itself (by Kraemer et al.,[17g] Bacon et al.,[18c] Miller et al.,[12] and Benson[21d]) and for its charge-symmetric version (by Boyd et al.[48]). Figure 43a is a logarithmic plot of the η cross section measured in this experiment, along with the data points of Bulos et al., Bacon et al., and Guisan et al. For the sake of clarity, the points of Richards et al., of Crouch et al., and of Wahlig and Mannelli are not included in the figure; the data of Richards et al. overlap and agree well with the points of Bulos et al., those of Crouch et al. overlap with those of this experiment and of Guisan et al., with which they do not entirely agree, and Wahlig and Mannelli have measured one point which agrees perfectly with one of the cross section points of Guisan et al. Figure 43b shows the ω cross section points of this experiment along with the data of Kraemer et al., Bacon et al., Boyd et al., Miller et al., and Benson, which for the most part do not overlap with those of this report.

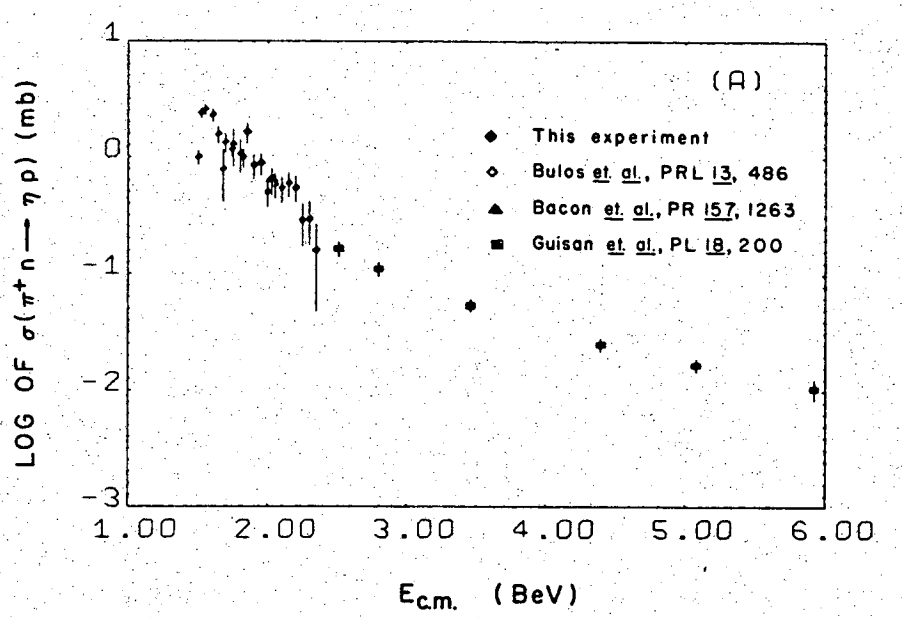

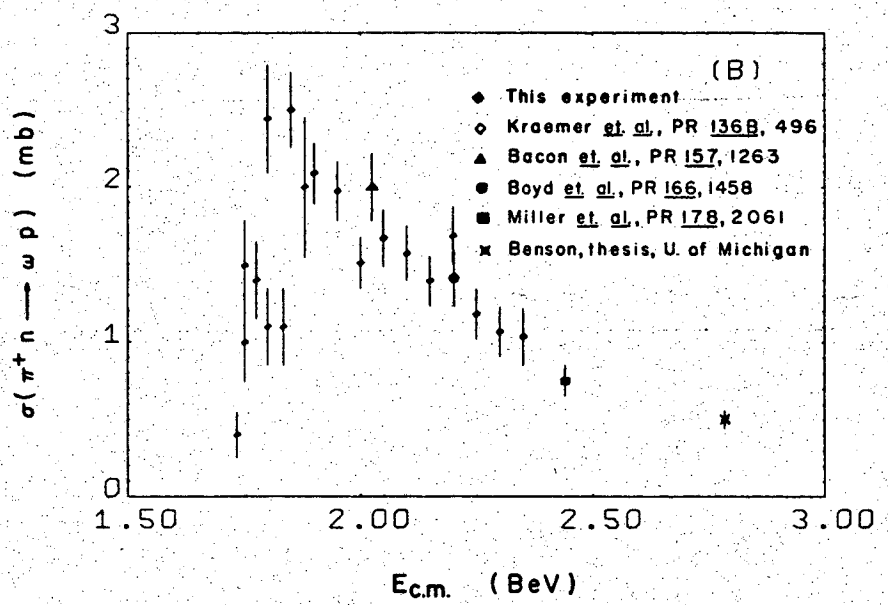

XBL 694-791

Figure 43. a) Logarithm of cross section for $\pi^+ n \rightarrow \eta p$ and $\pi^- p \rightarrow \eta n$ vs. c.m. energy, data are from this and three other experiments; b) cross section for $\pi^+ n \rightarrow \omega p$ and $\pi^- p \rightarrow \omega n$ vs. c.m. energy, data are from this and five other experiments.

V. η PRODUCTION AND DECAY IN THE REACTION $\pi^+ n \rightarrow \eta p$

Events referred to here as η events come from the decay $\eta \rightarrow \pi^+\pi^-\pi^o$(or γ). (About 10 per cent are estimated to be $\pi^+\pi^-\gamma$ decays; see Section IV.) The mass cut for the η selection is

$$530 \text{ MeV}/c^2 < m(\pi^+\pi^-\pi^o) < 570 \text{ MeV}/c^2.$$

These events also satisfy the "goodness" criteria defined in Section II and have spectator proton momentum less than 300 MeV/c. 349 such events lie within the η mass cut. The cross section for η production as a function of c.m. energy is given in the previous section.

A. The η Decay Dalitz Plot

Figure 44 is the Dalitz plot for the 3-pion decay of 349 η band events. The x-axis is $\sqrt{3}\ (T_+ - T_-)/Q$, and the y-axis is $3T_o/Q - 1$, where T_+, T_-, and T_o are, respectively, the kinetic energies (in the 3-pion rest frame) of the π^+, π^-, and π^o, and $Q = m_\eta - m_{\pi^+} - m_{\pi^-} - m_{\pi^o}$.

A topic of current interest is the violation of C-conjugation invariance in η decay into $\pi^+\pi^-\pi^o$ and $\pi^+\pi^-\gamma$.[49, 50, 51] An excess of events on either side of the vertical bisector of the η decay Dalitz plot of the form of Figure 44 is an indication of C-violation; a brief discussion of the reason for this is given in Appendix C. The fractional right-left asymmetry,

$$A = (R - L)/(R + L),$$

of the $\eta \rightarrow \pi^+\pi^-\pi^o$ Dalitz plot has been measured by a multi-university collaboration,[52] which found A = +.058 ± .034; by Cnops et al.,[53] who found A = +.003 ± .010; by Larribe et al.,[15a] who measured A = -.061 ± .040; by Baltay et al.,[14a] who found A = +.072 ± .028; and, most

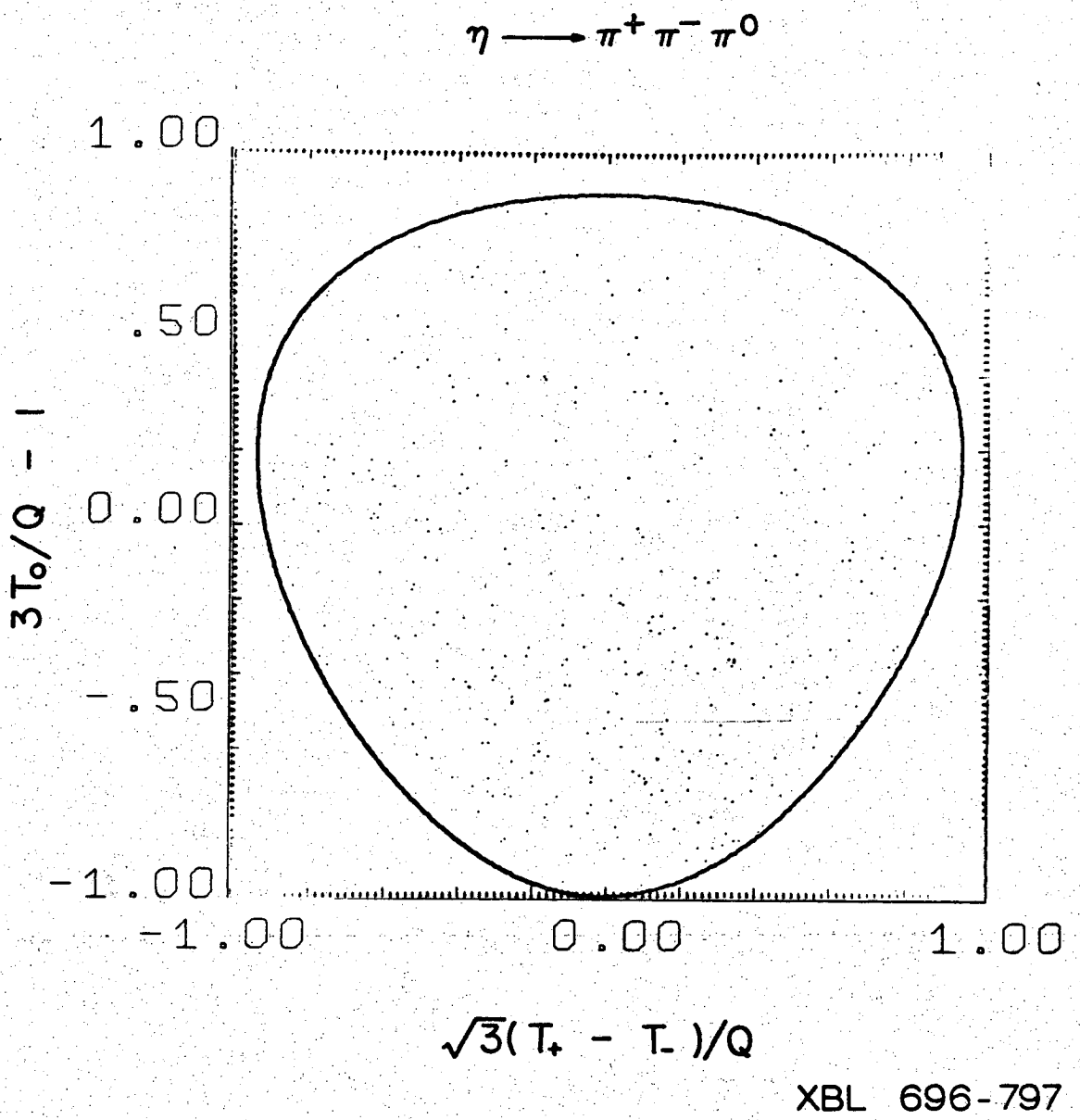

Figure 44. Dalitz plot of 340 events in the η mass band ($540\ MeV/c^2 < m(3\pi) < 570\ MeV/c^2$).

recently, by Gormley et al.,[54] who found A = +.015 ± .005. The asymmetry for the $\pi^+\pi^-\gamma$ decay of the η has also been measured (although with less precision than for the $\pi^+\pi^-\pi^o$ decay) by Crawford and Price,[55] who found A = -.02 ± .17; by Litchfield et al.,[15b] who measured A = -.04 ± .08; by Bowen et al.,[56] who found A = + .015 ± .025; and by Gormley et al.,[57] who obtained A = +.024 ± .014.

The right-left asymmetry in the decay Dalitz plot of the η events in this report is A = +.032 ± .054.

The variation along the vertical direction in the density of points in the $\eta \to \pi^+\pi^-\pi^o$ Dalitz plot of Figure 44 is a well-known feature of this decay, and it has been discussed as evidence for the existence of an intermediate $\pi^+\pi^-$ resonance in the decay.[58]

When the η decay into $\pi^+\pi^-\pi^o$ is fitted with a matrix element of the form

$$M(\eta \to \pi^+\pi^-\pi^o) = 1 + b\ (3T_o/Q - 1), \qquad (V.1)$$

Price and Crawford[59] find b = -.45 ± .05, and Cnops et al.[60] find b = -.55 ± .02.

Figure 45 shows the variation of density of points with the y-coordinate $3T_o/Q - 1$ for the Dalitz plot of Figure 44. The y-axis of Figure 45 is the density of points relative to that expected for uniform population of the Dalitz plot. The density was calculated under the assumption that of the events in the η mass cut, 86 per cent are true η events, and the rest are background uniformly distributed over the Dalitz plot. The background estimate is explained below in the discussion of the η production angular distributions. No account has been taken of the estimated 10 per cent of the η events which are

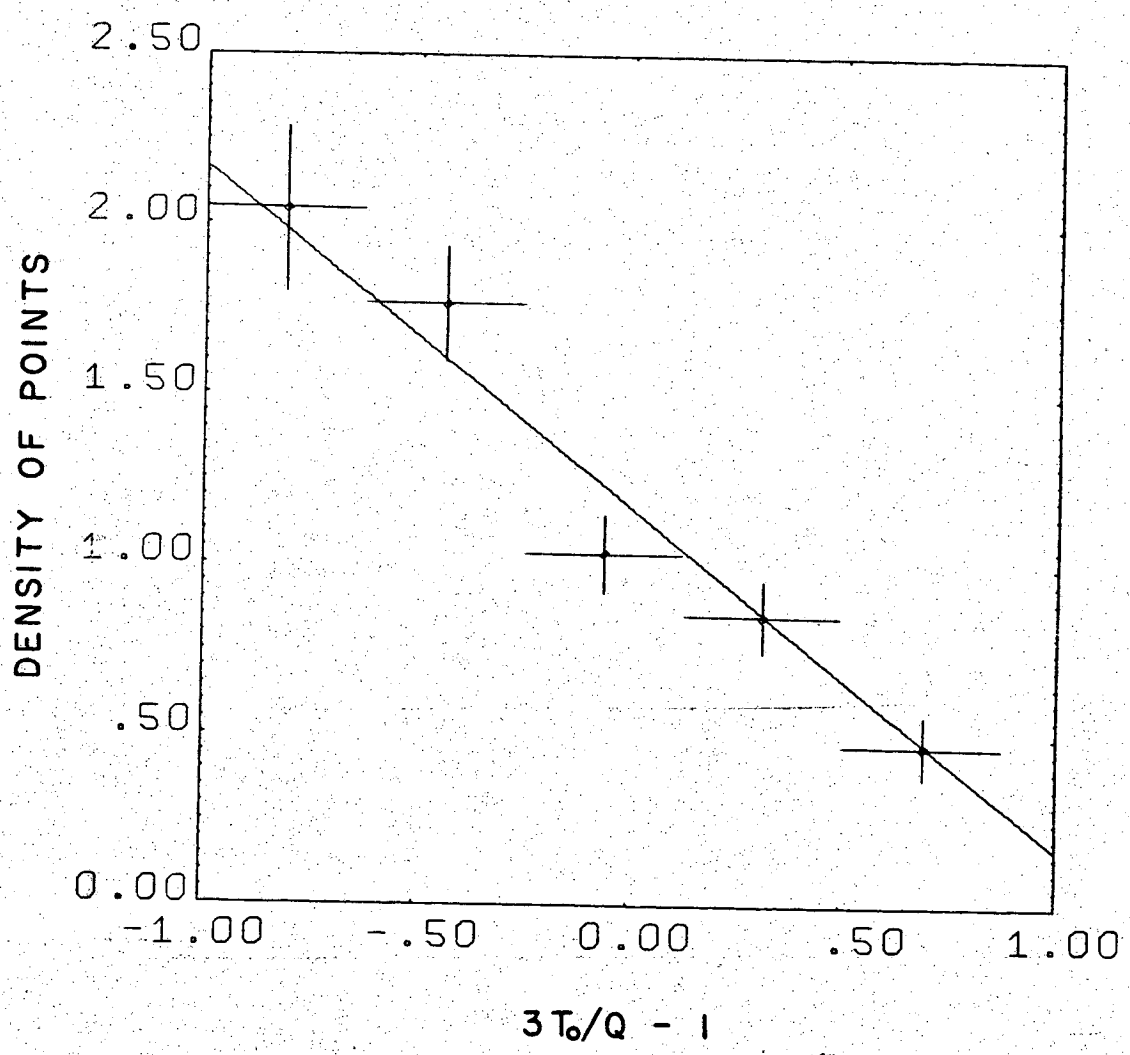

Figure 45. Relative density of points on the η Dalitz plot vs. $3T_o/Q - 1$. The straight line has slope -1.

really $\pi^+\pi^-\gamma$ decays. The straight line is a good fit to the points in the figure and has a slope of -1. Since, from equation (V.1),

$$\left|M(\eta \to \pi^+\pi^-\pi^o)\right|^2 \cong 1 + 2b\ (3T_o/Q - 1) \qquad (V.2)$$

(assuming that b is real), this gives

$$b = -.50 \pm .05$$

for the density variation factor for the η events in this experiment.

B. Production Angular Distributions for $\pi^+ n \to \eta p$

The production angle in this reaction is defined in the π^+n rest frame (the rest frame of the 4-vector $p_{\pi+} + p_d - p_{(p)}$) as the angle between the incoming π^+ beam and the outgoing $\pi^+\pi^-\pi^o$ momentum vector.

Appreciable numbers of events in the η band are found in the six 100 MeV-wide c.m. energy intervals centered at $E_{c.m.}$ = 1.7, 1.8, ..., 2.2 BeV; the first interval has 19 events, and the rest contain between 40 and 80 events apiece. From the assumed Gaussian line shape of the $\pi^+\pi^-\pi^o$ mass spectrum in the η mass region, it is possible to estimate the fraction of background events in the η mass cut in each c.m. energy interval, using the widths for the η signal given in Table 5. The background fraction estimates are .15, .07, .13, .17, .11, and .19, for the c.m. energy intervals centered at 1.7, 1.8, 1.9, 2.0, 2.1, and 2.2 BeV, respectively. The overall background fraction for all the events in the η mass cut is .14. The 3-pion production cosine distributions for 3-pion masses somewhat above the η mass cut (there are very few events with 3-pion mass below the η band) are

fairly flat at all c.m. energies. Assuming that the production angular distributions in this control region are the same as those of the background events in the η mass region, the background events (whose fractions are given above) were subtracted isotropically in production cosine from the production distributions for all events in the η band.

Figure 46 shows the production cosine distributions in the c.m. energy intervals mentioned above for events in the η band, with isotropic background subtracted in the amounts given above. The variable in the distributions is production cosine and not momentum-transfer-squared (-t), because the 100 MeV range of c.m. energies in each plot means that the maximum value of -t varies by typically 25 per cent over the plot. As an aid in estimating the t-distributions, Table 9 shows $(-t)_{minimum}$ and $(-t)_{maximum}$ for the reaction $\pi^+ n \rightarrow \eta p$ at a series of c.m. energy values. The shaded histogram contents in the forwardmost two bins are the estimated number of low-momentum-transfer events suppressed by the Pauli exclusion principle. Section III contains a discussion of this effect; in particular, see Table 4b. From the presence of the forward dip in the η production cosine distributions, and from the fact that the nucleon spin-flip amplitude must vanish in the forward direction, whereas the non-spin-flip amplitude need not, it is assumed that the Pauli principle correction factors to be used for the η production cosine distributions are those for the spin-flip amplitude.

The sharpness of the forward dip in the η production cosine distributions suggests that the dip may be due to an experimental bias in the sample of events.[61] Because only 4-pronged events (events with

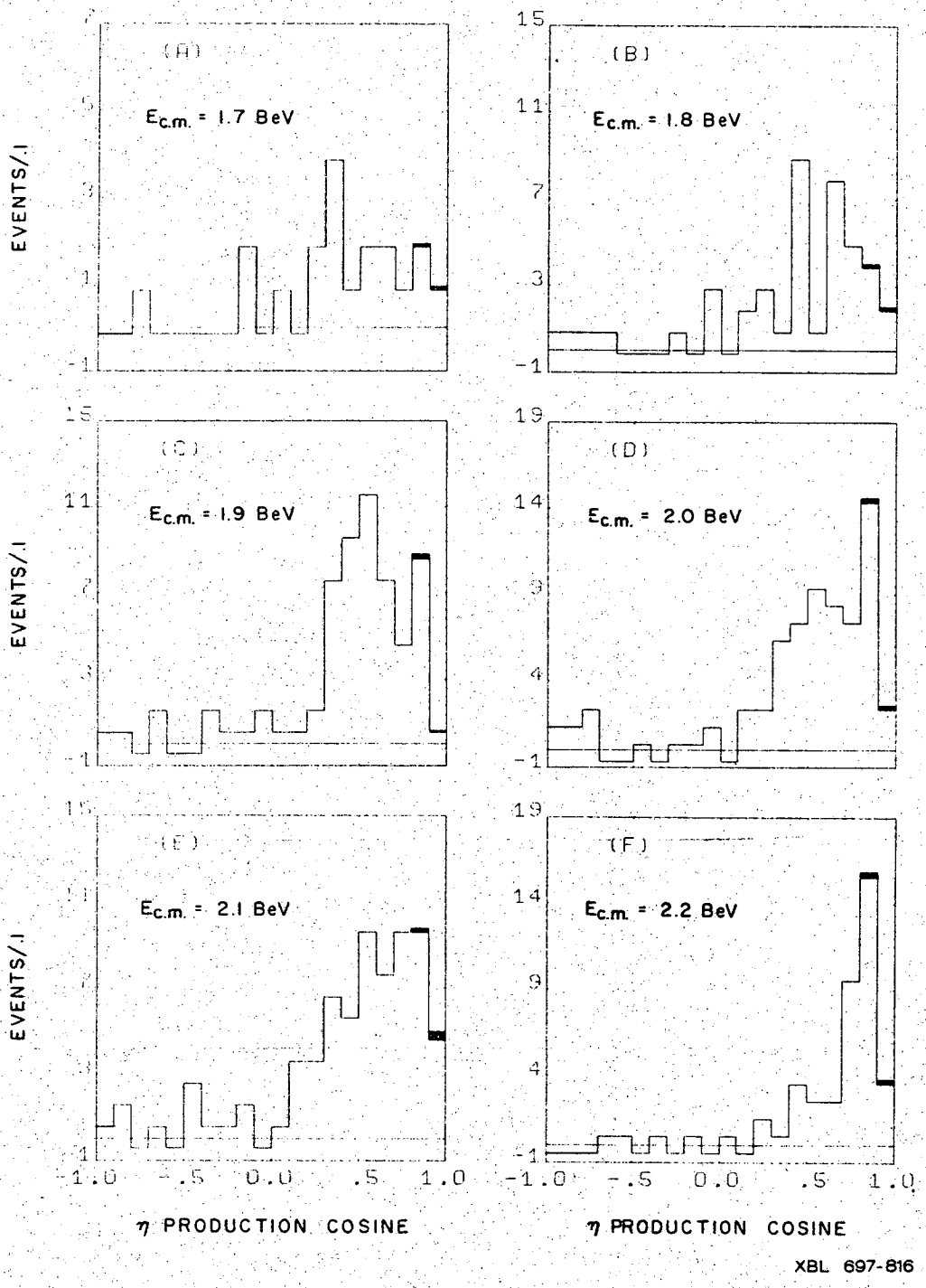

Figure 46. η production cosine distributions for six 100 MeV-wide c.m. energy intervals centered at the values indicated. The shaded events are added to account for the effect of the Pauli exclusion principle.

Table 9. Limits on momentum-transfer-squared as a function of c.m. energy for the reaction $\pi^+ n \rightarrow \eta p$.

$E_{c.m.}$ (BeV)	$(-t)_{min.}$ (BeV^2)	$(-t)_{max.}$ (BeV^2)
1.65	.032	.79
1.70	.025	.95
1.75	.020	1.12
1.80	.016	1.29
1.85	.014	1.47
1.90	.011	1.65
1.95	.010	1.84
2.00	.008	2.03
2.05	.007	2.23
2.10	.006	2.43
2.15	.006	2.64
2.20	.005	2.85
2.25	.004	3.07

two visible final-state protons) are used for this report, it is plausible that events with low momentum transfer may be lost into the sample of 3-pronged events in the following way: Since the target neutron, when it collides with an incoming π^+ and becomes a proton, is moving with a Fermi momentum of around 100 MeV/c in the laboratory system, it is possible that for low-momentum-transfer collisions many target neutrons are given just enough 3-momentum to make the laboratory momentum of the final-state proton below 85 MeV/c. Such a proton does not produce a visible track, and the event, which would normally appear as a 4-pronged event, is a 3-pronged event and does not appear in the sample of η's shown here. A Monte Carlo experiment was programmed to investigate this effect over a few values of c.m. energies covering the c.m. energy range of this experiment. It was found that this bias only affects the forwardmost bin of any of the η production cosine distributions presented, and that the correction for events lost from this bin into the 3-pronged events and into other production cosine bins due to misidentification of the spectator proton was at most 4 per cent, and typically 2 per cent. This correction cannot account for the sharpness of the forward dips seen in Figure 46, and it is ignored because of its smallness. It is thus felt that the sharp forward dips seen in the figure are a real attribute of the data.

C. A Regge Description of the Reaction $\pi^+ n \rightarrow \eta p$ Using Veneziano-Type Residue Functions

The concentration of events near the forward direction ($\cos\theta = 1$)

in Figure 46 suggests a description of the production process in terms of a t-channel pole, that is, in terms of particle or Regge-pole exchange. Figure 47 is a diagram illustrating this process; the exchanged pole is the $A_2(1300)$ meson with spin-parity of 2^+. The A_2 is the only known particle which can be exchanged in this reaction. This is because the upper vertex of the figure requires that an I = 1, G = - object be exchanged; of the four I = 1 possibilities, which are π, ρ, A_2, and B, ρ and B are excluded because they have G = +, and π is eliminated by spin and parity conservation, since the π has $J^P = 0^-$ (its Regge pole equivalent has unnatural spin-parity, i.e. $J,P = J, (-)^{J+1}$).

The differential cross section for this reaction, in terms of the invariant amplitudes A and B,[62] is

$$\frac{d\sigma}{d(\cos\theta)}\,(\text{mb}) = \frac{.3895\ M^2}{8\pi s}\frac{q_f}{q_i}\left\{\frac{p^2}{M^2}|A|^2 + \left[\left(\frac{s-u}{4M}\right)^2 + \frac{k^2 t}{4M^2}\right]|B|^2 - \left(\frac{s-u}{2M}\right)\mathrm{Re}(A^* B)\right\} \qquad (V.3)$$

Here s, t, and u are the usual Mandelstam variables, and

q_i = initial-state c.m. 3-momentum

q_f = final-state c.m. 3-momentum

k = t-channel meson momentum

$$= \left\{\left[t - (m_\pi + m_\eta)^2\right]\left[t - (m_\pi - m_\eta)^2\right]\right\}^{\frac{1}{2}} / 2\sqrt{-t}$$

p = t-channel baryon momentum

$$\sqrt{M^2 - t/4}$$

M = nucleon mass

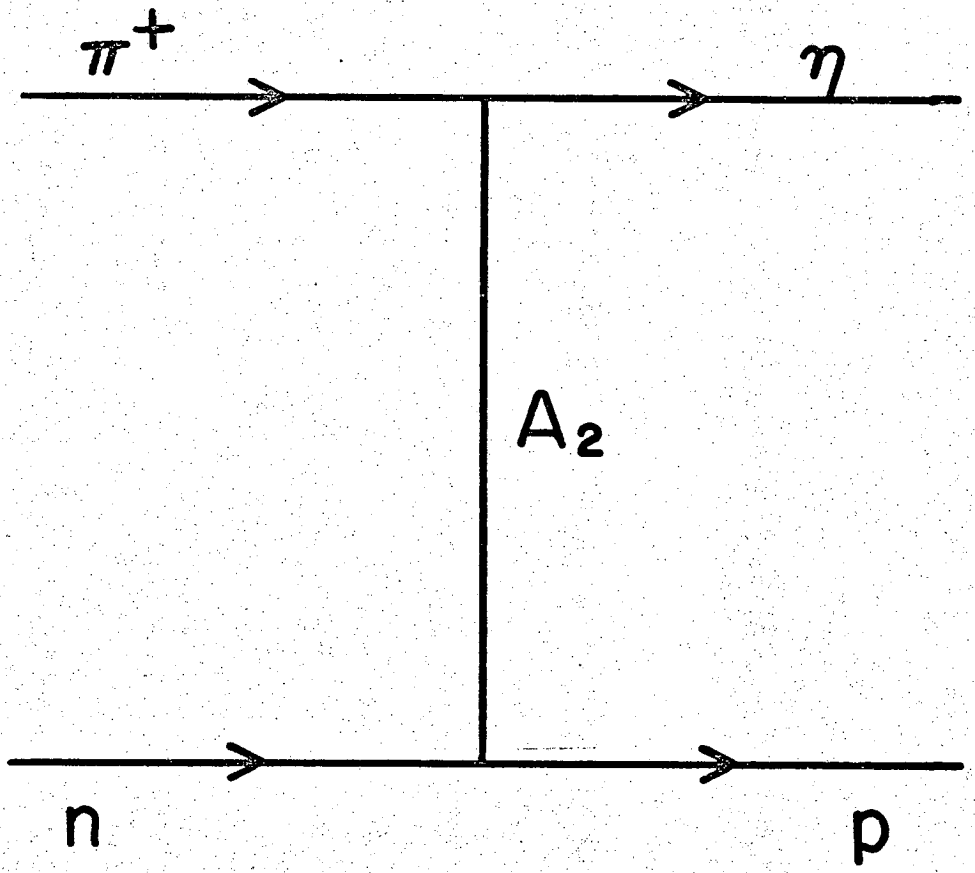

XBL 696-796

Figure 47. A_2-exchange diagram as a mechanism for the reaction $\pi^+ n \to \eta p$.

All masses and momenta are in BeV. The Regge form of the invariant amplitudes A and B is the leading order in s of a Veneziano parametrization:[62]

$$A\ (\text{BeV}^{-1}) = a_o \Gamma(1 - \alpha(t))(1 + e^{-i\pi\alpha(t)})(b's)^{\alpha(t)} \qquad (V.4a)$$

$$B\ (\text{BeV}^{-2}) = b_o \Gamma(1 - \alpha(t))(1 + e^{-i\pi\alpha(t)})(b''s)^{\alpha(t)-1} \qquad (V.4b)$$

For a discussion of the invariant amplitudes A and B, and for an elucidation of the function $\Gamma(1 - \alpha(t))$ as the Veneziano form for the Regge residue function, the reader is referred to Appendix D. $\alpha(t)$ is the A_2 trajectory function, which is taken to be the straight-line form

$$\alpha(t) = 2 + b\ (t - m_{A_2}^2) = 2 + b\ (t - 1.69) \qquad (V.5)$$

This parametrization is similar to the standard Regge treatment of t-channel helicity amplitudes,[63] but the Veneziano model demands that

$$b'' = b' = b \qquad (V.6)$$

be the universal slope of the linear trajectories. Hence, taking the universal slope b from experiment to be 1 BeV^{-2}, A and B are prescribed up to the real constants a_o and b_o, the only parameters of our fit.

A least-squares fit to the shape only of the η production angular distributions results in the choice

$$b_o/a_o = 2.4 \qquad (V.7)$$

as the ratio of magnitudes giving the best fit, which is displayed upon the six production cosine distributions in Figure 48. The curves on the production distributions all satisfy equation (V.7), but they are normalized separately to have the same area as the respective histogram in Figure 48. It will be seen below, however, that a single

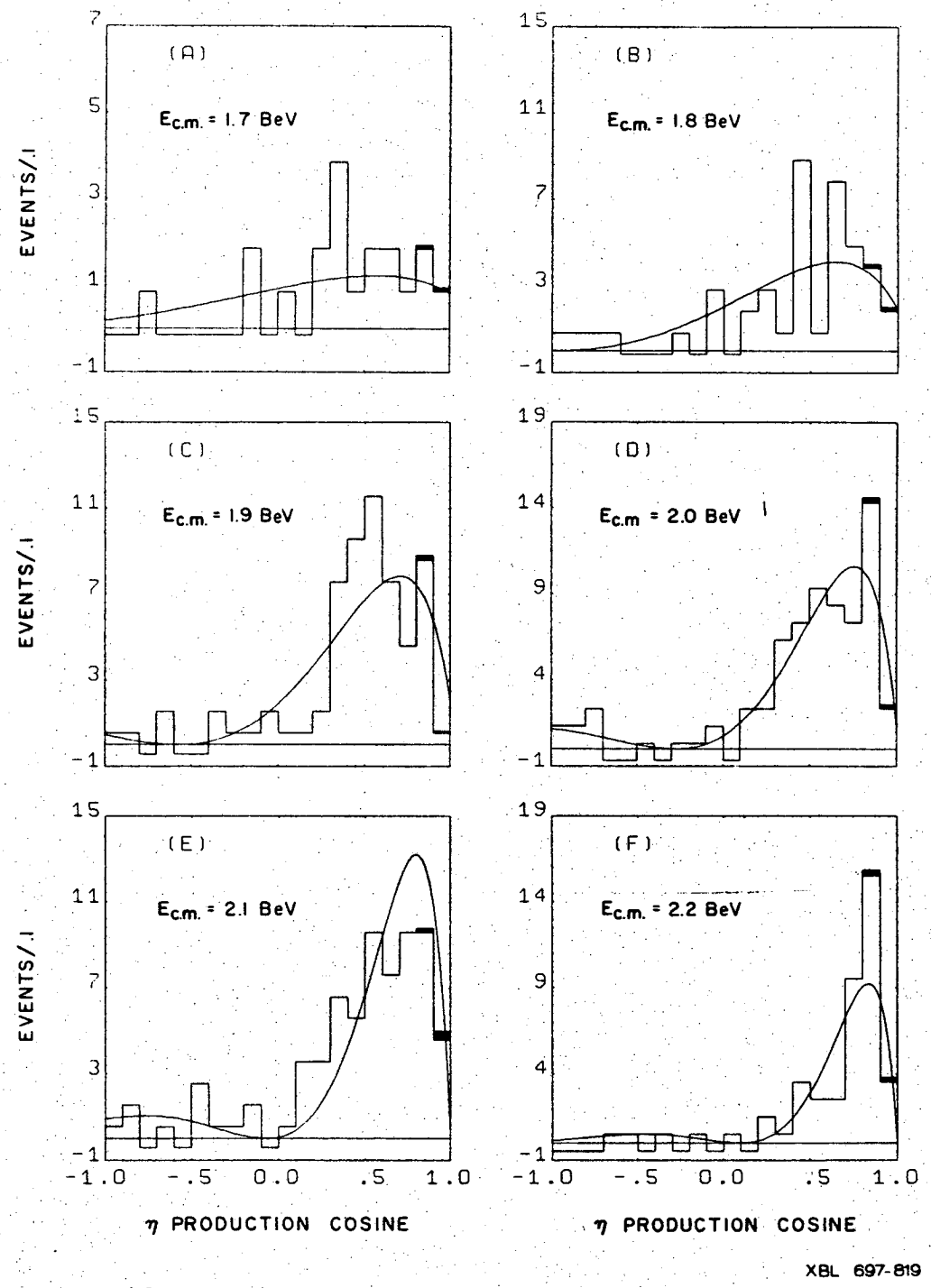

Figure 48. η production cosine distributions for six 100 MeV-wide c.m. energy intervals centered at the values indicated. The shaded events are added to account for the effect of the Pauli exclusion principle. The curves are the predictions of the Reggeized A_2-exchange model with $b_o/a_o = 2.4$; they are normalized to have the same area as the histograms.

choice of scale factor, i.e. a unique choice of a_o and b_o, fits both the shape and absolute scale of all distributions. The zero in the curves at $t = -1.3$ BeV^2 occurs because the signature factors in amplitudes (V.4) go to zero when $\alpha(t)$ passes through -1.

The energy dependence of the total cross section for this reaction and its charge-symmetric counterpart have also been compared to the model. The cross sections of references 18c, 43, and 47, as well as the data points of this experiment were used to test the validity of the energy dependence of the total cross section predicted by the model; these data points span the c.m. energy interval from threshold for the reaction up to almost 6 BeV, the highest energy at which it has been studied. Figure 49 is a plot of the total cross section for reaction (IV.6a) and its charge-symmetric equivalent vs. c.m. energy, along with the prediction of the Reggeized A_2-exchange model; the data points are the same as those in Figure 43a. With $b_o/a_o = 2.4$, and the value of a_o chosen so that the curve passes through the arbitrarily selected data point at $E_{c.m.} = 3.46$ BeV, the fit is seen to be very good over the entire range of energies. The energy dependence of the curves is seen to be quite sensitive to the value of b_o/a_o; agreement with the total cross section data is obtained only for the ratio b_o/a_o within ± 5 per cent of the value 2.4, which is the <u>same</u> ratio needed, within ± 10 per cent, in order to fit the <u>shape</u> of the production angular distributions! Furthermore an A_2 trajectory slope of 1 BeV^{-2} ± 10 per cent is necessary to fit the width of the experimental production cosine distributions, and this is in accordance with a universal trajectory slope of 1 BeV^{-2}.

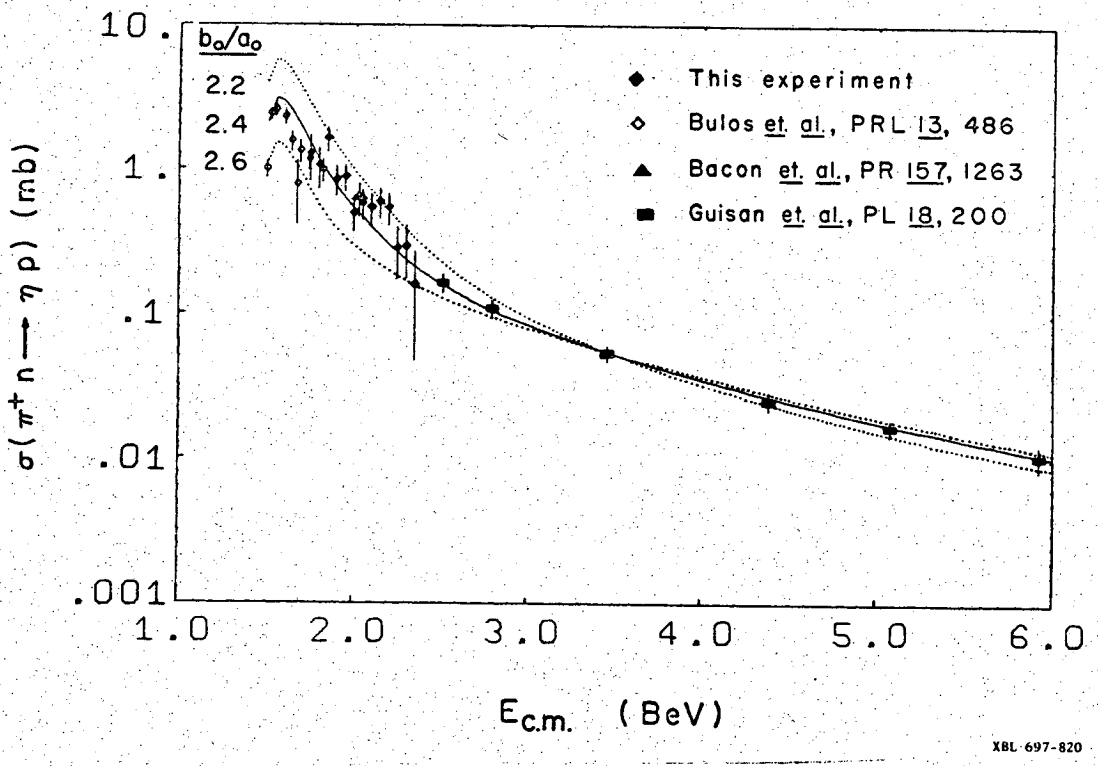

Figure 49. Cross section for $\pi^+ n \rightarrow \eta p$ or $\pi^- p \rightarrow \eta n$ vs. c.m. energy. Three predictions of the Reggeized A_2-exchange model are plotted; all curves are normalized to pass through the data point at $E_{c.m.}$ 3.46 BeV.

The parameter values used to obtain the fit to the shape of our production angular distributions and to the total cross section over a wide range of energies are

$$a_o = 28.7, \quad b_o = 68.8 \tag{V.8}$$

Figure 50 shows the differential cross section $d\sigma/dt$ for

$$\pi^- p \rightarrow n \eta, \quad \eta \rightarrow \gamma \gamma \tag{V.9}$$

from reference 47 at c.m. energies above 2.50 BeV, along with the predictions of the Reggeized A_2-exchange model; the curves are normalized to have the same area as the histograms. The agreement between the experimental distributions and the model is seen to be satisfactory; the total cross section points of this reference are in excellent agreement with the model, as is seen from Figure 49. Figure 51 shows differential cross section measurements from two more experiments. In Figure 51a the differential cross section measured by Benson[21d, 21e] is compared with the model. Here the agreement is quite good except for the greater number of events at large values of -t than is predicted by the model. However, it should be noted that the experimental distribution of Figure 51a includes events from reaction (II.2) with spectator proton momentum greater than 300 MeV/c. These are events which are suspected not to arise from π^+ collisions with only one of the nucleons in the deuteron, and they are at the same time events which are likely to have large momentum transfer values, since both final-state protons have laboratory momentum greater than 300 MeV/c. It is further noted that the sharp forward dip in Figure 51a is in disagreement with the equivalent distribution

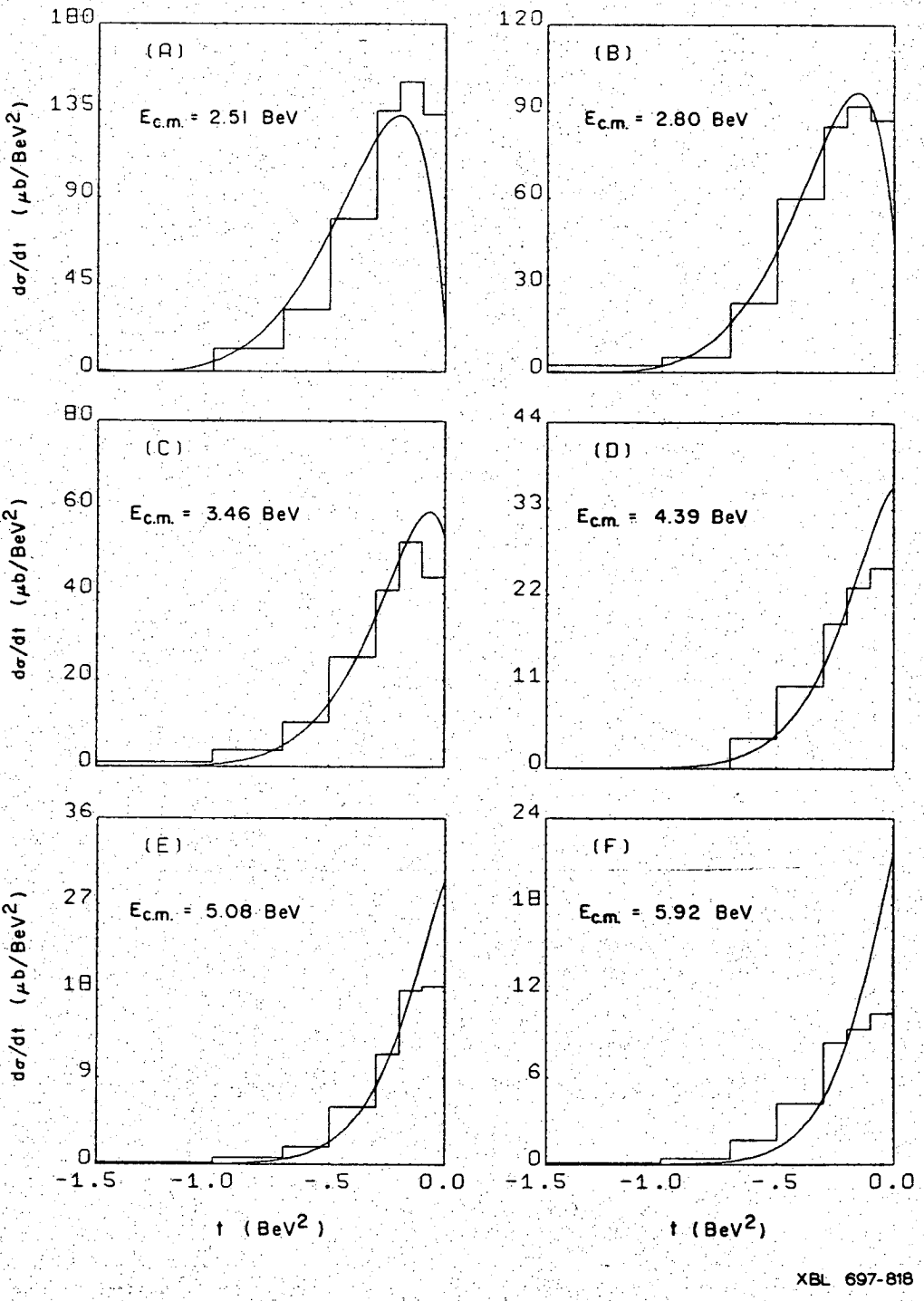

Figure 50. Differential cross sections for $\pi^- p \to \eta n$ from Guisan et al., PL 18, 200 (1965). The curves are the Reggeized A_2-exchange model predictions with b_0/a_0 = 2.4 and are normalized to have the same area as the histograms.

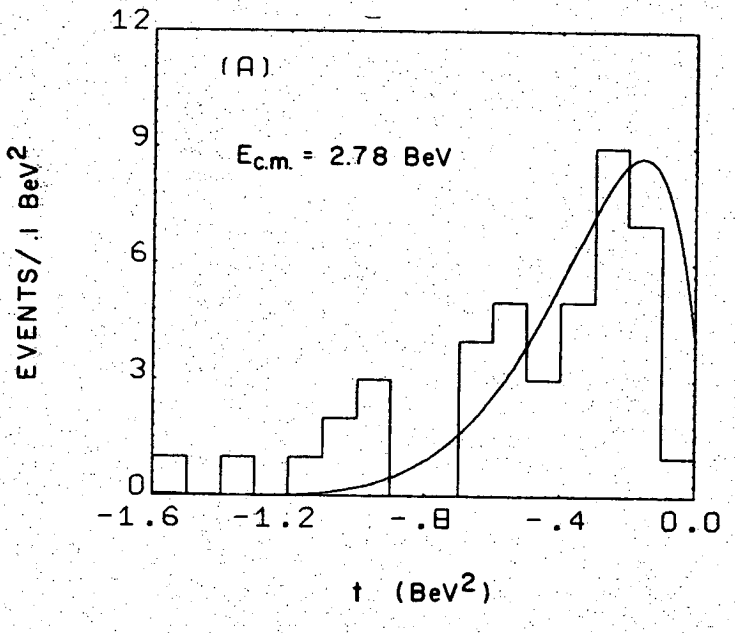

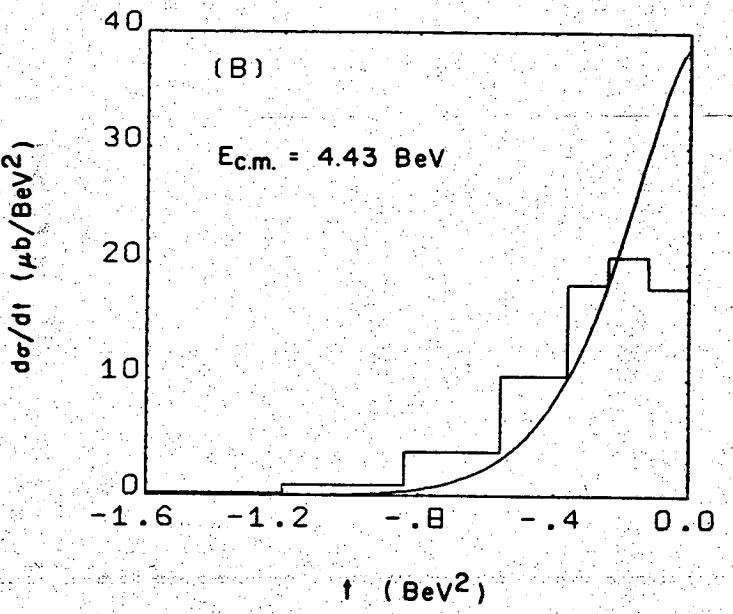

XBL 697-811

Figure 51. Differential cross section for a) $\pi^+ n \to \eta p$ from Benson, Ph. D. thesis, University of Michigan (1966), and b) $\pi^- p \to \eta n$ from Wahlig and Mannelli, PR 168, 1515 (1968). The curves are the predictions of the Reggeized A_2-exchange model with $b_o/a_o = 2.4$ and are normalized to have the same area as the histograms.

of reference 47 shown in Figure 50b. Figure 51b is the differential cross section for reaction (V.9) determined by Wahlig and Mannelli[46] at $E_{c.m.} = 4.43$ BeV. The distribution is somewhat broader than the model predicts; in this connection it is noted that the equivalent distribution of reference 47 seen in Figure 50d is narrower than that of Wahlig and Mannelli and more in agreement with the model, although both of these sources obtain the same total cross section.

At the lower end of the energy spectrum Richards et al.[44] have measured differential cross sections for reaction (V.9) which are in excellent agreement with those of this report at the energy values where they overlap. Only in the differential cross section measurements of this reference around $E_{c.m.} = 1.55$ BeV, the mass value of the $N_{\frac{1}{2}}(1550)$ resonance,[26] do the data differ markedly from the predictions of the Reggeized A_2-exchange model.

The simple two-parameter Regge exchange model described here is thus sufficient to describe accurately both the production angular distributions and the total cross section for reaction (IV.6a) over a wide range of energies; this indicates that the t-channel process of A_2-exchange dominates the reaction from near threshold up to the highest energy for which data are available.

Reference 64 is a list of other (less comprehensive) Regge fits to this reaction, using different parametrizations.

VI. ω PRODUCTION AND DECAY IN THE REACTION $\pi^+ n \to \omega p$

The $\pi^+\pi^-\pi^o$ decay mode of the ω is the only one considered in this report, and an ω event is one for which

$$750 \text{ MeV}/c^2 < m(\pi^+\pi^-\pi^o) < 820 \text{ MeV}/c^2.$$

Only those events are used which satisfy the "goodness" requirements of Section II and have proton spectator momentum less than 300 MeV/c. About 3100 such events lie in the ω mass band defined above; the background fraction in this cut is estimated to be 17 per cent. The reader is reminded that the cross section for ω production as a function of c.m. energy is given in Section IV.

A. The ω Decay Dalitz Plot

The Dalitz plot for the 3-pion decay of 3116 ω band events is shown in Figure 52. T_+, T_-, and T_o are the kinetic energies in the ω rest frame of the π^+, π^-, and π^o, respectively. The prominent feature of this Dalitz plot is the concentration of events near the center and the paucity of events near the boundary. This characteristic distribution of events in the Dalitz plot was used to determine the spin-parity of the ω as 1^- in the analysis of the experiment in which this meson was discovered and all its quantum numbers determined.[65] Since then Flatté et al.[66] have made a thorough analysis of over 4600 3-pion ω decays and also conclude that the spin-parity of the ω is 1^-. The simplest matrix element for the decay of a 1^- particle into $\pi^+\pi^-\pi^o$ is $\vec{p}_+ \times \vec{p}_-$, where $\vec{p}_+$ and $\vec{p}_-$ are the momentum vectors of the π^+ and the π^- in the 3-pion rest frame.[67] The square of this matrix element is displayed on the Dalitz plot of Figure 53. The

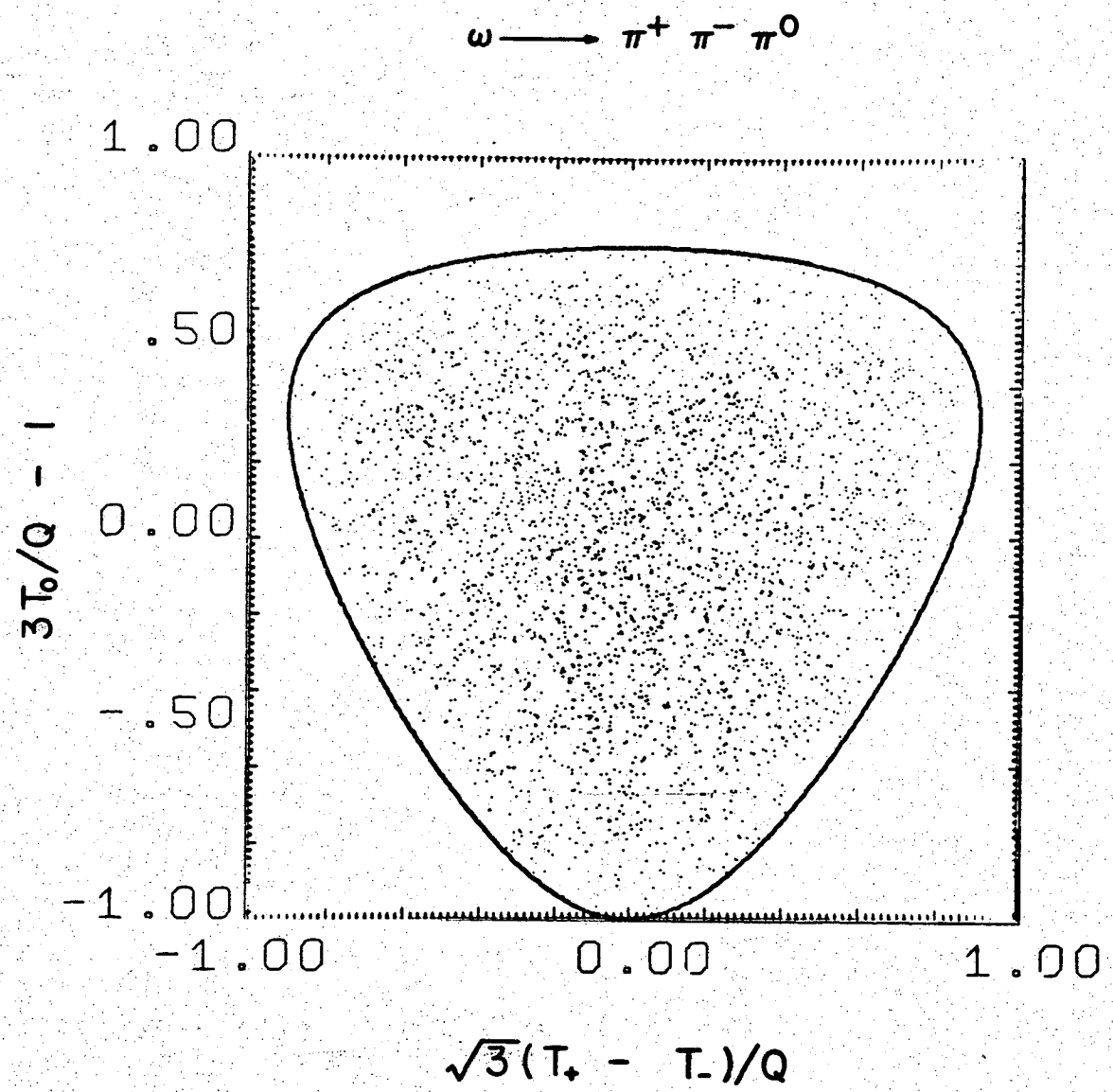

Figure 52. Dalitz plot of 3110 events in the ω band (750 MeV/c^2 < m(3π) < 820 MeV/c^2).

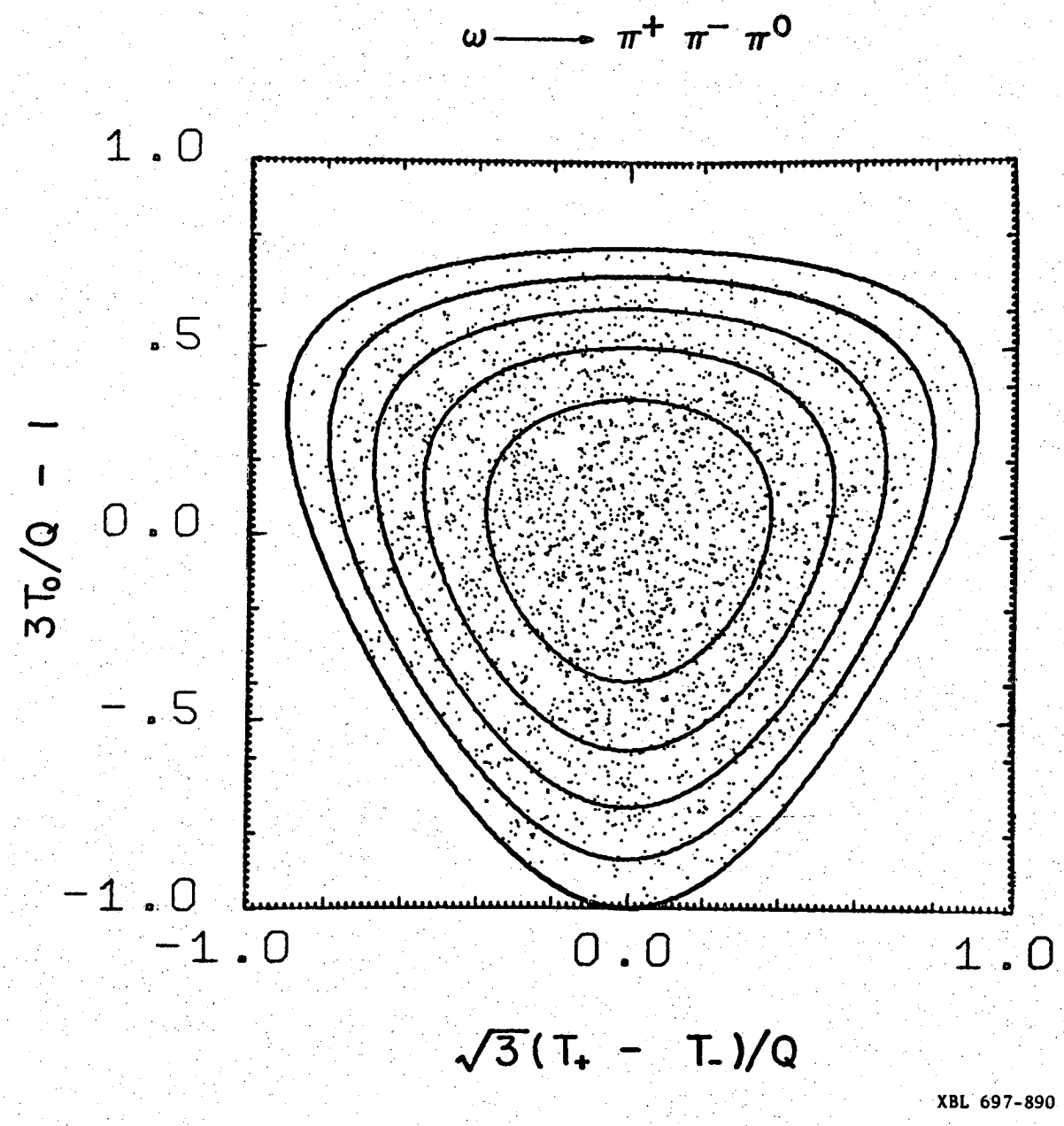

Figure 53. Dalitz plot of 3116 events in the ω band (750 MeV/c^2 < $m(3\pi)$ < 820 MeV/c^2); the curves are lines of constant probability for the decay of a 1^- particle.

contours are lines of constant intensity; the center of the Dalitz plot has maximum probability, and the boundary is the contour of zero probability.

The fractional left-right asymmetry of the events on the ω Dalitz plot in this report is

$$A = (R - L)/(R + L) = -.024 \pm .018$$

The significance of an asymmetry in the decay $\eta \to \pi^+\pi^-\pi^o$ has been discussed in the previous section.

B. Production Angular Distributions for $\pi^+ n \to \omega p$

The production angle is the angle between the π^+ beam and the final-state $\pi^+\pi^-\pi^o$ momentum vector, in the initial-state $\pi^+ n$ rest frame.

Production cosine distributions were obtained for six 100 MeV-wide c.m. energy intervals centered at $E_{c.m.}$ = 1.8, 1.9, ..., 2.3 BeV; the intervals contain between 200 and 750 events each. Using the Gaussian widths of the ω signals in these intervals (see Table 5), estimates have been made of the background fraction in the ω mass cut for each interval of c.m. energy. The background estimates for the intervals centered at $E_{c.m.}$ = 1.8, 1.9, 2.0, 2.1, 2.2, and 2.3 BeV are .18, .17, .20, .16, .11, and .14, respectively. The shape of the background production cosine distribution was presumed to be the same as that for 3-pion combinations with masses above and below the ω mass. The sum of production cosine distributions for 3-pion masses above (830 MeV/c^2 < m(3π) < 930 MeV/c^2) and below (640 MeV/c^2 < m(3π) < 740 MeV/c^2) the ω mass was found to be forward-peaked at all

c.m. energies except at 1.8 BeV. The shape of the production cosine distribution for these 3-pion mass cuts is well approximated by the function

$$b(\cos\theta) = 1 + h\, e^{-(1-\cos\theta)/.25}, \qquad \text{(VI.1)}$$

where h varied between 1 and 5 (except h = 0 at 1.8 BeV). A background with this shape was subtracted from each production cosine distribution in the amount given by the fractions stated above.

Figure 54 gives the ω production distributions for six 100 MeV-wide c.m. energy intervals after subtraction of the estimated background. The shaded area in the forwardmost two bins is the estimated number of events suppressed at low momentum transfer by the Pauli exclusion principle. A discussion of this effect is given in Section III. The fact that the production cosine distributions at the three highest energies have a somewhat flat forward peak suggests that the spin-flip as well as the non-spin-flip amplitude contributes. It was thus decided to take the <u>average</u> of the spin-flip and non-spin-flip Pauli suppression factors of Table 4a in making an upward correction to the two forwardmost production cosine bins at each energy. Table 10 shows $(-t)_{\text{minimum}}$ and $(-t)_{\text{maximum}}$ for this reaction at a number of c.m. energy values so that the t-distributions can be estimated.

C. <u>Decay Angular Distributions for $\omega \to \pi^+\pi^-\pi^o$</u>

The decay of ω mesons from the reaction $\pi^+ n \to \omega p$ will be described in the rest frame of the ω. The decay direction is the direction of the normal to the plane of the three decay pions. ω decay correlation data will be given for two reference frames.

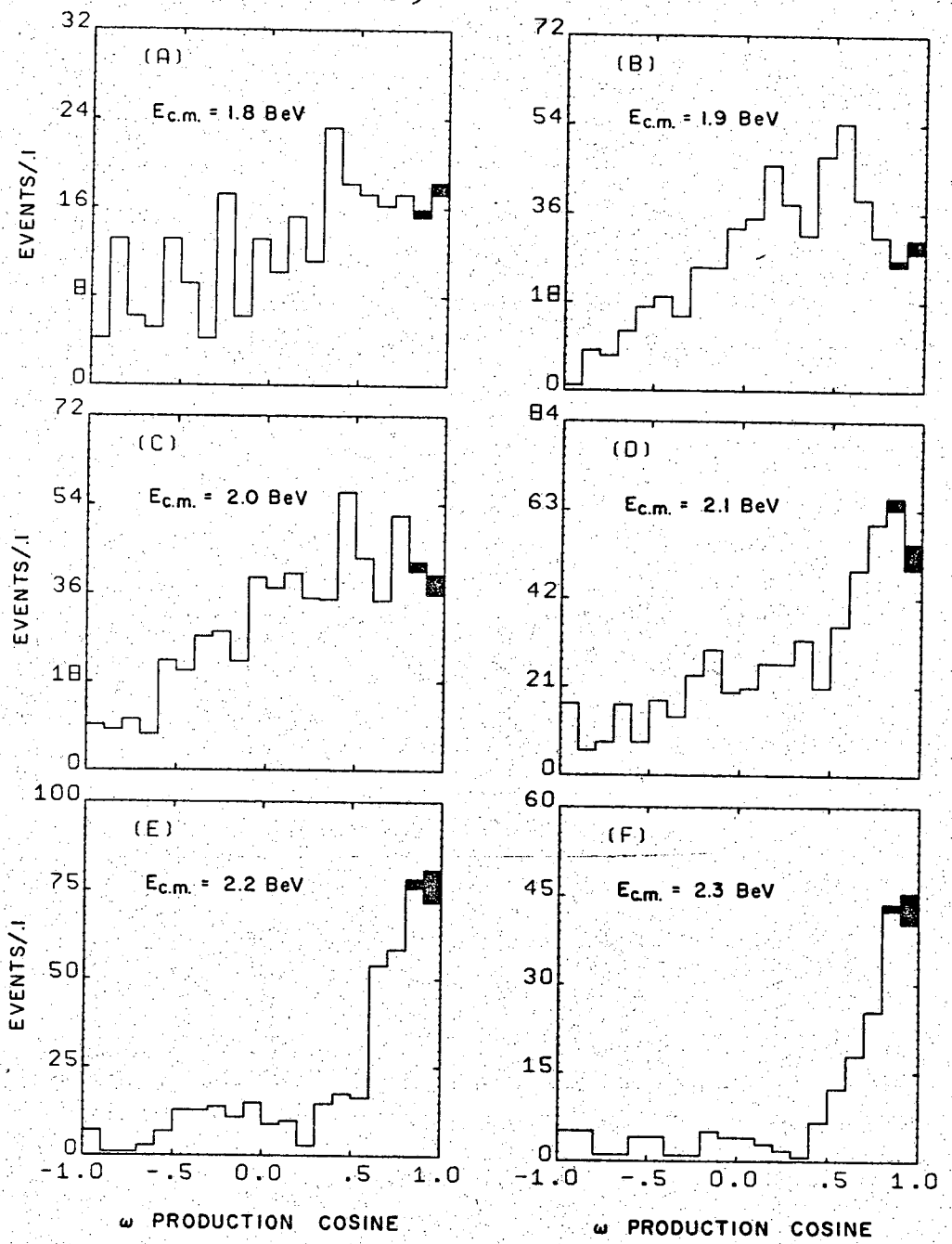

Figure 54. ω production cosine distributions for six 100 MeV-wide c.m. energy intervals. The shaded events are added to account for the effect of the Pauli exclusion principle.

Table 10. Limits on momentum-transfer-squared as a function of c.m. energy for the reaction $\pi^+ n \rightarrow \omega p$.

$E_{c.m.}$ (BeV)	$(-t)_{min.}$ (BeV^2)	$(-t)_{max.}$ (BeV^2)
1.75	.183	.555
1.80	.121	.790
1.85	.091	.999
1.90	.071	1.203
1.95	.058	1.406
2.00	.048	1.610
2.05	.041	1.817
2.10	.035	2.028
2.15	.030	2.243
2.20	.026	2.462
2.25	.023	2.686
2.30	.020	2.914
2.35	.018	3.147

a) Jackson frame:[69b]

Here the axes in the ω rest frame are defined as follows.

$\vec{z}$ = direction of incoming beam

$\vec{y}$ = normal to production plane

$\vec{x}$ = $\vec{y} \times \vec{z}$

b) helicity frame:

The axes in the ω rest frame are

$\vec{z}$ = direction of flight of the ω

$\vec{y}$ = normal to the production plane

$\vec{x}$ = $\vec{y} \times \vec{z}$

In both definitions it is important to note that the normal to the production plane is taken to be $\vec{b} \times \vec{\omega}$, where $\vec{b}$ is the 3-momentum of the incident beam and $\vec{\omega}$ is that of the outgoing ω meson.

The distribution of the normal to the 3-pion plane in these two frames is given by[68]

$$W(\theta,\varphi) = \frac{3}{4\pi}\Big[\ \rho_{0,0}\cos^2\theta + \frac{1}{2}(1 - \rho_{0,0})\sin^2\theta - \rho_{1,-1}\sin^2\theta\cos 2\varphi - \sqrt{2}\,\mathrm{Re}(\rho_{1,0})\sin 2\theta\cos\varphi\Big] \quad \text{(VI.2)}$$

Here $\rho_{i,j}$ are the components of the ω spin density matrix; a discussion of the density matrix of a spin-1 particle is given in Appendix F, which also contains an exposition of the method used here to find the density matrix.

The method of moments was used to determine the values of the density matrix elements. If the fraction of ω events in the ω mass cut is f, then under the assumption that the background events in the cut produce no decay correlations of the form given in equation (VI.2),

the density matrix elements are given by

$$\rho_{0,0} = \frac{1}{3} + \frac{1}{3}\sqrt{\frac{5}{4\pi}}\, a_{20}/f \qquad \text{(VI.3a)}$$

$$\rho_{1,-1} = -\frac{1}{12}\sqrt{\frac{30}{4\pi}}\, a_{22}/f \qquad \text{(VI.3b)}$$

$$\mathrm{Re}(\rho_{1,0}) = \frac{1}{12}\sqrt{\frac{15}{4\pi}}\, a_{21}/f \qquad \text{(VI.3c)}$$

Here

$$a_{20} = \langle Y_2^0(\theta,\varphi)\rangle = \langle\sqrt{\frac{5}{4\pi}}\,(\frac{3}{2}\cos^2\theta - \frac{1}{2})\rangle \qquad \text{(VI.4a)}$$

$$a_{21} = 2\langle \mathrm{Re}(Y_2^1(\theta,\varphi))\rangle = 2\langle -\sqrt{\frac{15}{8\pi}}\,\sin\theta\cos\theta\cos\varphi\rangle \qquad \text{(VI.4b)}$$

$$a_{22} = 2\langle \mathrm{Re}(Y_2^2(\theta,\varphi))\rangle = 2\langle \frac{1}{4}\sqrt{\frac{15}{2\pi}}\,\sin^2\theta\cos 2\varphi\rangle, \qquad \text{(VI.4c)}$$

where the Y_ℓ^m are the spherical harmonics (see Appendix F).

At each c.m. energy the events were divided into production cosine intervals such that each interval contained about 100 resonance events. In each production cosine interval the maximum-likelihood fitting program MURTLEBERT[37] was used to estimate the fraction of ω events; the fit was performed leaving the ω mass and width to be found as well as its fraction. The assumption that only the ω events (and not the background) contribute to the moments of Y_2^0, $\mathrm{Re}(Y_2^1)$, and $\mathrm{Re}(Y_2^2)$ was strengthened by taking moments in the nonresonant mass band 830 MeV/c^2 < $m(3\pi)$ < 930 MeV/c^2 for each c.m. energy interval and noting that these moments are essentially statistically zero. Since only ω events and background events, whose 3-pion "decay" should be isotropic, are assumed to be present in the ω mass cut, only the three moments listed above should be nonvanishing. To check this prediction, <u>all</u> the moments of Y_ℓ^0, $\mathrm{Re}(Y_\ell^m)$, and $\mathrm{Im}(Y_\ell^m)$ for ℓ = 1, 2, 3 were calculated, and it was seen that essentially all moments, except

the allowed ones, are zero in the ω band.

An independent check on the method was supplied by a series of maximum-likelihood fits, in which the decay correlation coefficients a_{20}, a_{21}, and a_{22} were included in addition to the ω amount, mass, and width. In a few production cosine intervals no solution could be obtained, since a few events yielded negative likelihoods, but in all cases where a solution was found, the coefficients were in excellent agreement with those determined from the moments analysis.

The density matrix elements quoted in this report are the ones found from the moments analysis.

Table 11 gives the density matrix elements in the Jackson frame found as described above, and in Table 12 are found those in the helicity frame. The errors take into account the uncertainty in the coefficients a_{20}, a_{21}, and a_{22} as well as that in the ω fraction. Figures 55, 56, and 57 show the density matrix elements $\rho_{0,0}$, $\rho_{1,-1}$, and $\mathrm{Re}(\rho_{1,0})$, respectively, in the Jackson frame. The curves in these figures will be discussed below. Figures 58, 59, and 60 display these density matrix elements in the helicity frame.

It is noted that the density matrix values in the Jackson frame for $E_{c.m.} = 2.0$ BeV agree well with the equivalent values given by Bacon *et al.*[18c] averaged over all production cosine. The Jackson frame values of $\rho_{0,0}$ are also similar to those found by Miller *et al.*,[12] Cohn *et al.*,[20c] and Benson[21d, 21e] at higher energies: typically $\rho_{0,0} \cong .5$, which implies a $1 + \cos^2\theta$ decay cosine distribution.

Table 11. ω decay density matrix elements in the Jackson frame as a function of c.m. energy and production cosine interval.

$E_{c.m.}$ (BeV)	$\cos\theta$	$\rho_{0,0}$	$\rho_{1,-1}$	$Re(\rho_{1,0})$
1.8	(-1.,0.)	.53 ± .12	-.05 ± .08	.12 ± .08
	(0.,.5)	.60 ± .14	-.04 ± .09	-.05 ± .08
	(.5,1.)	.49 ± .13	.07 ± .10	-.08 ± .08
1.9	(-1.,-.3)	.62 ± .18	-.06 ± .10	-.01 ± .08
	(-.3,.1)	.61 ± .11	-.19 ± .08	-.07 ± .06
	(.1,.4)	.58 ± .11	.01 ± .07	-.10 ± .06
	(.4,.7)	.63 ± .11	.09 ± .07	-.16 ± .06
	(.7,1.)	.33 ± .11	-.06 ± .10	-.06 ± .08
2.0	(-1.,-.3)	.52 ± .13	.00 ± .08	-.06 ± .07
	(-.3,.1)	.80 ± .13	-.08 ± .07	-.15 ± .07
	(.1,.4)	.53 ± .10	-.03 ± .07	-.24 ± .08
	(.4,.7)	.51 ± .10	-.03 ± .07	-.21 ± .06
	(.7,1.)	.31 ± .09	.04 ± .07	-.18 ± .06
2.1	(-1.,-.2)	.40 ± .10	-.12 ± .09	-.16 ± .08
	(-.2,.2)	.55 ± .11	-.09 ± .08	-.16 ± .07
	(.2,.6)	.37 ± .09	.05 ± .08	-.21 ± .07
	(.6,.8)	.20 ± .08	.07 ± .09	-.17 ± .06
	(.8,1.)	.42 ± .09	.08 ± .08	-.05 ± .06
2.2	(-1.,0.)	.30 ± .11	-.29 ± .13	-.16 ± .09
	(0.,.6)	.34 ± .11	-.09 ± .10	-.27 ± .09
	(.6,.85)	.27 ± .08	.09 ± .07	-.12 ± .05
	(.85,1.)	.49 ± .09	-.11 ± .07	-.01 ± .05
2.3	(-1.,.7)	.42 ± .12	-.11 ± .10	-.16 ± .09
	(.7,1.)	.49 ± .10	.08 ± .07	-.16 ± .06

Table 12. ω decay density matrix elements in the helicity frame as a function of c.m. energy and production cosine interval.

$E_{c.m.}$ (BeV)	cosθ	$\rho_{0,0}$	$\rho_{1,-1}$	$Re(\rho_{1,0})$
1.8	(-1.,0.)	.53 ± .13	-.04 ± .08	-.07 ± .07
	(0.,.5)	.23 ± .12	-.22 ± .12	.01 ± .08
	(.5,1.)	.40 ± .12	.03 ± .10	.12 ± .08
1.9	(-1.,-.3)	.46 ± .15	-.14 ± .12	-.11 ± .09
	(-.3,.1)	.36 ± .09	-.31 ± .09	-.03 ± .05
	(.1,.4)	.18 ± .09	-.20 ± .09	.02 ± .06
	(.4,.7)	.15 ± .09	-.15 ± .08	.18 ± .06
	(.7,1.)	.43 ± .13	.00 ± .09	.07 ± .08
2.0	(-1.,-.3)	.38 ± .11	-.07 ± .09	-.08 ± .07
	(-.3,.1)	.23 ± .09	-.36 ± .10	-.17 ± .07
	(.1,.4)	.08 ± .10	-.26 ± .10	.13 ± .07
	(.4,.7)	.29 ± .08	-.14 ± .08	.20 ± .06
	(.7,1.)	.60 ± .11	.19 ± .08	.07 ± .06
2.1	(-1.,-.2)	.15 ± .10	-.24 ± .11	-.06 ± .07
	(-.2,.2)	.20 ± .09	-.26 ± .10	-.05 ± .06
	(.2,.6)	.12 ± .10	-.07 ± .08	.16 ± .06
	(.6,.8)	.42 ± .10	.18 ± .08	.15 ± .06
	(.8,1.)	.43 ± .09	.08 ± .08	.12 ± .07
2.2	(-1.,0.)	.17 ± .13	-.36 ± .14	.01 ± .07
	(0.,.6)	.13 ± .12	-.19 ± .12	.15 ± .09
	(.6,.85)	.33 ± .07	.12 ± .07	.10 ± .05
	(.85,1.)	.45 ± .09	-.13 ± .08	.04 ± .06
2.3	(-1.,.7)	.30 ± .11	-.18 ± .12	.09 ± .08
	(.7,1.)	.43 ± .10	.05 ± .07	.15 ± .06

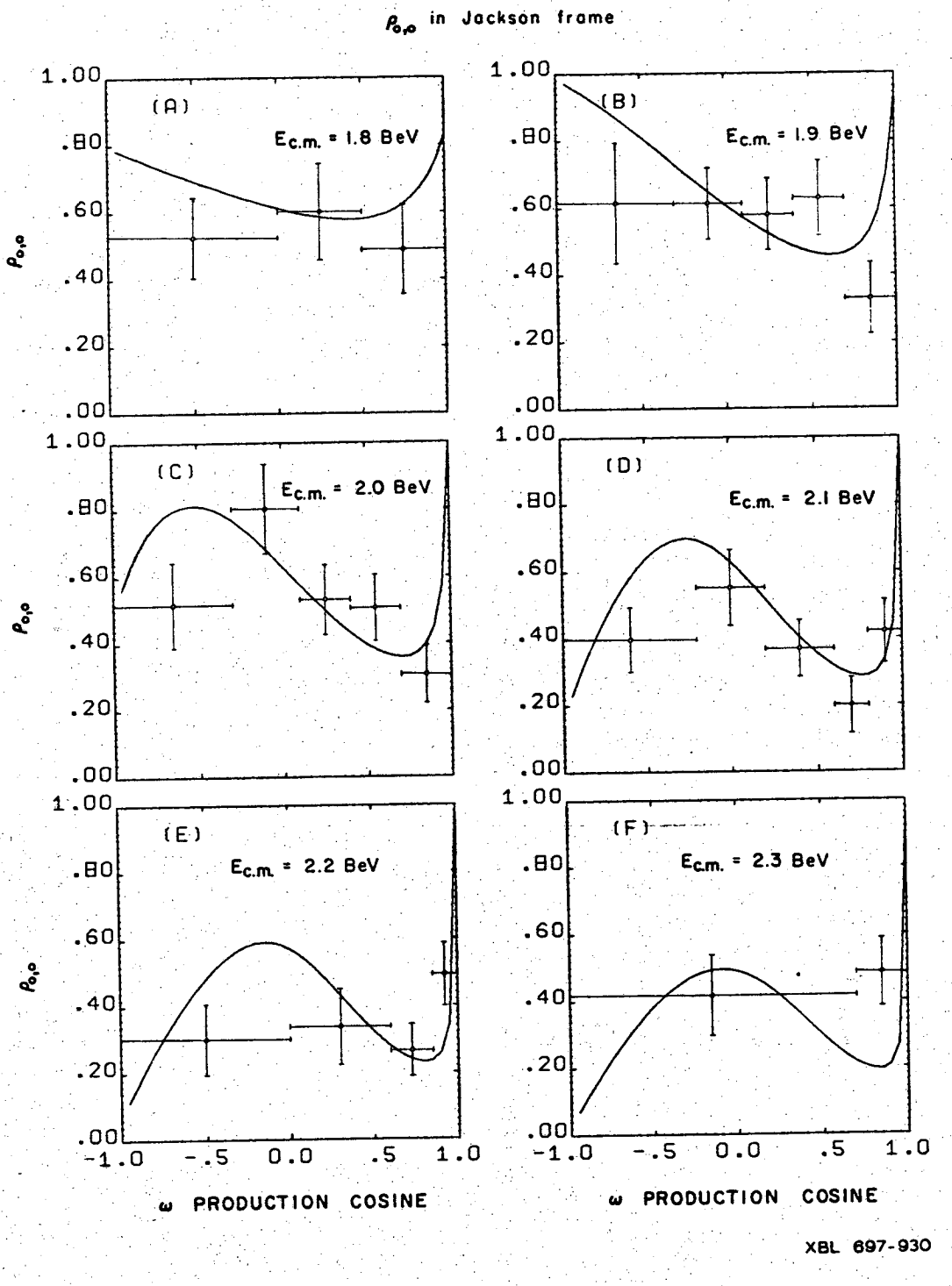

Figure 55. $\rho_{0,0}$ for ω decay in the Jackson frame; the curves are the predictions of the ρ-exchange model with absorption for $G_T = G_V$.

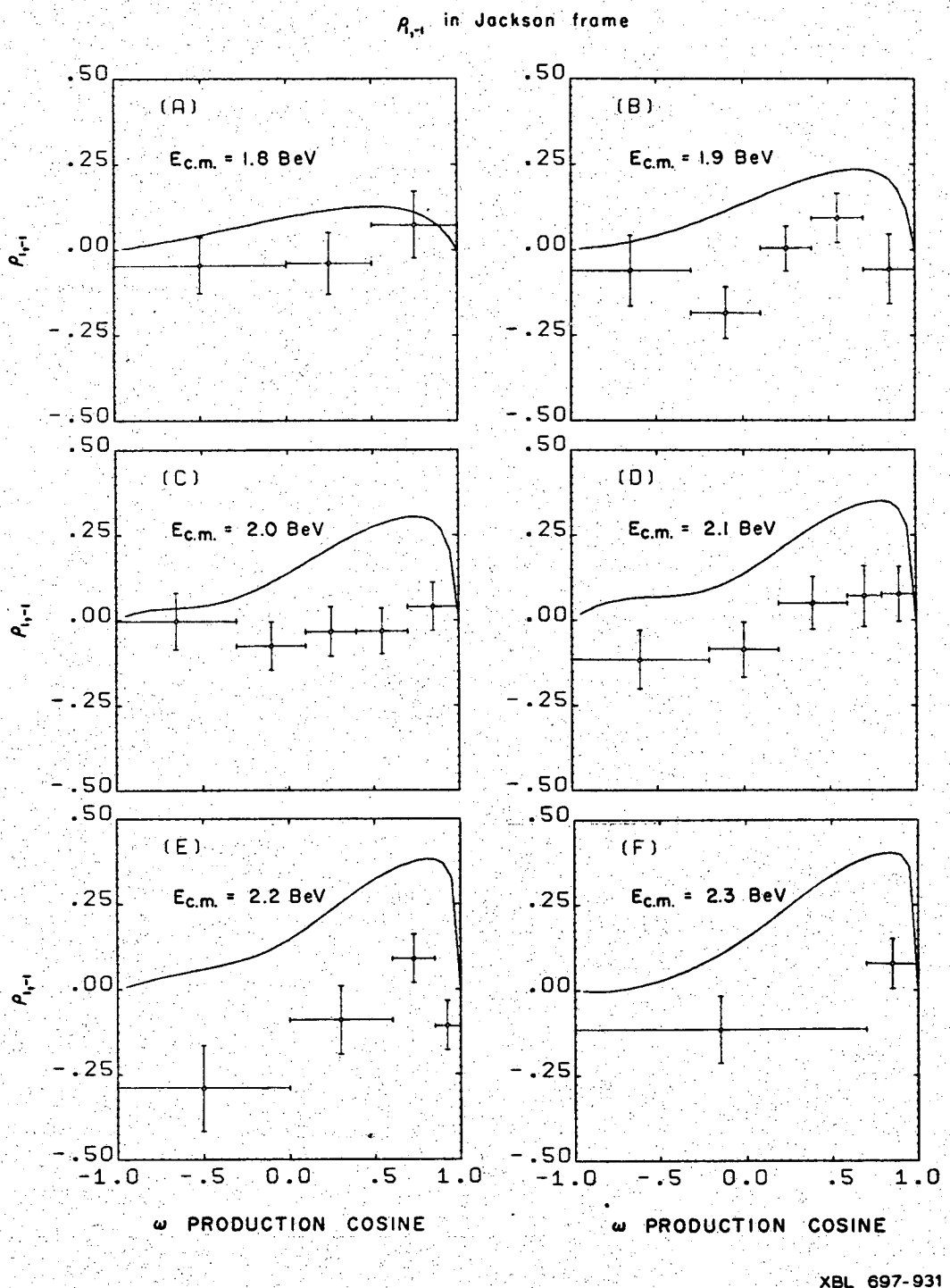

Figure xx. $\rho_{1,-1}$ for ω decay in the Jackson frame; the curves are the predictions of the ρ-exchange model with absorption for $G_T = G_V$.

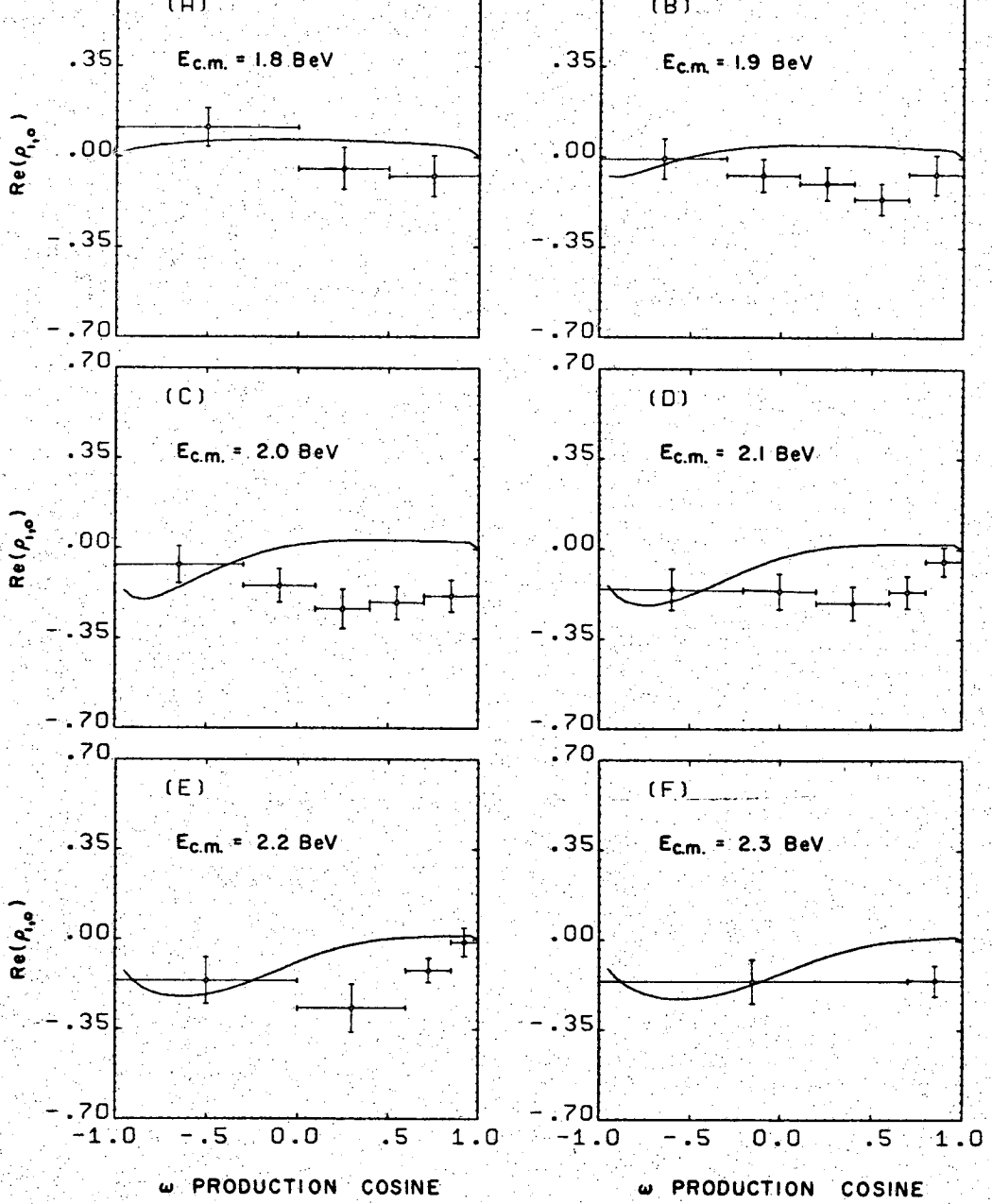

Figure 57. $Re(\rho_{1,0})$ for ω decay in the Jackson frame; the curves are the predictions of the ρ-exchange model with absorption for $G_T = G_V$.

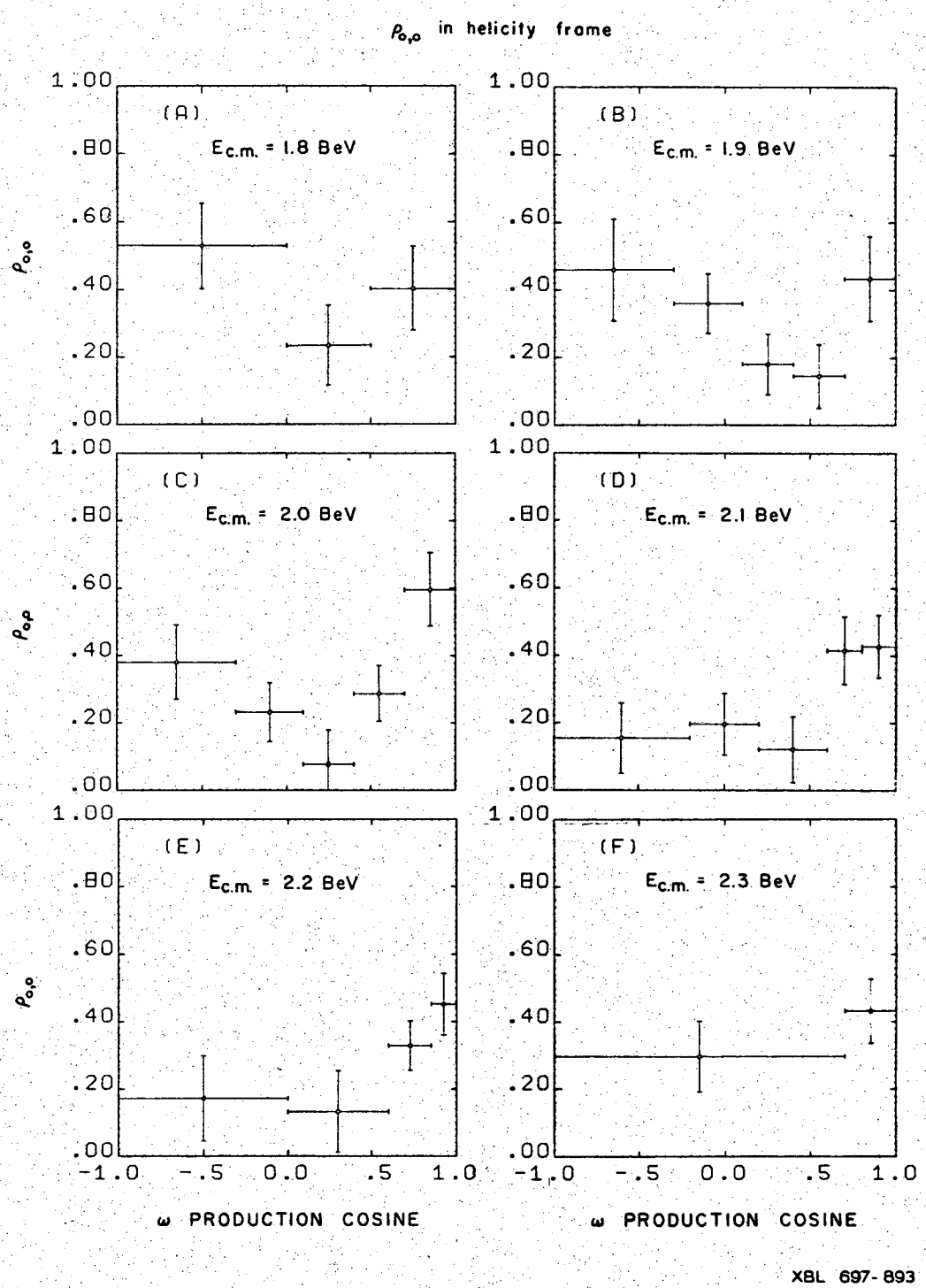

Figure 58. $\rho_{0,0}$ for ω decay in the helicity frame.

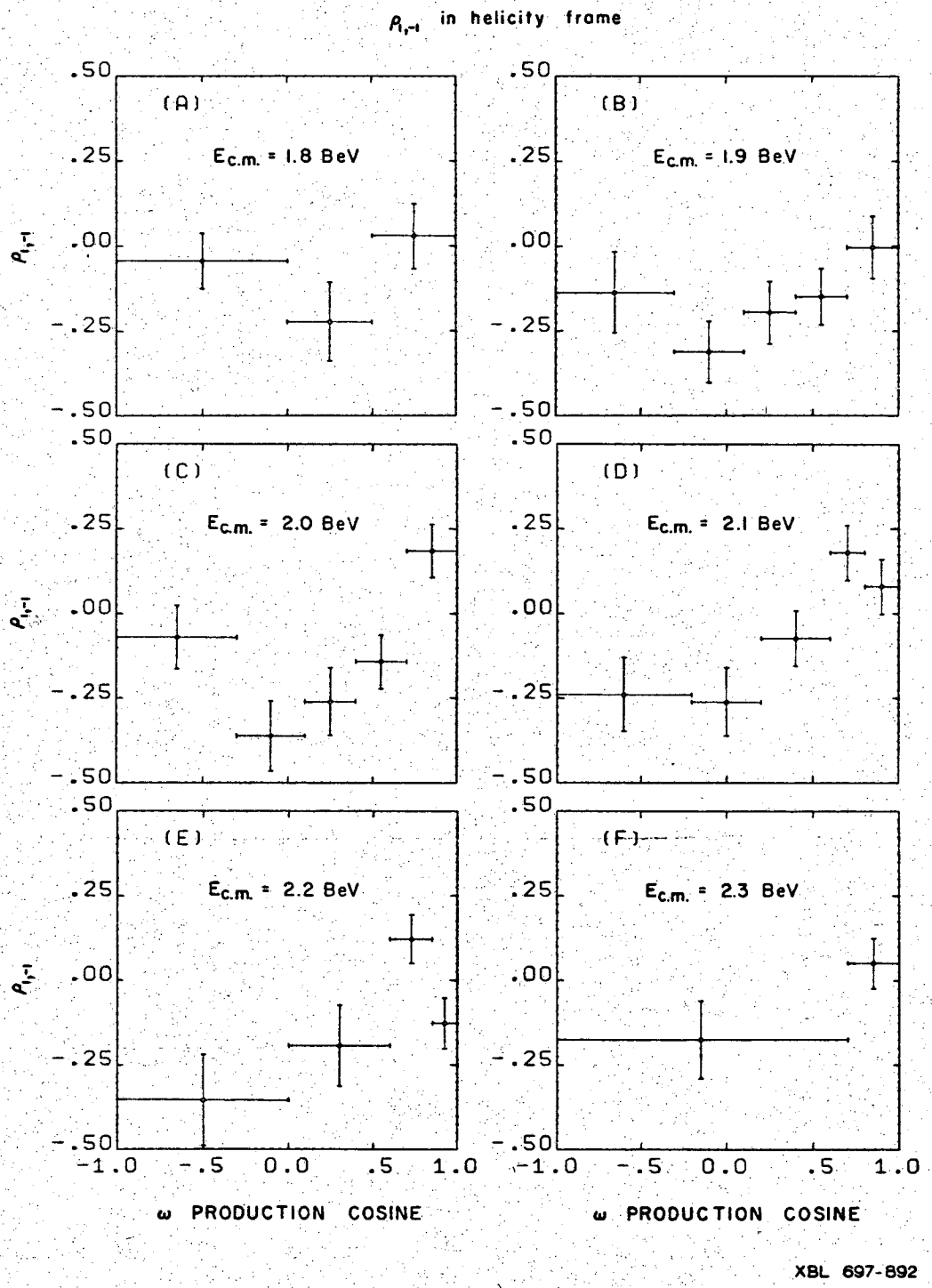

Figure 59. $\rho_{1,-1}$ for ω decay in the helicity frame.

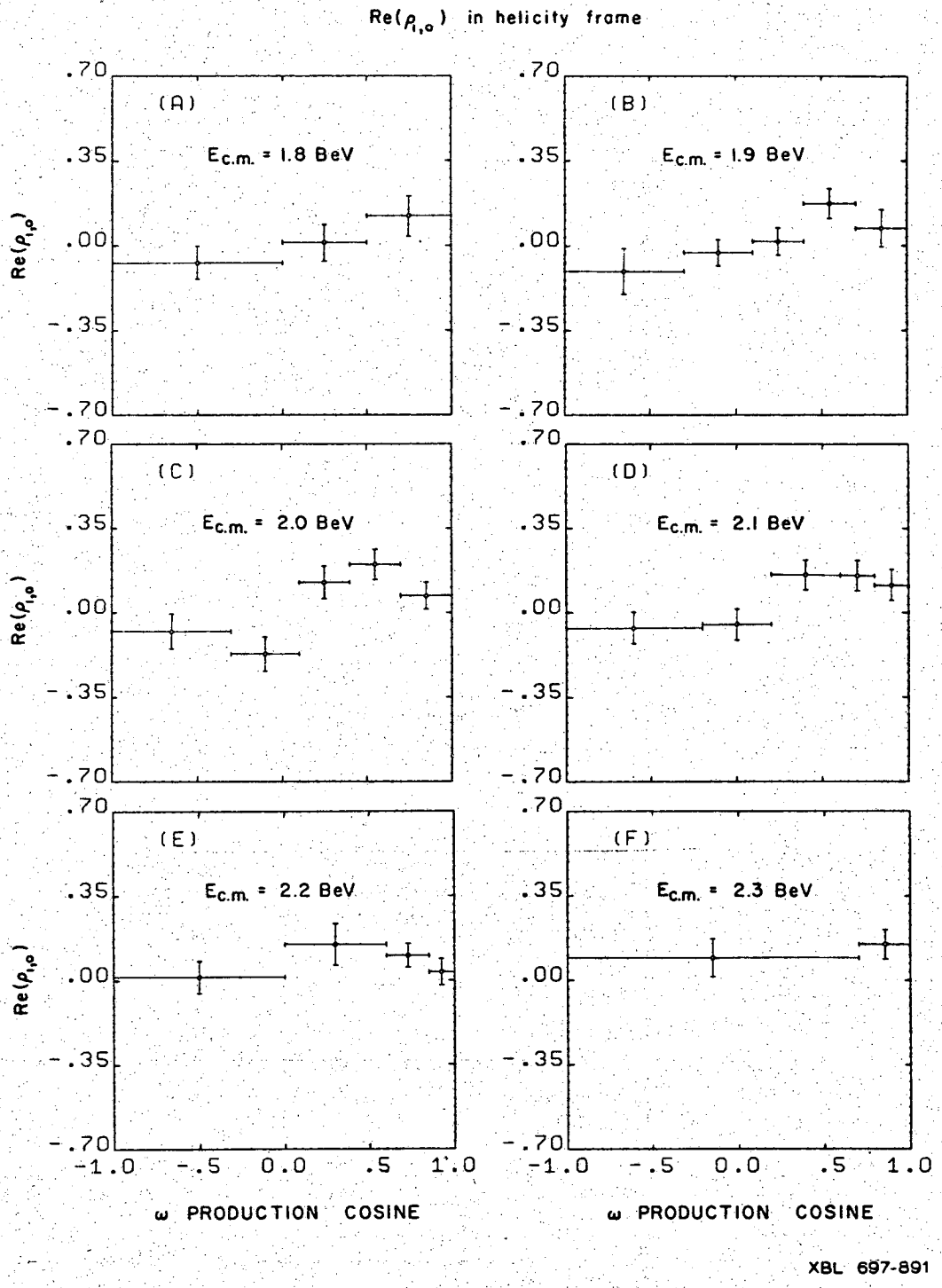

Figure 60. $Re(\rho_{1,0})$ for ω decay in the helicity frame.

D. An Attempt to Describe the Reaction $\pi^+ n \to \omega p$ Using a ρ-Exchange Model with Absorption

The forward peaking of the production cosine distributions of Figure 54 at the higher c.m. energies suggests that in this energy region, say for $E_{c.m.} > 1.9$ BeV, a description of the production process might be obtained in terms of particle or Regge-pole exchange. Figure 61a shows such an exchange diagram in which the exchanged particle is the ρ meson. In fact, the upper vertex of the figure shows that the exchanged meson must have I = 1, and of the four I = 1 possibilities (π, ρ, A_2, B), π and A_2 have the incorrect G-parity. The ρ meson has a lower mass than the B meson and might at first consideration be expected to contribute more than the B.

The postulate of ρ-exchange as shown in Figure 61a leads to the conclusion that

$$\rho_{0,0} = \mathrm{Re}(\rho_{1,0}) = 0 \qquad \text{(VI.5)}$$

in the Jackson frame. This can be seen easily as follows: In the Jackson frame the ω is at rest, and a ρ and a π^+ (the beam) come together from opposite directions along the z-axis to form the ω. The π^+ has $J^P = 0^-$, the ρ has $J^P = 1^-$, and the ω has $J^P = 1^-$, so to satisfy spin and parity conservation the ρ and π^+ must be in a relative P-wave. Now because the ρ-π^+ relative angular momentum has no component along their line of flight (the z-axis), the P-wave angular momentum function must be Y_1^0 in the Jackson frame. This angular momentum is added to the ρ spin wave function to form the ω spin. But since Y_1^0, the ρ, and the ω all have spin 1, only the ± 1 substates of

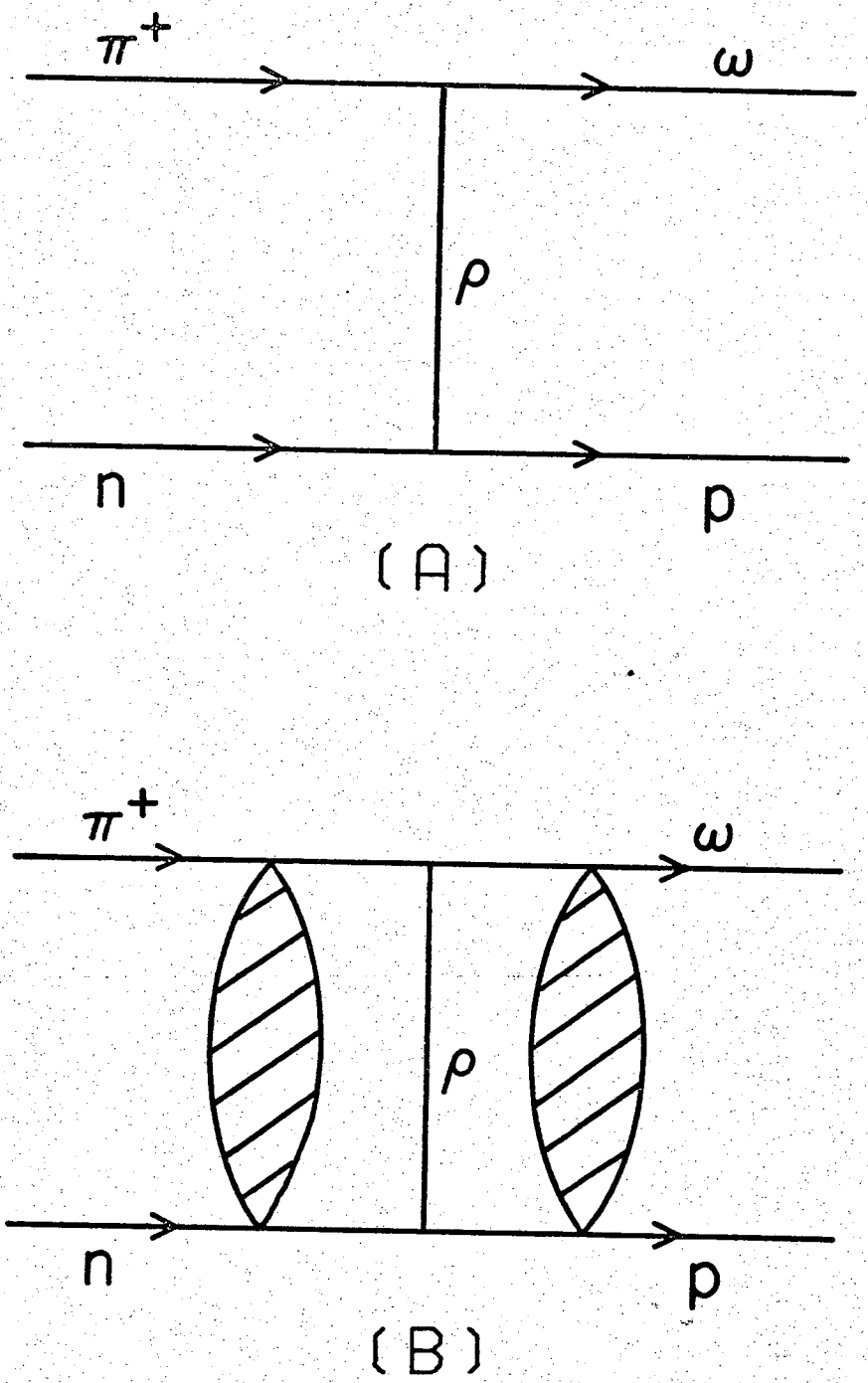

XBL 697-889

Figure 61. a) ρ-exchange diagram as a mechanism for $\pi^+ n \rightarrow \omega p$;
b) ρ-exchange diagram with absorption as a mechanism for $\pi^+ n \rightarrow \omega p$.

the ω can be populated. (The m = 0 spin substate of the ρ, when added as an angular momentum with Y_1^0, does not couple to spin 1.) The fact that no m = 0 substates of the ω are populated then implies equation (VI.5).

It is clear from the nonvanishing values of $\rho_{0,0}$ in the Jackson frame in this and other experiments that the simple ρ-exchange process discussed above does not agree with the data. A way around the difficulty is the inclusion of absorptive corrections, that is, the inclusion of diffractive scattering of the initial- and final-state particles along with the ρ-exchange. This situation is drawn in Figure 61b. J. D. Jackson and his coworkers have developed a theory of particle exchange, including the effects of absorption; reference 69 is a list of papers expounding the theory and summarizing its comparisons with many experiments. The initial- and final-state absorption (diffractive scattering) not only change the value of $\rho_{0,0}$ from that expected according to simple ρ-exchange, but also predict production angular distributions narrower than those predicted by the ρ propagator factor alone.

In essence, the two diffraction scattering processes indicated in Figure 61b each contribute to the overall process with a phase shift $\delta(\ell)$ given by

$$e^{2i\delta(\ell)} = 1 - C\, e^{-\gamma \ell^2}, \qquad \text{(VI.6)}$$

where, by analogy with diffraction scattering on a "gray" disc, C gives the "darkness" of the disc (C = 1 means an opaque disc, C = 0 means no disc at all); and $\gamma = 2/k^2R^2$, where k is the particle momen-

tum, R is the radius of the diffracting disc, and ℓ is the angular momentum. The parameters γ and C are known for the initial-state scattering ($\pi^+ n$ scattering in our example), and for the final-state scattering the standard choice[69f] of parameters is C = 1, and $\gamma_{final} = .75\ \gamma_{initial}$.

A fit to the reaction $\pi^+ n \rightarrow \omega p$ at our c.m. energies using a ρ-exchange model with absorption has been attempted.[70] With the absorption parameters γ and C fixed as stated in the above paragraph, fits were tried for three values of the ratio G_T/G_V, the ratio of tensor to vector coupling at the ρnp vertex.[69c] The model was compared to the data of this report for G_T/G_V = 1, 2, and 3; at all of these values the agreement is in general poor, so that no more detailed fitting was attempted. Although vector meson dominance of the nucleon form factor predicts $G_T/G_V = 3.7$,[69c] this value was not tried since the agreement between the model and the data, where present, occurred for a ratio of 1.

The total cross section for this reaction cannot be described by the model, since the experimental cross section drops after reaching a peak near threshold (see Figure 43b), whereas the model predicts a cross section rising uniformly with energy from threshold. In order to ignore this basic discrepancy between experiment and the theory, the differential cross section curves predicted by the model have been normalized to have the same area as the histograms of Figure 62, which shows the differential cross section and the theoretical curves for $G_T/G_V = 1$. The curves agree with the experimental production distributions only for $E_{c.m.}$ 2.2 and 2.3 BeV. The curves in Figures

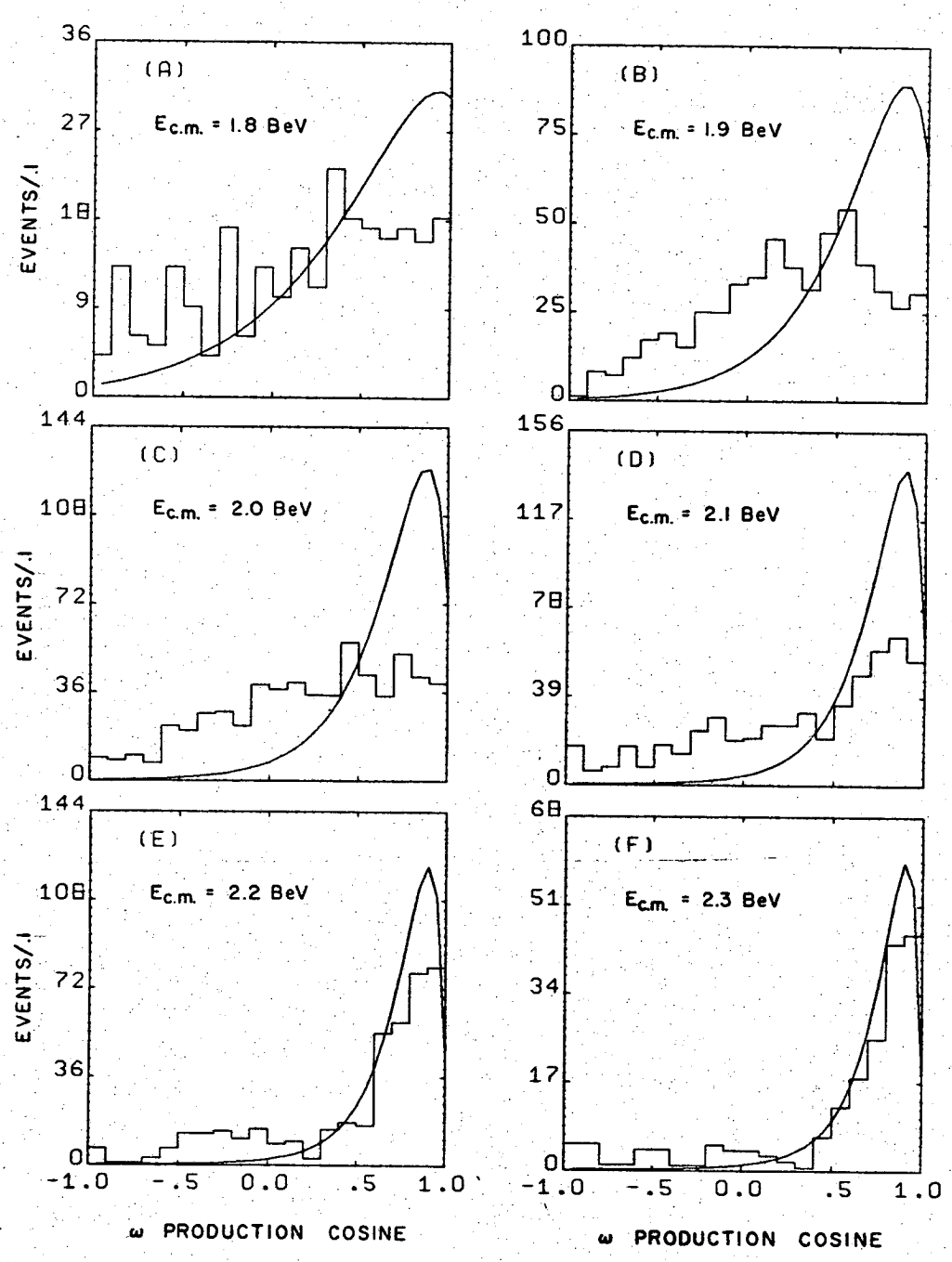

Figure 62. ω production cosine distributions for six 100 MeV-wide c.m. energy intervals. The shaded events are added to account for the effect of the Pauli exclusion principle. The curves are the predictions of the ρ-exchange model with absorption; they are normalized to have the same area as the histograms.

55, 56, and 57 show the predictions of the ρ-exchange model with absorption for the ω decay density matrix elements. The value $G_T/G_V = 1$ was selected for graphical comparison with the data primarily because it yields a fairly good fit to $\rho_{0,0}$. However, the agreement with $\rho_{1,-1}$ and $\mathrm{Re}(\rho_{1,0})$ is poor, as it is for the other values of G_T/G_V. Similar difficulties in comparing this ρ-exchange model with experiment have been met by other authors.[12, 18c, 20c, 21d]

An attempt to understand the reaction $\pi^+ n \to \omega p$ in terms of a Regge pole-exchange model involving both B and ρ trajectory exchanges has also been attempted by some authors,[12, 18c, 21d] with indifferent success.

APPENDIX A

DETERMINATION OF EXPOSURE SIZE

Three independent methods were used to determine the size of the exposure at the eight incident pion momentum settings p = 1.10 (1.119 ± .01119 and 1.086 ± .01086), 1.30 (1.301 ± .01301), 1.53 (1.525 ± .01525), 1.58 (1.584 ± .01584), 1.70 (1.704 ± .01704), 1.86 (1.856 ± .025 and 1.868 ± .01868), 2.15 (2.160 ± .0216 and 2.140 ± .0214), and 2.37 (2.360 ± .0445 and 2.384 ± .040) BeV/c. The numbers in parentheses are the values used in the beam momentum averaging.

Method 1. Direct Measurement of Path Length

In a special scan of the film, every 25th frame of 10 rolls of film at each incident momentum was scanned, noting the number of beam tracks entering the chamber (= N_o), the number leaving the end of the chamber without interacting (= N_e), the number leaving the sides of the chamber without interacting (= N_s), and the number having some interaction in the bubble chamber (= N_i). N_i is corrected for an estimated 10 per cent of 1-pronged events missed due to the fact that their scattering angles were too small to be detected. Then at each momentum a number of tracks leaving the end and a number leaving the sides of the chamber were measured on a Franckenstein measuring machine to determine their average lengths, ℓ_e and ℓ_s, respectively. Table A.1 gives the number of each type found in the scan, and their average lengths.

Since the interaction length ℓ_o in the bubble chamber is long ($\sigma_{tot} \sim 60$ mb, so $\ell_o \simeq$ (1 ft-b)/60 mb $\simeq$ 16 ft) compared to the length

Table A.1. Results of path length scan and track length measurement.

p (BeV/c)	N_o	N_i	N_s	ℓ_e* (cm)	ℓ_s+ (cm)
1.10	2 669	756	1 161	156.9	132.
1.30	2 522	780	374	153.6	130.
1.53	3 384	1 040	891	154.1	120.
1.58	3 237	972	929	154.8	131.
1.70	3 672	1 156	353	153.8	140.
1.86	3 493	1 044	179	153.5	135.
2.15	3 703	1 028	92	152.8	121.
2.37	3 076	802	89	151.9	106.

* The error in ℓ_e is typically 1 per cent.

+ The error in ℓ_s is typically 5 per cent.

of the bubble chamber ($\cong 6$ ft), the average length of tracks interacting in the bubble chamber will be taken to be $\ell_e/2$, or $\frac{1}{2}$ the effective length of the chamber; i.e. the beam is not appreciably attenuated in passing through the bubble chamber, and the interactions are distributed randomly along the length of the chamber. This can be calculated as follows, using the fact that the probability of interacting at a distance x is $-d(e^{-x/\ell_o})/dx = (e^{-x/\ell_o})/\ell_o$:

$$\langle \ell \rangle = \text{average length of interacting tracks}$$

$$= \frac{\int_o^{\ell_e} (x/\ell_o)\, e^{-x/\ell_o}\, dx}{\int_o^{\ell_e} (1/\ell_o)\, e^{-x/\ell_o}\, dx}$$

$$= \frac{\ell_e}{1 - e^{\ell_e/\ell_o}} + \ell_o$$

Since $\ell_o \gg \ell_e$, $e^{\ell_e/\ell_o} \cong 1 + \ell_e/\ell_o + (\ell_e/\ell_o)^2/2$,

$$\langle \ell \rangle \cong \frac{-\ell_o}{1 + \ell_e/2\ell_o} + \ell_o \cong \ell_e/2$$

The path length in the frames scanned is then

$$L = N_e\ell_e + N_s\ell_s + N_i\ell_e/2$$

$$= (N_o - N_i - N_s)\ell_e + N_s\ell_s + N_i\ell_e/2$$

$$= (N_o - N_i/2 - N_s)\ell_e + N_s\ell_s$$

Table A.2 gives the results of this calculation of the path length.

Method 2. Indirect Determination of the Path Length

In this method of estimating the total path length, the total $\pi^+ d$ cross section as measured elsewhere[34] with high precision is divided into the total number of events estimated to be on the film,

Table A.2. Results of direct measurement of path length.

p (BeV/c)	path length in scan (10^6 cm)	path length per roll (10^6 cm)	number of rolls	total path length (10^6 cm)	total path length (ev/μb)
1.10	.330	.825	16	13.20	.50
1.30	.319	.797	15	11.96	.45
1.53	.411	1.029	69	70.98	2.70
1.58	.404	1.009	13	13.12	.50
1.70	.471	1.177	68	81.24	3.09
1.86	.453	1.132	71	80.35	3.05
2.15	.484	1.211	70	84.78	3.22
2.37	.402	1.005	26	26.14	.99

using the relation

$$\text{path length (cm)} = L = 26.3 \cdot 10^6 \cdot (\text{total events})/\sigma_{tot}\ (\mu b).$$

Two procedures were used to estimate the total number of events on the film:

a) In a scan of every 25th frame of 10 rolls of film at each of the eight momentum settings, the total number of interactions were noted, as described in method 1. Extrapolating to the entire sample of film, the numbers given in Table A.3 were obtained for the size of the exposure.

b) Using the scan mentioned in a) above, the ratio of 3- and 4-pronged events to all events was computed. Then using the master scan list to get the total number of 3- and 4-pronged events found on the film, corrected upward by 5 per cent (the scan ineffiency for 3- and 4-pronged events estimated from a check scan), the total number of events on the film was estimated, and the exposure size was obtained as in a). Table A.4 gives a summary of the procedure and the results obtained.

Method 3. Indirect Determination of the Path Length

This method of estimating the total path length is similar to that of method 2, but instead of estimating the total number of events on the film and dividing this number by the total cross section, here we estimate the total number of events fitting the reactions

$$\begin{aligned} \pi^+ n\ (p) &\rightarrow (p)\ p\ \pi^+\ \pi^- \\ &\rightarrow (p)\ p\ \pi^+\ \pi^-\ \pi^o \\ &\rightarrow (p)\ p\ \pi^+\ \pi^-\ \gamma \end{aligned} \qquad \text{(A.1)}$$

Table A.3. Path length determination using π^+ d total cross section (method a)

p (BeV/c)	σ_{tot}^{34} (mb)	ev/μb
1.10	71.0	.42 ± .01
1.30	69.8	.43 ± .01
1.53	71.4	2.57 ± .07
1.58	69.6	.46 ± .01
1.70	66.5	2.97 ± .07
1.86	64.7	2.92 ± .06
2.15	63.8	2.88 ± .06
2.37	63.2	.84 ± .02

Table A.4. Path length determination using $\pi^+ d$ total cross section (method b)

p (BeV/c)	no. of 3-, 4-prongs	corrected* no. of 3-, 4-prongs	ratio of 3-, 4-prongs to all	total events	σ_{tot}^{34} (mb)	ev/μb
1.10	4 541	4 780	.145	32 966	71.0	.46
1.30	5 367	5 649	.186	30 371	69.8	.44
1.53	34 977	36 818	.204	180 480	71.4	2.53
1.58	6 385	6 721	.226	29 739	69.6	.43
1.70	43 111	45 380	.226	200 796	66.5	3.03
1.86	48 618	51 177	.271	188 845	64.7	2.92
2.15	59 301	62 422	.317	196 915	63.8	3.09
2.37	18 401	19 369	.364	53 212	63.2	.84

* The correction is for an estimated 5 per cent scan inefficiency.

$$\rightarrow (p)\ p\ \pi^+\ \pi^-\ (mm),$$

and divide this number by the sum of the cross sections for the above four reactions. The sum of these cross sections is known by charge symmetry to be equal to the sum of the cross sections for the processes

$$\begin{aligned} \pi^-\ p &\rightarrow \pi^+\ \pi^-\ n \\ &\rightarrow \pi^+\ \pi^-\ (mm), \end{aligned} \tag{A.2}$$

the cross sections for which have been measured over the c.m. energy range of this experiment;[42] see Table 6.

Before displaying the results of this determination of the cross section, one comment should be made: For the events fitting the four $\pi^+ d$ reactions (A.1), we tacitly assume the validity of the spectator model. That is, we assume that one of the protons in the final state did not participate in the reaction, even though in many events both protons have laboratory momentum greater than 300 MeV/c, which is the effective upper limit for laboratory momentum according to the Hulthén wave function. The inclusion in this procedure of <u>all</u> events fitting reactions (A.1) introduces some uncertainty.

Table A.5 summarizes the procedure and the results obtained. No results are given at the momentum settings 1.86 and 2.15 BeV/c, since no 3-pronged events were measured at these momentum values. The errors on the ev/μb values are set at 10 per cent, which is the typical experimental error on the normalization cross section of reference 42.

Table A.5. Exposure size determination via normalization to reactions (A.1).

p (BeV/c)	events* in reactions (A.1)	σ^{42} for reactions (A.1) (mb)	ev/μb
1.10	4 200	11.3	.37 ± .04
1.30	4 669	10.7	.44 ± .04
1.53	25 480	10.6	2.40 ± .24
1.58	4 770	10.4	.46 ± .05
1.70	-	-	-
1.86	-	-	-
2.15	37 156	12.2	3.05 ± .30
2.37	10 577	10.7	.99 ± .10

* The number of events includes a correction for the passing rates of 3-pronged and 4-pronged events and for a scanning inefficiency of 5 per cent.

Summary of Results

Table A.6 summarizes the results for the path length found by the four procedures described above.

It is seen that the last three methods agree with one another, whereas method 1 yields path lengths which are consistently 5-10 per cent higher than the values obtained by the other methods. This is consistent with an estimate of 5-10 per cent of noninteracting muon contamination in the beam. Because of the above-mentioned uncertainty in method 3 due to the inclusion of events with fast spectator protons in the method, the average result of methods 2a and 2b is taken as the final values for the path lengths; these values are given in the last column of Table A.6.

Corollary Result: Determination of $\pi^+ d$ Total Cross Section

As an additional result from method 1, the direct measurement of the path length, we can compute the total $\pi^+ d$ cross section at each of the momentum values from the number of events N found in the scan done for method 1 above, and the direct calculation of path length, L, via the formula

$$\sigma\ (\mu b) = 26.3 \cdot N/L\ (10^6\ cm).$$

Using Table A.1, column 3, to get N, and Table A.2, column 2, for the path length, we obtain the results given in Table A.7, along with the precisely measured values of Carter et al.[34]

Again it is seen that the presence of about 10 per cent of non-interacting muon beam contamination could account for the consistently lower cross section values obtained in this experiment.

Table A.6. Summary of results of exposure size determination.

p (BeV/c)	method 1 (ev/μb)	method 2a (ev/μb)	method 2b (ev/μb)	method 3 (ev/μb)	final result (ev/μb)
1.10	.50	.42	.46	.37	.44
1.30	.45	.43	.44	.44	.44
1.53	2.70	2.57	2.53	2.40	2.55
1.58	.50	.46	.43	.46	.45
1.70	3.09	2.97	3.03	-	3.00
1.86	3.05	2.92	2.92	-	2.92
2.15	3.22	2.88	3.09	3.05	2.97
2.37	.99	.84	.84	.99	.84

Table A.7. $\pi^+ d$ total cross section as measured in this experiment, and from reference 34.

p (BeV/c)	σ_{tot}, this experiment (mb)	σ_{tot}, ref. 34 (mb)
1.10	60.2	71.0
1.30	64.3	69.8
1.53	66.5	71.4
1.58	63.3	69.6
1.70	64.6	66.5
1.86	60.7	64.7
2.15	55.8	63.8
2.37	52.4	63.2

APPENDIX B

SCANNING, MEASURING, AND FITTING

The entire sample of film was scanned once for all 3- and 4-pronged events. A total of 128 000 4-pronged and 93 000 3-pronged events was found. A check scan of a small sample of the film revealed that the overall single-scan efficiency for finding 3- and 4-pronged events was 95 per cent; this efficiency was taken into account in computing the total path length of our exposure (see Appendix A).

Of the events found, all but the 3-pronged events at beam momentum settings 1.70 and 1.86 BeV/c were measured, using Spiral Reader measuring machines I and II[71] of the Lawrence Radiation Laboratory. These new measuring machines afford an order-of-magnitude increase in measuring speed over the older Franckenstein digitized microscope measuring machines, with comparable accuracy.[72] The average measuring rate for the events described here was 80 events per hour.

The measurements were converted into track coordinates by the filtering program POOH. The track coordinates were reconstructed in space and fit to the event hypotheses listed in Section II by the standard Alvarez-group program package TVGP-SQUAW.[73] As an added feature in the fitting of the events, pulse height information on the tracks from the Spiral Reader was used for each kinematic hypothesis to do a separate fit to the expected bubble density of all tracks. This procedure was incorporated into SQUAW with program BUBBLE.[74] About 67 per cent of the first-measured events fit some kinematic hypothesis. All events failing to fit one of the possible hypotheses were remeasured on the Spiral Reader, and about 40 per cent of the

second-measured events then had a successful fit. As a result of the first and second measurements, over 80 per cent of all events had a successful fit after a total of about 240 000 measurements of 182 000 events. Table B.1 gives the numbers of 3- and 4-pronged events found at the different momentum settings, along with their passing rates (fraction of the events fitting one of the hypotheses of Section II).

A special procedure was applied in the fitting of 3-pronged events; these are almost entirely events with two protons in the final state, where one of the protons, the spectator, has momentum so low that no visible track is produced. Therefore in fitting 3-pronged events only hypotheses with at least one proton were attempted; the momentum of the invisible track was set to zero with errors $\Delta p_x = \pm 30$ MeV/c, $\Delta p_y = \pm 30$ MeV/c, and $\Delta p_z = \pm 40$ MeV/c. The larger error on the z-component of momentum reflects the fact that a proton moving in the plus or minus z-direction (along the line of sight of the camera) is less likely to be seen. The errors give an expectation value of momentum magnitude roughly equal to 60 MeV/c, the value at which the Hulthén distribution of spectator momentum has its peak.

After completion of the fitting process, most events were found to have a successful fit to more than one hypothesis. Selection of the correct hypothesis was performed by the program CREE,[75] a version of the program ARROW adapted to the needs of our 3- and 4-prong hypothesis separation. The choice of the most likely hypothesis was made by constructing the empirical function

$$B \quad (\chi^2_{kin} - 4C_{kin}) + \frac{1}{2}(\chi^2_{ion} - C_{ion})$$

and selecting the hypothesis with the lowest value of B as the

Table B.1. Numbers of 3- and 4-pronged events found, and their passing rates.

p (BeV/c)	number of 3-prongs	3-prong pass rate	number of 4-prongs	4-prong pass rate
1.10	2 325	.85	2 216	.79
1.30	2 559	.86	2 808	.84
1.53	16 148	.84	18 829	.80
1.58	2 870	.83	3 515	.76
1.70	18 361	-	24 750	.83
1.86	20 503	-	28 115	.83
2.15	23 339	.84	35 962	.80
2.37	7 053	.87	11 348	.82

"correct" choice. Here

χ^2_{kin} = chi-squared for the kinematic fit

C_{kin} = number of constraints in the kinematic fit

χ^2_{ion} = chi-squared for the track ionization fit

C_{ion} = number of constraints in the track ionization fit

The quantity B stands for the "badness" of the fit; it increases with increasing χ^2 and is reduced as the number of constraints grows larger. This has the effect of biasing in favor of fits with a large number of constraints. Since the number of kinematic constraints in the hypotheses of Section II is either 0, 1, or 4, it is clear that the selection of the hypothesis with the lowest value of "badness" will greatly prefer 4-constraint fits to either of the other constraint classes. The contribution of the ionization fit to the "badness" was weighted to be one-half as important as that of the kinematic fit; note that since all hypotheses have the same number of constraints in the track ionization fit (i.e. they all have the same number of charged tracks), the constant multiplying C_{ion} is taken to be 1. This procedure of choosing the hypothesis with the lowest value of B was found to be preferable to that of making the selection on the basis of the highest confidence level (regardless of constraint class). The latter procedure was found not to express the fact that a fit to a high-constraint-number kinematic hypothesis is likely to be the best choice, even if a fit with fewer constraints is obtained having a higher confidence level. There were two exceptions to the selection method described above:

a) If an event was found to fit best to the final state $p\ p\ \pi^+\ \pi^-\ \gamma$

and second best to $p\ p\ \pi^+\ \pi^-\ \pi^o$ or $p\ p\ \pi^+\ \pi^-$, the second best fit was taken as the correct choice. This is because the final state $p\ p\ \pi^+\ \pi^-\ \gamma$ arises only from the reactions

$$\pi^+ d \to p\ p\ \eta, \qquad \eta \to \pi^+\ \pi^-\ \gamma$$

or

$$\pi^+ d \to p\ p\ \eta'(960), \qquad \eta' \to \pi^+\ \pi^-\ \gamma$$

and gives rise to only a few hundred events, as concluded from other η and η' decay modes. Because there are two orders of magnitude more events from the final states $p\ p\ \pi^+\ \pi^-\ \pi^o$ and $p\ p\ \pi^+\ \pi^-$, and because our mass resolution is such that we cannot discriminate very well between a missing γ and a missing π^o, many $p\ p\ \pi^+\ \pi^-\ \pi^o$ and $p\ p\ \pi^+\ \pi^-$ events were found to fit best to $p\ p\ \pi^+\ \pi^-\ \gamma$, as evidenced by the fact that the $\pi^+\pi^-\gamma$ mass spectrum for these events (assuming that the missing neutral was a γ) showed a strong ω peak for events with $p\ p\ \pi^+\ \pi^-\ \pi^o$ second best, and a strong ρ peak for events with $p\ p\ \pi^+\ \pi^-$ second best. By only taking those events as $p\ p\ \pi^+\ \pi^-\ \gamma$ events when neither $p\ p\ \pi^+\ \pi^-\ \pi^o$ nor $p\ p\ \pi^+\ \pi^-$ is the second best fit, a much smaller and cleaner sample of $p\ p\ \pi^+\ \pi^-\ \gamma$ events was obtained.

b) Events with a best fit to $p\ p\ \pi^+\ \pi^-$, $p\ p\ \pi^+\ \pi^-\ \pi^o$, or $p\ p\ \pi^+\ \pi^-\ \gamma$ and a second best fit to $n\ p\ \pi^+\ \pi^+\ \pi^-$ or $p\ \pi^+\ \pi^+\ \pi^-$ (mm) were found to have a poorer spectator proton momentum distribution than the whole sample of these events. It was found that these events were mostly the final state (n) $p\ \pi^+\ \pi^+\ \pi^-$, where one π^+ in the final state was misinterpreted as a proton; the (misinterpreted) spectator proton momentum distribution then had the appearance of the π^+ momentum

spectrum in the final state (n) $p\,\pi^+\,\pi^+\,\pi^-$. In the few hundred cases in which the three final states mentioned were the first choice and $n\,p\,\pi^+\,\pi^+\,\pi^-$ or $p\,\pi^+\,\pi^+\,\pi^-$ (mm) was second, the order of the choice was reversed, as in case a) above.

Use was made of the program PHONY[76] in generating Monte Carlo events to insure that making the two exceptions listed did not misassign more events than the number correctly assigned.

The missing-mass and confidence level distributions of Section II show the validity of the separation of hypotheses discussed here.

APPENDIX C

C-INVARIANCE VIOLATION IN η DECAY

Consider the decay $\eta \rightarrow \pi^+\pi^-\pi^o$. C is the charge-conjugation quantum number, and P is the parity operator. Since $C(\eta) = +$ and $C(\pi^o) = +$, then $C(\pi^+\pi^-) = +$. But for a spinless boson-antiboson pair, CP is the exchange operator, and hence $CP = +$. This then implies that $P(\pi^+\pi^-) = +$. Now $P(\pi^+\pi^-) = (-)^{\ell}$, where ℓ is the relative angular momentum of the two charged pions in their rest frame, so ℓ = even. This means that the angular distribution of the charged-pions decay direction in their rest frame, with respect to their line of flight (which is the direction of the recoiling π^o in the η rest frame), must be symmetric. This is because the amplitude is a sum of $P_{\ell}(\cos\theta)$, with all ℓ's even, and its square is symmetric in $\cos\theta$.

This says that for every π^o kinetic energy, the $\pi^+\pi^o$ invariant mass (which is proportional to the π^- kinetic energy in the η rest frame) must be distributed like the $\pi^-\pi^o$ invariant mass (which is proportional to the π^+ kinetic energy), so that there are as many π^+'s with kinetic energy greater than that of the π^- as vice versa. Thus the Dalitz plot, which has its x-axis proportional to $T(\pi^+) - T(\pi^-)$, must be right-left symmetric if C is conserved in the decay.

For the $\pi^+\pi^-\gamma$ decay of the η the argument is similar, except that ℓ may only be odd, and the square of a sum of $P_{\ell}(\cos\theta)$ with ℓ odd is again symmetric in $\cos\theta$.

APPENDIX D

$\pi^+ n \rightarrow \eta p$: FORMALISM OF A REGGEIZED A_2-EXCHANGE MODEL WITH VENEZIANO-TYPE RESIDUE FUNCTIONS

The matrix element for π-nucleon scattering, written in terms of the invariant amplitudes A and B, is

$$M = -A + \frac{1}{2} i\gamma \cdot (q_i + q_f) B, \tag{D.1}$$

where γ_μ are the Dirac matrices, and q_i and q_f are the initial- and final-state 4-momenta in the reaction c.m.[77] The cross section becomes

$$\frac{d\sigma}{dt}\ (\mathrm{mb/BeV^2}) = \frac{.3895}{\pi\, s}\left(\frac{M}{4q_i}\right)^2 \left\{ \left| \frac{p}{M} A - k\cos\theta_t B \right|^2 + \left| \frac{k\sqrt{t}}{2M} \sin\theta_t B \right|^2 \right\}, \tag{D.2}$$

where

$$k = \left\{ \left[t - (m_\pi + m_\eta)^2 \right] \left[t - (m_\pi - m_\eta)^2 \right] \right\}^{\frac{1}{2}} \Big/ 2\sqrt{-t}$$

= t-channel meson momentum

$$p = \sqrt{M^2 - t/4}$$

= t-channel baryon momentum

The t-channel reaction is $\pi^- \eta \rightarrow n \bar{p}$, and M is the nucleon mass. $\cos\theta_t$ is the t-channel scattering angle, with

$$4pk\cos\theta_t = s - u$$

The cross section becomes

$$\frac{d\sigma}{dt} = \frac{.3895}{\pi\, s}\left(\frac{M}{4q_i}\right)^2 \left\{ \frac{p^2}{M^2}|A|^2 + \left[\left(\frac{s-u}{4M}\right)^2 + \frac{k^2 t}{4M^2} \right] |B|^2 - \left(\frac{s-u}{2M}\right) \mathrm{Re}(A^* B) \right\}, \tag{D.3}$$

and for angular distributions, of course

$$\frac{d\sigma}{d(\cos\theta)} = 2q_i q_f \frac{d\sigma}{dt} \qquad (D.4)$$

In equations (D.2)-(D.4), q_i and q_f are the initial- and final-state 3-momentum magnitudes.

The A and B amplitudes are given the following Regge representation, which expresses the expectation that the process is dominated by the exchange of the A_2 meson pole, as is drawn in Figure 47:

$$A\ (\text{BeV}^{-1}) = a_o\Gamma(1 - \alpha(t))(1 + e^{-i\pi\alpha(t)})(b's)^{\alpha(t)} \qquad (D.5a)$$

$$B\ (\text{BeV}^{-2}) = b_o\Gamma(1 - \alpha(t))(1 + e^{-i\pi\alpha(t)})(b"s)^{\alpha(t)-1} \qquad (D.5b)$$

The function $\alpha(t)$ is the trajectory function of the $A_2(1300)$ meson, with the linear form

$$\alpha_{A_2}(t) = 2 + b\cdot(t - 1.3^2) \qquad (D.6)$$

The expressions for A and B take on a more familiar Regge form when the identity

$$\Gamma(1 - \alpha) = \frac{\pi}{\sin\pi\alpha}\frac{1}{\Gamma(\alpha)} \qquad (D.7)$$

is noted. This shows the presence of the usual $(\sin\pi\alpha)^{-1}$ pole term explicitly. a_o and b_o are real constants that give the amounts of the terms A and B.

It will now be demonstrated how equations (D.5) arise from the Regge limit ($s \to \infty$, t fixed) of Veneziano expressions for A and B, and, further, how the Veneziano parametrization dictates the values of the constants b, b', and b" in equations (D.5) and (D.6).

Veneziano expressions for A and B can be written as

$$A = a_o\Big[(\tfrac{1}{2} - \sigma)\beta(1 - \tau, \tfrac{1}{2} - \sigma) + (\tfrac{1}{2} - \mu)\beta(1 - \tau, \tfrac{1}{2} - \mu) + (\tfrac{1}{2} - \mu)\beta(\tfrac{1}{2} - \mu, \tfrac{3}{2} - \sigma)\Big] \qquad (D.8a)$$

$$B = b_o\Big[\beta(1 - \tau, \tfrac{1}{2} - \sigma) - \beta(1 - \tau, \tfrac{1}{2} - \mu)\Big] \qquad (D.8b)$$

Here β is the symmetric function

$$\beta(x,y) = \Gamma(x)\Gamma(y)/\Gamma(x + y) \qquad (D.9)$$

σ, τ, and μ are, respectively, the s-, t-, and u-channel trajectory functions, that is, the trajectory functions for the poles dominating the s-, t-, and u-channels.

$$\sigma(s) = \sigma_o + bs \qquad (D.10a)$$

$$\mu(u) = \sigma_o + bu \qquad (D.10b)$$

$$\tau(t) = \tau_o + bt \qquad (D.10c)$$

One of the requirements of the amplitudes A and B is crossing symmetry:

$$A(s,t,u) = A(u,t,s) \qquad (D.11a)$$

$$B(s,t,u) = -B(u,t,s) \qquad (D.11b)$$

The amplitudes A and B are constructed to satisfy these requirements, which they clearly do, and that is why σ and μ are the <u>same</u> functions of their respective variables - the u- and s-channel trajectories in this simplest Veneziano-type representation are the same. (For a complete discussion of the similar example of $\pi N \to \pi N$, see reference 62.)

It will now be shown that the Veneziano amplitudes (D.8) exhibit Regge behavior in the limit $s \to \infty$, t fixed. In taking this limit, the s-trajectory is given a small positive imaginary part, $\sigma_I(s)$ (such that $\sigma_I(s)/s \to 0$ as $s \to \infty$), in order to keep the term $\Gamma(\frac{1}{2} - \sigma)$

finite as the real part of σ goes through positive half-integer values, as it does in the physical region. $\sigma_I(s)$ can be taken to be, e.g.

$$\sigma_I(s) = \text{const.} \sqrt{s - s_{\text{threshold}}};$$

it is to be understood as the width function of the s-channel resonances.

Now go to the Regge limit. In this limit,

$$\sigma \to bs \tag{D.12a}$$

$$\mu \to - bs \tag{D.12b}$$

$$\tau = \text{constant} \tag{D.12c}$$

(ignoring the imaginary part of σ). The second of these limits is true because of

$$s + t + u = 2M^2 + m_\eta^2 + m_\pi^2, \tag{D.13a}$$

thus

$$\sigma + \tau + \mu = b\cdot(2M^2 + m_\eta^2 + m_\pi^2) + 2\sigma_o + \tau_o \tag{D.13b}$$

The first term in the expression for A becomes, using equation (D.7)

$$a_o(-bs)\Gamma(1 - \tau)\frac{\sin\pi(3/2 - \tau - \sigma)}{\sin\pi(1/2 - \sigma)}\frac{\Gamma(-1/2 + \tau + \sigma)}{\Gamma(1/2 + \sigma)}$$

$$= a_o(-bs)\Gamma(1 - \tau)\left[\cos\pi(1 - \tau) + \cot\pi(1/2 - \sigma)\cdot\sin\pi(1 - \tau)\right]\cdot$$
$$\cdot\Gamma(-1/2 + \tau + \sigma)/\Gamma(1/2 + \sigma)$$

Now

$$\Gamma(x)/\Gamma(y) \cong y^{(x - y)} \text{ for } x, y \text{ large, and } x - y \ll y \tag{D.14}$$

as can be quickly seen after noting that

$$\Gamma(x) = (x - 1)! \text{ for integer } x$$

The term under consideration is then approximately

$$a_o(-bs)\Gamma(1-\tau)\left[\cos\pi(1-\tau)+\cot\pi(1/2-\sigma)\sin\pi(1-\tau)\right]\left(\frac{1}{2}+\sigma\right)^{\tau-1}$$

Now because of the presence of σ_I,

$$\cot\pi(1/2-\sigma)\to i \text{ as } s\to\infty,$$

and the term becomes

$$\begin{aligned} &a_o(-bs)\Gamma(1-\tau)e^{i\pi(1-\tau)}(bs)^{\tau-1} \\ &= a_o\Gamma(1-\tau)e^{-i\pi\tau}(bs)^{\tau} \end{aligned} \tag{D.15}$$

The second term in (D.8a) becomes, in the same limit

$$\begin{aligned} &a_o\left(\frac{1}{2}-\mu\right)\beta\left(1-\tau,\frac{1}{2}-\mu\right) \\ &\to a_o(bs)\Gamma(1-\tau)\Gamma\left(\frac{1}{2}-\mu\right)/\Gamma\left(\frac{3}{2}-\tau-\mu\right) \\ &\cong a_o(bs)\Gamma(1-\tau)\left(\frac{3}{2}-\tau-\mu\right)^{\tau-1} \\ &\cong a_o\Gamma(1-\tau)(bs)^{\tau} \end{aligned} \tag{D.16}$$

The third term in (D.8a) goes as

$$\begin{aligned} &\Gamma\left(\frac{3}{2}-\mu\right)\Gamma\left(\frac{3}{2}-\sigma\right)/\Gamma(2-\mu-\sigma) \\ &\to \frac{1}{\Gamma(\text{const.})}\,\frac{\Gamma(3/2-\mu)}{\Gamma(-1/2+\sigma)}\,\frac{\pi}{\sin\pi(3/2-\sigma)}, \end{aligned}$$

using (D.13b) and (D.7), and hence approaches

$$\begin{aligned} &\text{const.}\left(-\frac{1}{2}+\sigma\right)^{2-\mu-\sigma}/\sin\pi\left(\frac{3}{2}-\sigma\right) \\ &= \text{const.}\left(-\frac{1}{2}+\sigma\right)^{\text{const.}}/\sin\pi\left(\frac{3}{2}-\sigma\right) \to 0, \end{aligned} \tag{D.17}$$

since the imaginary part of σ makes the denominator go to infinity exponentially. Adding equations (D.15), (D.16), and (D.17) shows that

$$A \rightarrow a_o \Gamma(1 - \tau)(1 + e^{-i\pi\tau})(bs)^{\tau}$$

Similarly B becomes

$$B \rightarrow b_o \Gamma(1 - \tau)(1 + e^{-i\pi\tau})(bs)^{\tau-1}$$

in the Regge limit.

Comparing this with equations (D.5) and noting that $\tau(t) = \alpha(t)$, it is clear that the Veneziano formula is indeed constructed to give Regge behavior in the Regge limit, with a residue function of $\Gamma(1 - \tau)$. It is emphasized that the Regge behavior, including the proper signature factor, holds only when the slope of all the trajectories is the same. Hence the Veneziano representation prescribes not only the residue functions, it also requires that in equations (D.5)

$$b = b' = b'' \qquad \text{(D.18)}$$

be the universal slope of all particle trajectories, which is taken to be

$$b = 1 \text{ BeV}^{-2}$$

from experiment.

The Veneziano representation in the Regge limit thus leaves only the constants a_o and b_o to be determined by a fit to experiment.

APPENDIX E

NOTATIONS

Below is a list of notations frequently used in this report.

E = total energy

$\vec{p}$ = 3-momentum, with components p_x, p_y, p_z.

$p = (\vec{p}, E)$ = 4-momentum

$p_1 \cdot p_2 = E_1 E_2 - \vec{p}_1 \cdot \vec{p}_2$ = 4-vector dot product

$m = \sqrt{E^2 - \vec{p}^2}$ = mass of a particle or system of particles

For the reaction

$$\text{meson(1)} + \text{baryon(2)} \rightarrow \text{meson(3)} + \text{baryon(4)}$$

the Mandelstam variables are, in terms of 4-momenta

$s = (p_1 + p_2)^2 = (p_3 + p_4)^2$

$t = (p_1 - p_3)^2 = (p_2 - p_4)^2$

$u = (p_1 - p_4)^2 = (p_2 - p_3)^2$.

φ = azimuthal angle in a spherical coordinate system

θ = polar angle in a spherical coordinate system

$\vec{n}$ = normal to the production plane in a reaction with a two-body or quasi-two-body final state

$= \vec{p}(\text{beam}) \times \vec{p}(\text{outgoing meson})$

The convention $c = 1$ is often used, where c is the speed of light.

APPENDIX F

THE SPIN DENSITY MATRIX FOR A SPIN-1 PARTICLE AND ITS DETERMINATION USING THE METHOD OF MOMENTS

Familiarity with the basic theory of the spin density matrix[68] will be assumed in this discussion. The decay of a 1^- particle into two pions or into three pions[68] gives a decay angular distribution with the general form

$$W(\theta,\varphi) = \sum_{m,n} \rho_{m,n} Y_1^{m*} Y_1^n ; \qquad (F.1)$$

this is the distribution of the pion line of flight in the former case and of the normal to the plane of the three pions in the latter case. Restrictions on the form of the decay distribution are supplied by the hermiticity of the spin density matrix and by unitarity:

$$\rho_{1,1} + \rho_{0,0} + \rho_{-1,-1} = 1 \qquad (F.2)$$

Furthermore, conservation of parity in the production process implies, when the quantization axis is in the production plane, that[69b]

$$\rho_{m,n} = (-)^{m-n}\rho_{-m,-n} \qquad (F.3)$$

Application of hermiticity and the conditions (F.2) and (F.3) yield

$$W(\theta,\varphi) = \frac{3}{4\pi}\Big[\rho_{0,0}\cos^2\theta + \frac{1}{2}(1 - \rho_{0,0})\sin^2\theta - \rho_{1,-1}\sin^2\theta\cos 2\varphi - \sqrt{2}\,\mathrm{Re}(\rho_{1,0})\sin 2\theta\cos\varphi \Big] \qquad (F.4)$$

Furthermore

$$\rho_{0,0} + 2\rho_{1,1} = 1, \qquad (F.5)$$

and $\rho_{0,0}$, $\rho_{1,1}$, and $\rho_{1,-1}$ are real.

Using the spherical harmonics, equation (F.4) can be rewritten as

$$W(\theta,\varphi) = \frac{1}{4\pi}\Big[\, 1 + \sqrt{\frac{4\pi}{5}}\,(3\rho_{0,0} - 1)Y_2^0 - 12\sqrt{\frac{4\pi}{30}}\,\rho_{1,-1}\mathrm{Re}(Y_2^2) + 12\sqrt{\frac{4\pi}{15}}\,\mathrm{Re}(\rho_{1,0})\mathrm{Re}(Y_2^1)\,\Big] \qquad \text{(F.6)}$$

Note that $W(\theta,\varphi)$, integrated over all angles, is 1. It can be easily seen that the functions

$$Y_\ell^0,\ \mathrm{Re}(Y_\ell^m),\ \mathrm{Im}(Y_\ell^m),\quad m = 1, 2, \ldots, \ell \qquad \text{(F.7)}$$

are an orthogonal set of real functions; they are more useful than the complex functions Y_ℓ^m for expanding a (real!) decay distribution like $W(\theta,\varphi)$. Since the functions (F.7) are orthogonal, the expansion coefficients in the expansion

$$W(\theta,\varphi) = 1 + \sum_{\ell=1}^{N}\Big[\, a_\ell Y_\ell^0 + \sum_{m=1}^{\ell}\big(\, R_{\ell m}\mathrm{Re}(Y_\ell^m) + I_{\ell m}\mathrm{Im}(Y_\ell^m)\,\big)\Big] \qquad \text{(F.8)}$$

are given by the moments expressions

$$a_\ell = \langle Y_\ell^0\rangle \qquad \text{(F.9a)}$$

$$R_{\ell m} = 2\langle \mathrm{Re}(Y_\ell^m)\rangle \qquad \text{(F.9b)}$$

$$I_{\ell m} = 2\langle \mathrm{Im}(Y_\ell^m)\rangle \qquad \text{(F.9c)}$$

Here, e.g., $\langle Y_\ell^0\rangle$ means the average of Y_ℓ^0 over $W(\theta,\varphi)$. Comparing (F.8) and (F.9) with (F.6), the equations (VI.3) for the density matrix elements of the decay $\omega \to \pi^+\pi^-\pi^0$ are obvious; the factor f in equations (VI.3) accounts for the fact that the ω decay distribution does not integrate to 1 but to f, the fraction of ω events in the sample.

ACKNOWLEDGMENTS

I wish to thank all those whose support, knowledge, guidance, and inspiration have helped me in the completion of this work.

Thanks are due to the crews of the Bevatron and the 72-inch bubble chamber.

The scanning and measuring efforts, as well as the handling of the many large computer jobs associated with the preliminary data reduction were supervised by our competent experiment librarians Wally Hendricks, Betty Armstrong, Maureen Nassiri, and Meredeth Vogler. I also owe thanks to the many scanners, and to the supervisors and operators of the Spiral Reader measuring machines.

The staff of the LRL computer center deserve thanks for their constant cooperation throughout the months of data analysis in ensuring fast, reliable processing of hundreds of computer jobs.

I particularly acknowledge many useful discussions with my graduate student colleague Don Davies. I thank Professors Don Miller and Janos Kirz for their guidance, and I am grateful to my colleagues Paul Hoch and Bob Rader and to Drs. Orin Dahl and Maris Abolins for their assistance.

I acknowledge the support and encouragement of Prof. Luis Alvarez throughout the time that I have been a member of his group, and his hospitality at his weekly seminars. I note that the funds financing this work were granted by the U. S. Atomic Energy Commission.

Finally, a special expression of thanks to my wife Gudrun for her unlimited patience during the final months of work and the preparation of this manuscript.

FOOTNOTES AND REFERENCES

1. W. Chinowsky, G. Smith, and J. Kirz, Bevatron Secondary Beam 1B, in Bevatron Experimenters' Handbook, Sec. C., December 1965.

2. P. Hoch, Alvarez Group Memo 616, 1966.

3. Donald W. Davies, Ph. D. thesis, University of California at Berkeley, 1969.

4. Maris A. Abolins, Orin I. Dahl, Jerome Danburg, Donald Davies, Paul Hoch, Donald H. Miller, Robert Rader, and Janos Kirz, Phys. Rev. Letters 22, 427 (1969).

5. Robert J. Manning, Ph. D. thesis, University of California at Berkeley, 1969.

6. Gerald A. Smith and Robert J. Manning, Phys. Rev. 171, 1399 (1968).

7. Maris A. Abolins, Orin I. Dahl, Jerome S. Danburg, Donald Davies, Paul Hoch, Donald H. Miller, and Robert Rader, Heidelberg International Conf. on Elementary Particles, 1967.

8. Jerome S. Danburg, Maris A. Abolins, Orin I. Dahl, Donald W. Davies, Paul L. Hoch, Janos Kirz, Donald H. Miller, and Robert K. Rader, Bull. of American Phys. Soc. 14, 76 (1969).

9. Donald W. Davies, Maris A. Abolins, Orin I. Dahl, Jerome S. Danburg, Paul L. Hoch, Janos Kirz, Donald H. Miller, and Robert K. Rader, Bull. of American Phys. Soc. 14, 119 (1969).

10. Robert K. Rader, Maris A. Abolins, Orin I. Dahl, Jerome S. Danburg, Donald W. Davies, Paul L. Hoch, Janos Kirz, and Donald H. Miller, Bull. of American Phys. Soc. 14, 560 (1969).

11. J. Gezelter, S. Lichtman, F. J. Loeffler, R. J. Miller, and R. B. Willmann, Nuovo Cimento 53A, 213 (1968).

12. R. J. Miller, S. Lichtman, and R. B. Willmann, Phys. Rev. 178, 2061 (1969).

13. π^+ d at .65-.85 BeV/c:

a) E. Pauli, A. Muller, R. Barloutaud, L. Cardin, J. Meyer, M. Beneventano, G. Gialanella, L. Paoluzi, and R. Finzi, in Proc. of the Siena International Conf. on Elementary Particles, Vol. I, 92 (1963);

b) A. Muller, E. Pauli, R. Berloutaud, L. Cardin, J. Meyer, M. Beneventano, G. Gialanella, and L. Paoluzi, ibid., Vol. I, 99 (1963);

c) E. Pauli and A. Muller, Phys. Letters 13, 351 (1964).

14. π^+ d at .82 BeV/c:

a) C. Baltay, P. Franzini, J. Kim, L. Kirsch, D. Zanello, J. Lee-Franzini, R. Loveless, J. McFadyen, and H. Yarger, Phys. Rev. Letters 16, 1224 (1966);

b) C. Baltay, P. Franzini, J. Kim, R. Newman, N. Yeh, and L. Kirsch, Phys. Rev. Letters 19, 1495 (1967);

c) C. Baltay, P. Franzini, J. Kim, L. Kirsch, R. Newman, N. Yeh, J. A. Cole, J. Lee-Franzini, and H. Yarger, Phys. Rev. Letters 19, 1498 (1967).

15. π^+ d at .82 BeV/c:

a) A. Larribe, A. Leveque, A. Muller, E. Pauli, D. Revel, T. Tallini, P. J. Litchfield, L. K. Rangan, A. M. Segar, J. R. Smith, P. J. Finney, C. M. Fisher, and E. Pickup, Phys. Letters 23, 600 (1966);

b) P. J. Litchfield, L. K. Rangan, A. M. Segar, J. R. Smith,

A. Larribe, A. Leveque, A. Muller, E. Pauli, D. Revel, and B. Tallini, Phys. Letters 24B, 486 (1967);

c) P. J. Litchfield, Nuovo Cimento 58A, 468 (1968).

16. π^+ d at .82 BeV/c:

M. Bazin, A. T. Goshaw, R. Zacher, H. Blumenfeld, T. Kitagaki, and C. R. Sun, Phys. Rev. Letters 19, 1157 (1967).

17. π^+ d at 1.23 BeV/c:

a) A. Pevsner, R. Kraemer, M. Nussbaum, P. Schlein, T. Toohig, M. Block, A. Kovacs, and C. Meltzer, in Proc. of Int'l Conf. on Elem. Particles, Aix-en-Provence, 277 (1961);

b) A. Pevsner, R. Kraemer, M. Nussbaum, C. Richardson, P. Schlein, R. Strand, T. Toohig, M. Block, A. Engler, R. Gessaroli, and C. Meltzer, Phys. Rev. Letters 7, 421 (1961);

c) C. Richardson, R. Kraemer, M. Meer, M. Nussbaum, A. Pevsner, R. Strand, T. Toohig, and M. Block, in Proc. of 1962 CERN Conf., 96 (1962);

d) T. Toohig, R. Kraemer, L. Madansky, M. Meer, M. Nussbaum, A. Pevsner, C. Richardson, and M. Block, ibid., 99 (1962);

e) M. Meer, R. Strand, R. Kraemer, L. Madansky, M. Nussbaum, A. Pevsner, C. Richardson, T. Toohig, M. Block, S. Orenstein, and T. Fields, ibid., 103 (1962);

f) T. Fields, S. Orenstein, R. Kraemer, L. Madansky, M. Meer, A. Pevsner, C. Richardson, and T. Toohig, in Proc. of Athens Topical Conf. on Resonant Particles, 185 (1963);

g) R. Kraemer, L. Madansky, M. Meer, M. Nussbaum, A. Pevsner, C. Richardson, R. Strand, R. Zdanis, T. Fields, S. Orenstein, and

T. Toohig, Phys. Rev. 136B, 496 (1964).

18. π^+ d at 1.7 BeV/c:

a) T. C. Bacon, H. W. K. Hopkins, D. K. Robinson, D. G. Hill, E. O. Salant, A. Engler, H. E. Fisk, C. M. Meltzer, and J. B. Westgard, in Proc. of Dubna Conf., Vol. I, 532 (1964);

b) T. C. Bacon, W. J. Fickinger, D. G. Hill, H. W. K. Hopkins, D. K. Robinson, and E. O. Salant, in Proc. of Athens Conf. on Newly Discovered Resonances, 129 (1965);

c) T. C. Bacon, W. J. Fickinger, D. G. Hill, H. W. K. Hopkins, D. K. Robinson, and E. O. Salant, Phys. Rev. 157, 1263 (1967).

19. π^+ d at 2.15 BeV/c:

K. J. Braun, D. Cline, and V. Scherer, Phys. Rev. Letters 21, 1275 (1968).

20. π^+ d at 3.29 BeV/c:

a) N. Gelfand, G. Lütjens, and J. Steinberger, in Proc. of Dubna Conf., Vol. I, 437 (1964);

b) N. Gelfand, G. Lütjens, M. Nussbaum, J. Steinberger, H. O. Cohn, W. M. Bugg, and G. T. Condo, Phys. Rev. Letters 12, 567 (1964);

c) H. O. Cohn, W. M. Bugg, and G. T. Condo, Phys. Letters 15, 344 (1965);

d) H. O. Cohn, W. M. Bugg, G. T. Condo, R. D. McCulloch, G. Lütjens, and N. Gelfand, Phys. Rev. Letters 15, 906 (1965);

e) H. O. Cohn, R. D. McCulloch, W. M. Bugg, and G. T. Condo, Phys. Letters 21, 347 (1966);

f) H. O. Cohn, R. D. McCulloch, W. M. Bugg, and G. T. Condo,

Nucl. Phys. 82, 690 (1966);

g) H. O. Cohn, R. D. McCulloch, W. M. Bugg, and G. T. Condo, Nucl. Phys. B1, 57 (1967);

h) W. M. Bugg, G. T. Condo, J. T. Humphreys, R. D. McCulloch, and H. O. Cohn, Nucl. Phys. B6, 246 (1968).

21. π^+ d at 3.65 BeV/c:

a) G. Benson, L. Lovell, E. Marquit, B. Roe, D. Sinclair, J. Vander Velde, and K. Weaver, Phys. Rev. Letters 12, 600 (1964);

b) G. Benson, L. Lovell, E. Marquit, B. Roe, D. Sinclair, and J. Vander Velde, Phys. Rev. Letters 16, 1177 (1966);

c) G. Benson, E. Marquit, B. Roe, D. Sinclair, and J. Vander Velde, Phys. Rev. Letters 17, 1234 (1966);

d) George C. Benson, Ph. D. thesis, University of Michigan, 1966;

e) G. C. Benson, B. P. Roe, D. Sinclair, and J. C. Vander Velde, Phys. Rev. Letters 22, 1074 (1969).

22. π^+ d at 4.5 BeV/c:

a) A. Forino et al. (Saclay-Orsay-Bologna Collaboration), in Proc. of Dubna Conf., Vol. I, 445 (1964);

b) A. Forino et al. (Saclay-Orsay-Bari-Bologna Collaboration), Phys. Letters 11, 347 (1964);

c) A. Forino et al. (Saclay-Orsay-Bologna Collaboration), Phys. Letters 19, 65 (1965);

d) A. Forino et al. (Saclay-Orsay-Bari-Bologna-Firenze Collaboration), Phys. Letters 19, 68 (1965).

23. π^+ d at 5.1 BeV/c:

a) N. Armenise et al. (Bari-Bologna-Firenze-Orsay Collaboration),

Phys. Letters 25B, 53 (1967);

b) N. Armenise et al. (Bari-Bologna-Firenze-Orsay Collaboration), Phys. Letters 26B, 336 (1968);

c) N. Armenise et al. (Bari-Bologna-Firenze-Orsay Collaboration), Nuovo Cimento 54A, 999 (1968).

24. π^+ d at 6 BeV/c:

a) F. Bruyant, M. Goldberg, G. Vegni, H. Winzeler, P. Fleury, J. Huc, R. Lestienne, G. de Rosny, and R. Vanderhagen, in Proc. of Dubna Conf., Vol. I, 180 (1964);

b) F. Bruyant, M. Goldberg, G. Vegni, H. Winzeler, P. Fleury, J. Huc, R. Lestienne, G. de Rosny, and R. Vanderhagen, ibid., Vol. I, 442 (1964);

c) F. Bruyant, M. Goldberg, M. Holder, M. Krammer, J. V. Major, G. Vegni, H. Winzeler, P. Fleury, J. Huc, R. Lestienne, G. de Rosny, and R. Vanderhagen, Phys. Letters 10, 232 (1964);

d) F. Bruyant, M. Goldberg, G. Vegni, H. Winzeler, P. Fleury, J. Huc, R. Lestienne, G. de Rosny, and R. Vanderhagen, Phys. Letters 12, 278 (1964);

e) M. Goldberg et al. (CERN-Ecole Polytechnique Collaboration), Phys. Letters 17, 354 (1965);

f) G. Vegni, H. Winzeler, P. Zaniol, P. Fleury, and G. de Rosny, Phys. Letters 19, 526 (1965);

g) G. de Rosny and P. Fleury, Nuovo Cimento 48A, 1137 (1967).

25. π^+ d at 8 BeV/c:

a) A. M. Cnops, P. V. C. Hough, F. R. Huson, I. R. Kenyon, J. M. Scarr, I. O. Skillicorn, H. O. Cohn, R. D. McCulloch, W. M. Bugg,

G. T. Condo, and M. M. Nussbaum, Phys. Rev. Letters 21, 1609 (1968); b) A. M. Cnops, P. V. C. Hough, F. R. Huson, I. R. Kenyon, J. M. Scarr, I. O. Skillicorn, H. O. Cohn, R. D. McCulloch, W. M. Bugg, G. T. Condo, and M. M. Nussbaum, Phys. Letters 29B, 45 (1969).

26. N. Barash-Schmidt, A. Barbaro-Galtieri, L. R. Price, A. H. Rosenfeld, P. Söding, C. G. Wohl, M. Roos, and G. Conforto, UCRL 8030, Jan. 1969.

27. J. M. Blatt and V. F. Weisskopf, Theoretical Nuclear Physics (John Wiley and Sons, New York, 1952), Chap. II.

28. Lamek Hulthén and Masao Sugawara, in Handbuch der Physik (Springer-Verlag, Berlin, 1957), Vol. 39, Chap. 1.

29. R. L. Gluckstern and H. A. Bethe, Phys. Rev. 81, 761 (1951).

30. M. Moravcsik, Nucl. Phys. 7, 113 (1958).

31. R. G. Newton, Scattering Theory of Waves and Particles (McGraw-Hill Book Company, 1966), Chap. 8.

32. R. J. Glauber, Phys. Rev. 100, 242 (1955).

33. Colin Wilkin, Phys. Rev. Letters 17, 561 (1966).

34. A. A. Carter, K. F. Riley, R. J. Tapper, D. V. Bugg, R. S. Gilmore, K. M. Knight, D. C. Salter, G. H. Stafford, E. J. N. Wilson, J. D. Davies, J. D. Dowell, P. M. Hattersley, R. J. Homer, and A. W. O'Dell, Phys. Rev. 168, 1457 (1968).

35. V. J. Stenger, W. E. Slater, D. H. Stork, H. K. Ticho, G. Goldhaber, and S. Goldhaber, Phys. Rev. 134B, 1111 (1964).

36. I. Butterworth, J. L. Brown, G. Goldhaber, S. Goldhaber, A. A. Hirata, J. A. Kadyk, B. M. Schwarzschild, and G. H. Trilling, Phys. Rev. Letters 15, 734 (1965).

37. J. Friedman, Alvarez Group Programming Note P-156 (1966).

38. J. Bartsch et al. (Aachen-Berlin-Birmingham-Bonn-Hamburg-London-München Collaboration), Phys. Letters 11, 167 (1964).

39. A. Barbaro-Galtieri and P. Söding, UCRL 18271, 1968.

40. S. Y. Fung, W. Jackson, R. T. Pu, D. Brown, and G. Gidal, Phys. Rev. Letters 21, 47 (1968).

41. R. K. Rader, private communication, 1969.

42. a) E. Pickup, D. K. Robinson, E. O. Salant, F. Ayer, and B. A. Munir, Phys. Rev. 132, 1819 (1963);
b) T. C. Bacon, W. J. Fickinger, D. G. Hill, H. W. K. Hopkins, D. K. Robinson, and E. O. Salant, Phys. Rev. 157, 1263 (1967);
c) L. D. Jacobs, UCRL 16877, 1966.

43. F. Bulos et al. (Brown-Brandeis-Harvard-M.I.T.-Padua Collaboration), Phys. Rev. Letters 13, 486 (1964).

44. W. B. Richards, C. B. Chiu, R. D. Eandi, A. C. Helmholz, B. W. Kenney, B. J. Moyer, J. A. Poirier, R. J. Cence, V. Z. Peterson, N. K. Sehgal, and V. J. Stenger, Phys. Rev. Letters 16, 1221 (1966).

45. H. R. Crouch et al. (Brown-Harvard-Padua-Weizmann Institute-M.I.T. Collaboration), Phys. Rev. Letters 21, 845 (1968).

46. M. A. Wahlig and I. Mannelli, Phys. Rev. 168, 1515 (1968).

47. O. Guisan, J. Kirz, P. Sonderegger, A. V. Stirling, P. Borgeaud, C. Bruneton, P. Falk-Vairant, B. Amblard, C. Caversasio, J. P. Guillaud, and M. Yvert, Phys. Letters 18, 200 (1965).

48. J. H. Boyd, A. R. Erwin, W. D. Walker, and E. West, Phys. Rev. 166, 1458 (1968).

49. T. D. Lee, Phys. Rev. 139B, 1415 (1965).

50. H. Yuta and S. Okubo, Phys. Rev. Letters 21, 781 (1968).

51. P. K. Kabir, Phys Rev. 178, 2486 (1969).

52. Columbia-Berkeley-Purdue-Wisconsin-Yale Collaboration, Phys. Rev. 149, 1044 (1966).

53. A. M. Cnops, J. Finocchiaro, J. C. Lassalle, P. Mittner, P. Zanella, J. P. Dufey, B. Gobbi, M. A. Pouchon, and A. Müller, Phys. Letters 22, 546 (1966).

54. M. Gormley, E. Hyman, W. Lee, T. Nash, J. Peoples, C. Schultz, and S. Stein, Phys. Rev. Letters 21, 402 (1968).

55. Frank S. Crawford, Jr. and LeRoy R. Price, Phys. Rev. Letters 16, 333 (1966).

56. R. A. Bowen, A. M. Cnops, G. Finocchiaro, P. Mittner, J. P. Dufey, B. Gobbi, M. A. Pouchon, and A. Müller, Phys. Letters 24B, 206 (1967).

57. M. Gormley, E. Hyman, W. Lee, T. Nash, J. Peoples, C. Schultz, and S. Stein, Phys. Rev. Letters 21, 399 (1968).

58. Laurie M. Brown and Paul Singer, Phys. Rev. Letters 8, 460 (1962); Laurie M. Brown and Paul Singer, Phys. Rev. 133B, 812 (1964).

59. LeRoy R. Price and Frank S. Crawford, Jr., Phys. Rev. 167, 1339 (1968).

60. A. M. Cnops, G. Finocchiaro, P. Mittner, J. P. Dufey, B. Gobbi, M. A. Pouchon, and A. Müller, Phys. Letters 27B, 113 (1968).

61. This possible bias was suggested by J. D. Jackson, private communication, 1969.

62. This parametrization of the cross section was suggested by Richard C. Brower, private communication, 1969; see also K. Igi,

Phys. Letters 28B, 330 (1968) for an example of such a parametrization for the reaction $\pi N \to \pi N$.

63. F. Arbab, N. F. Bali, and J. W. Dash, Phys. Rev. 158, 1515 (1967). Our kinematical factors are identical to those in this reference when A and B are written in terms of helicity amplitudes.

64. a) Roger J. N. Phillips and William Rarita, Phys. Rev. 140B, 200 (1965);

b) Roger J. N. Phillips and William Rarita, Phys. Rev. Letters 15, 807 (1965);

c) R. J. N. Phillips and W. Rarita, Phys Letters 19, 598 (1965);

d) R. J. N. Phillips, Nucl. Phys. B1, 573 (1967);

e) Farzam Arbab, Naren F. Bali, and Jan W. Dash, Phys. Rev. 158, 1515 (1967);

f) D. D. Reeder and K. V. L. Sarma, Nuovo Comento 51A, 169 (1967);

g) D. D. Reeder and K. V. L. Sarma, Phys. Rev. 172, 1566 (1968);

h) Maurice L. Blackmon, Phys. Rev. 178, 2385 (1969).

65. B. C. Maglić, L. W. Alvarez, A. H. Rosenfeld, and M. L. Stevenson, Phys. Rev. Letters 7, 178 (1961); M. L. Stevenson, L. W. Alvarez, B. C. Maglić, and A. H. Rosenfeld, Phys. Rev. 125, 687 (1962).

66. S. M. Flatté, D. O. Huwe, J. J. Murray, J. Button-Shafer, F. T. Solmitz, M. L. Stevenson, and C. Wohl, Phys. Rev. 145, 1050 (1966).

67. Charles Zemach, Phys. Rev. 133B, 1201 (1964).

68. J. D. Jackson, Particle and Polarization Angular Distributions for Two and Three Body Decays, in High Energy Physics, 1965 Les Houches Lectures, edited by C. Dewitt and M. Jacob (Gordon

and Breach Science Publishers, Inc., New York, 1965).

69. a) K. Gottfried and J. D. Jackson, Phys. Letters 8, 144 (1964);
b) K. Gottfried and J. D. Jackson, Nuovo Cimento 33, 309 (1964);
c) J. D. Jackson and H. Pilkuhn, Nuovo Cimento 33, 906 (1964);
d) K. Gottfried and J. D. Jackson, Nuovo Cimento 34, 735 (1964);
e) J. D. Jackson, J. T. Donohue, K. Gottfried, R. Keyser, and B. E. Y. Svensson, Phys. Rev. 139B, 428 (1965);
f) J. D. Jackson, Revs. Mod. Phys. 37, 484 (1965).

70. I am grateful to J. D. Jackson and C. Quigg for providing the ρ-exchange programs.

71. Gerald R. Lynch, UCRL 17328, 1967.

72. G. Lynch, Alvarez Group Memo 575 (1965); R. K. Rader, Alvarez Group Memo 677 (1968).

73. F. T. Solmitz, A. D. Johnson, and T. B. Day, Alvarez Group Programming Note P-117 (1966).

74. J. S. Danburg and G. R. Lynch, Alvarez Group Programming Note P-160 (1967).

75. Orin Dahl and Don Davies, Alvarez Group Programming Note P-154 (1966).

76. D. Drijard, Trilling-Goldhaber Group Technical Note 143 (1968).

77. R. J. Eden, High Energy Collisions of Elementary Particles (Cambridge University Press, 1967), Chap. 9.